



저작자표시-비영리-변경금지 2.0 대한민국

이용자는 아래의 조건을 따르는 경우에 한하여 자유롭게

- 이 저작물을 복제, 배포, 전송, 전시, 공연 및 방송할 수 있습니다.

다음과 같은 조건을 따라야 합니다:



저작자표시. 귀하는 원저작자를 표시하여야 합니다.



비영리. 귀하는 이 저작물을 영리 목적으로 이용할 수 없습니다.



변경금지. 귀하는 이 저작물을 개작, 변형 또는 가공할 수 없습니다.

- 귀하는, 이 저작물의 재이용이나 배포의 경우, 이 저작물에 적용된 이용허락조건을 명확하게 나타내어야 합니다.
- 저작권자로부터 별도의 허가를 받으면 이러한 조건들은 적용되지 않습니다.

저작권법에 따른 이용자의 권리는 위의 내용에 의하여 영향을 받지 않습니다.

이것은 [이용허락규약\(Legal Code\)](#)을 이해하기 쉽게 요약한 것입니다.

[Disclaimer](#)

공학박사학위논문

Application of Nanostructured Materials for  
Highly Efficient Flexible Energy Harvesters

나노구조재료를 이용한 고효율 유연성  
광전 및 압전소자에 관한 연구

2016년 2월

서울대학교 대학원

재료공학부

이 호 림

# Application of Nanostructured Materials for Highly Efficient Flexible Energy Harvesters

## 나노구조재료를 이용한 고효율 유연성 광전 및 압전소자에 관한 연구

지도교수 서 용 석  
이 논문을 공학박사학위논문으로 제출함  
2016년 2월

서울대학교 대학원  
재료공학부  
이 호 립

이호림의 박사학위논문을 인준함  
2016년 2월

위 원 장	<u>김 장 주 (인)</u>
부 위 원 장	<u>서 용 석 (인)</u>
위 원	<u>박 수 영 (인)</u>
위 원	<u>강 용 수 (인)</u>
위 원	<u>김 동 영 (인)</u>

# **Abstract**

## **Application of Nanostructured Materials for Highly Efficient Flexible Energy Harvesters**

**Horim Lee**

Department of Materials Science and Engineering

Seoul National University

With the energy crisis and environmental pollution by fossil fuels, the development for clean and renewable energy sources has attracted considerable interest in the past decade. In most cases, it has been focused on the energy resources for large-scale power generation, such as hydraulic power, wind power, and nuclear plants. More recently, in addition to alternatives energy sources for the large scale power generation, energy harvesting from ambient energy sources including solar, thermal and

mechanical energy for small-scale mobile application has been actively investigated due to recent progress of power consumption efficiency.

In this study, we prepared highly efficient energy harvester using nanostructured materials. Among the variety of energy sources, we focused on the light and mechanical energy and fabricated solar cells and piezoelectric nanogenerators. These energy sources are always available in environment and easy to utilize. Also, power generation characteristics of assembled devices were investigated.

First, we fabricated flexible dye-sensitized solar cells (DSSCs) using 0-D  $\text{TiO}_2$  aggregates. Hierarchically structured  $\text{TiO}_2$  (HS- $\text{TiO}_2$ ) was prepared on a flexible ITO-PEN (polyethylene naphthalate) substrate via electrospray deposition using a commercially available  $\text{TiO}_2$  nanocrystalline powder in order to fabricate flexible DSSCs under low-temperature ( $<150^\circ\text{C}$ ) conditions. The cell efficiency increased when using flexible ITO-PEN substrates post-treated by either a mechanical compression treatment or a chemical sintering treatment using titanium tetrabutoxide (TTB). The mechanical compression treatment reduced the surface area and porosity of the HS- $\text{TiO}_2$ ; however, this treatment improved the inter-particle connectivity and physical adhesion between the HS- $\text{TiO}_2$  and ITO-PEN substrate, which increased the photocurrent density of the as-pressed HS-

TiO<sub>2</sub> cells. The electron diffusion coefficients of the as-pressed HS-TiO<sub>2</sub> improved upon compression treatment whereas the recombination lifetimes remained unchanged. An additional chemical sintering post-treatment involving TTB was tested for its effects on DSSC efficiency. The freshly coated TiO<sub>2</sub> submitted to TTB hydrolysis in water at 100°C yielded an anatase phase. TTB treatment of the HS-TiO<sub>2</sub> cell after compression treatment yielded faster electron diffusion, providing an efficiency of 5.57% under 100 mW cm<sup>-2</sup>, AM 1.5 global illumination.

Long-term stability of flexible DSSCs is also important for real application. We examined the influence of dye binding mode on long-term stability of room-temperature fabricated TiO<sub>2</sub> photoelectrodes (R-TiO<sub>2</sub>). A surface OH group-rich R-TiO<sub>2</sub> photoelectrode was prepared by electrospray method and was found to exhibit poor long-term stability (34.8% of its initial efficiency after 1000 h at 60°C under illumination of 100 mWcm<sup>-2</sup>) due to the desorption of adsorbed dye molecules from the R-TiO<sub>2</sub> surface. We found that large amounts of N719 dye on the R-TiO<sub>2</sub> surface were weakly anchored with one carboxylic acid as a result of rapid adsorption of dye by excess surface OH groups on R-TiO<sub>2</sub> surface. The loss of weakly adsorbed N719 from the R-TiO<sub>2</sub> surface could be suppressed by the addition of stearic acid (SA) to the dye solution as co-adsorbents during the dye

anchoring process (RS-TiO<sub>2</sub>). The competitive adsorption of SA and N719 on the surface Ti-OH groups slowed the adsorption rate of N719, which decreased the amount of weakly bound N719 present on the RS-TiO<sub>2</sub> surface. The RS-TiO<sub>2</sub> device exhibited a high resistance to dye desorption and displayed enhanced long-term stability (70.1% of its initial efficiency after 1000 h at 60°C under illumination of 100 mW cm<sup>-2</sup>).

Also, we prepared the co-sensitized TiO<sub>2</sub> photoelectrode using mixed dye solution, including highly efficient organic dye, JH-1, and near IR squaraine dye, SQ2, to make panchromatic adsorption of TiO<sub>2</sub> photoelectrode. Afterward, the use of mixed dye of JH-1 and SQ2 on HS-TiO<sub>2</sub> photoelectrode, the efficiency of 6.31% was achieved for flexible DSSCs, which is higher than pure JH-1 sensitized DSSCs. We found that increased total amount of adsorbed dye on TiO<sub>2</sub> surface induce higher photocurrent density, resulted in higher PCE of co-sensitized photoelectrode.

Finally, we fabricated flexible piezoelectric nanogenerator using 1-D piezoelectric nanofibers. An electrospun nanofiber-based PbZr<sub>0.52</sub>Ti<sub>0.48</sub> (PZT) textile was used as a flexible piezoelectric nanogenerator, and its performance parameters were investigated. The fiber orientation of electrospun PZT textile was controlled using a multi-pair metal wire or metal mesh. Flexible piezoelectric nanogenerators were assembled by

forming a composite of the textile and a polydimethylsiloxane (PDMS) matrix sandwiched between two flexible ITO-PEN substrates. The assembled nanogenerator could generate an electrical output of 1.1 V at 1.4  $\mu\text{A}$  at a thickness of 80  $\mu\text{m}$  and an area of 8  $\text{cm}^2$  under bending strain. The piezoelectric voltage depended on the thickness of the PZT textile, whereas the piezoelectric current depended on both the thickness and area of the PZT textile. We found that the electrical output of the device was significantly influenced by the orientation of the PZT fiber and the bending direction. The output voltage and current were strain-dependent, whereas the total integrated charge was strain rate-independent. The characteristics of the flexible nanogenerator quantified the device performance.

**KEYWORDS:** Flexible Energy Harvester, Nanostructured Materials, Solar Cells, Piezoelectric Nanogenerator, Electrospray, Electrospinning, PZT,  $\text{TiO}_2$ , Organic dye, Long-term stability, Dye-adsorption, Composite layer, Charge transport, Low-temperature process, Fiber orientation, PDMS

**Student Number: 2009-20634**

# Contents

<b>Abstract</b> .....	<b>i</b>
<b>Contents</b> .....	<b>vi</b>
<b>List of Tables</b> .....	<b>xi</b>
<b>List of Figures</b> .....	<b>xiii</b>

## Chapter 1

<b>Introduction</b> .....	<b>1</b>
1.1 Energy harvester.....	1
1.2 Fundamentals of Flexible Dye-Sensitized Solar Cells (DSSCs) .....	5
1.3 Fundamentals of Flexible Piezoelectric Nanogenerator (NG) .....	15
1.4 Electrospray.....	20
1.5 Electrospinning.....	25
1.6 Research Objective.....	28
1.7 Reference.....	33

## Chapter 2

**Low-temperature fabrication of TiO<sub>2</sub> electrodes for flexible dye-sensitized solar cells using an electro-spray process..... 38**

2.1 Introduction .....38

2.2 Experimental .....43

    2.2.1 Materials .....43

    2.2.2 Preparation of the HS-TiO<sub>2</sub> Electrode .....44

    2.2.3 TTB treatment.....44

    2.2.4 Device Fabrication.....45

    2.2.5 Characterization of the Flexible DSSCs.....46

2.3 Results and discussion.....49

    2.3.1 Morphological Changes in the HS-TiO<sub>2</sub>.....49

    2.3.2 Photovoltaic Performance upon Compression Treatment .....55

    2.3.3 Thickness dependence of the as-pressed HS-TiO<sub>2</sub> electrode.....63

    2.3.4 TTB treatment after Compression Treatment .....67

2.4 Conclusion.....72

2.5 References .....74

**Chapter 3**

**Enhanced long-term stability of room-temperature fabricated DSSCs by stabilized binding of N719 dye ..... 78**

3.1 Introduction .....	78
3.2 Experimental .....	82
3.2.1 Preparation of TiO <sub>2</sub> photoelectrodes.....	82
3.2.2 Device Fabrication.....	83
3.2.3 UV-Vis spectroscopy measurement.....	85
3.2.4 ATR FT-IR spectroscopy measurement.....	85
3.2.5 Photovoltaic characterization .....	86
3.3 Results and discussion.....	87
3.3.1 Initial efficiency.....	87
3.3.2 Long-term stability .....	95
3.3.3 Binding mode of N719 on H-TiO <sub>2</sub> and R-TiO <sub>2</sub> electrode .....	102
3.3.4 Effects of stearic acid (SA) on the efficiency and durability...	106
3.3.5 Stabilized binding mode of N719 dye by addition of SA .....	111
3.4 Conclusion.....	113
3.5 References .....	114

## **Chapter 4**

### **Highly efficient photon harvesting by cosensitization for flexible dye-sensitized solar cells ..... 122**

4.1 Introduction .....	122
4.2 Experimental .....	125
4.2.1 Materials .....	125

4.2.2 Preparation of the HS-TiO <sub>2</sub> Electrode .....	126
4.2.3 Device Fabrication.....	127
4.2.4 Amount of adsorbed dye measurement .....	128
4.2.5 Characterization of the DSSCs .....	128
4.3 Results and discussion.....	130
4.3.1 Absorption spectra of mixed dye solution .....	130
4.3.2 Absorption spectra of co-sensitized TiO <sub>2</sub> films .....	133
4.3.3 Photovoltaic characteristics of co-sensitized device .....	139
4.4 Conclusion.....	149
4.5 References .....	150

## **Chapter 5**

### **Anisotropic piezoelectric generation of highly oriented PZT nanofibers for a flexible nanogenerator .....**

**155**

5.1 Introduction .....	155
5.2 Experimental .....	158
5.2.1 Preparation of the PZT nanofiber textiles.....	158
5.2.2 Device Fabrication.....	159
5.2.3 Characterization.....	160
5.3 Results and discussion.....	161
5.3.1 Morphologies of electrospun PZT nanofibers .....	161
5.3.2 Structure of assembled flexible nanogenerator .....	165

5.3.3 Piezoelectric Generation – Thickness and area dependence ...	172
5.3.4 Piezoelectric Generation – Bending orientation dependence ..	176
5.3.5 Piezoelectric Generation – Strain and Strain rate dependence	179
5.4 Conclusion.....	185
5.5 References .....	186

## **Chapter 6**

<b>Conclusion .....</b>	<b>192</b>
6.1 Overall Conclusion.....	192
6.2 Further works .....	196
<b>Korean Abstract .....</b>	<b>198</b>
<b>List of Publications.....</b>	<b>202</b>

## List of Tables

**Table 2.1** Physical characteristics of as-sprayed and as-pressed HS-TiO<sub>2</sub> particles

**Table 2.2** Photovoltaic properties of the DSSCs using as-sprayed, as-pressed and TTB-treated HS-TiO<sub>2</sub> photoelectrode with a film thickness of 9 μm

**Table 2.3** Summary of photovoltaic performance of DSSC prepared with photoelectrode with as-pressed HS-TiO<sub>2</sub> films of various thickness

**Table 3.1** Photovoltaic properties of the H-TiO<sub>2</sub>, R-TiO<sub>2</sub>, and RS-TiO<sub>2</sub> photoelectrode with a TiO<sub>2</sub> film thickness of 9 μm as function of aging time

**Table 3.2** Summary of the amount of adsorbed N719 dye on each TiO<sub>2</sub> photoelectrodes with different aging time at 60°C under illumination of 100 mW cm<sup>-2</sup>

**Table 4.1** Concentration of individual dye loaded onto the flexible TiO<sub>2</sub> electrode for various molar ratio of dye cocktail solution.

**Table 4.2** Photovoltaic parameters of the flexible DSSCs with different dye concentration.

**Table 5.1** Output signals obtained from the flexible piezoelectric nanogenerators prepared with different thicknesses and areas

# List of Figures

**Figure 1.1** Structure and operating principle of the DSSC

**Figure 1.2** Photocurrent-voltage curve of the dye-sensitized solar cell

**Figure 1.3** Incident photon-to-electron conversion efficiency (IPCE) of Ru-sensitizers as a function of wavelength

**Figure 1.4** Orientation of dipoles by polarization, (a) random orientation of polar domains, (b) application of high DC electric field (polarization), (c) remnant polarization after the electric field is extinguished.

**Figure 1.5** Schematic of direct piezoelectric effect; (a) piezoelectric material, (b) energy generation under tension, (c) energy generation under compression

**Figure 1.6** Schematic of converse piezoelectric effect; (a) piezoelectric material, (b) dimensional change when an electrical charge applied, (c) dimensional change when an opposite electrical charge applied.

**Figure 1.7** Schematic illustration of basic setup for electrospray

**Figure 1.8** Schematic illustration of basic setup for electrospinning

**Figure 2.1** SEM images of (a) and (b) as-sprayed, (c) as-pressed, and (d) TTB-treated HS-TiO<sub>2</sub> photoelectrode

**Figure 2.2** Pore volume distribution of as-sprayed and as-pressed HS-TiO<sub>2</sub>

particles

**Figure 2.3** J-V curves (a) and IPCE spectra (b) of the DSSCs based as-sprayed and as-pressed HS-TiO<sub>2</sub> photoelectrodes

**Figure 2.4** Typical IMPS (a) and IMVS (b) plots of the DSSCs based as-sprayed and as-pressed HS-TiO<sub>2</sub> photoelectrodes

**Figure 2.5** Electron diffusion coefficient (a) and recombination lifetime (b) of the DSSCs based as-sprayed, as-pressed, and TTB-treated HS-TiO<sub>2</sub> photoelectrodes as a function of the incident photonflux for 446 nm modulated (<10%) laser illumination

**Figure 2.6** Photovoltaic properties of DSSCs prepared with photoelectrodes with as-pressed HS-TiO<sub>2</sub> films of various thicknesses

**Figure 2.7** XRD diffraction patterns of air-dried TTB (a) and hot water-treated TTB (b)

**Figure 3.1** (a), (b) SEM images of hierarchically structured R-TiO<sub>2</sub> photoelectrode and (c) Initial J-V characteristics of H-TiO<sub>2</sub>, R-TiO<sub>2</sub>, and RS-TiO<sub>2</sub> photoelectrodes

**Figure 3.2** ATR-FTIR spectra of P25 pristine TiO<sub>2</sub> powder (dashed green), H-TiO<sub>2</sub> (solid black) and R-TiO<sub>2</sub> (solid blue), bare electrodes

**Figure 3.3** Electron diffusion coefficients (a) and recombination lifetime (b) of the DSSCs based H-TiO<sub>2</sub>, and R-TiO<sub>2</sub> photoelectrodes as a function of incident photon flux for 446 nm modulated (<10%) laser illumination.

**Figure 3.4** (a) Normalized amounts of adsorbed dye on each TiO<sub>2</sub> surface in 0.3 mM N719 solution as a function of adsorption time and (b) aging time at 60°C under illumination of 100 mW cm<sup>-2</sup>. Y-axis is normalized by saturation amount of adsorbed dye on TiO<sub>2</sub> surface

**Figure 3.5** (a) Power conversion efficiencies (PCE) and (b) normalized PCE of H-TiO<sub>2</sub>, R-TiO<sub>2</sub>, and RS-TiO<sub>2</sub> photoelectrodes as a function of aging time

**Figure 3.6** Photographs of the N719-sensitized H-TiO<sub>2</sub> (top), R-TiO<sub>2</sub> (middle), and RS-TiO<sub>2</sub> (bottom) after aging

**Figure 3.7** Relative ATR FT-IR spectra of the TiO<sub>2</sub> electrodes sensitized 0.3 mM of N719 (H-TiO<sub>2</sub> and R-TiO<sub>2</sub>) and sensitized 0.3 mM of N719 with 3 mM of stearic acid (RS-TiO<sub>2</sub>). All spectra were normalized by the amount of adsorbed dye on each TiO<sub>2</sub> surface for quantitative analysis at the signal of 1540 cm<sup>-1</sup> (bipyridyl n(C=C) adsorption from N719 molecules).

**Figure 3.8** Plausible binding mode of N719 on (a) H-TiO<sub>2</sub> surface, (b) R-TiO<sub>2</sub>, and (c) RS-TiO<sub>2</sub> surface

**Figure 4.1** Molecular structures of (a) JH-1, (b) SQ2, and (c) absorption spectra of mixed dye solution with different molar ratio in ethanol.

**Figure 4.2** (a) Photograph images and (b) absorption spectra of co-sensitized TiO<sub>2</sub> films with different cocktail dye solution.

**Figure 4.3** Normalized dye concentrations onto the flexible TiO<sub>2</sub> photoelectrode as a function of dipping times. The calculated values are the average of sample from three TiO<sub>2</sub> electrodes. Inset plot is dye coverage ( $\theta$ ) versus adsorption time based on pseudo-first-reaction of each dye onto the flexible TiO<sub>2</sub> photoelectrode.

**Figure 4.4** Dye concentrations on flexible TiO<sub>2</sub> film as a function of molar ratio in dye cocktail solution.

**Figure 4.5** J-V curves of the co-sensitized flexible DSSCs with different dye concentration.

**Figure 4.6** The IPCE spectra of the co-sensitized flexible DSSCs with different dye concentration.

**Figure 4.7** Calculated photocurrent density with different dye concentration as a function of the dye molar ratio in the solution.

**Figure 4.8** Photovoltaic properties of (a) flexible DSSCs co-sensitized with molar ratio of 6:4 (JH1/SQ2) as a function of TiO<sub>2</sub> thicknesses and (b) J-V characteristics of JH-1/SQ2 and N719-sensitized device.

**Figure 5.1** (a) Schematic diagram showing the process of fabricating the aligned PZT textiles by electrospinning onto multi-pair metal wire collectors.

(b and c) SEM images of the PZT textile prepared with a parallel orientation and the randomly oriented PZT textile, respectively.

**Figure 5.2** (a) XRD pattern of a calcined PZT textile. (b) TEM image of a single PZT nanofiber. (c) High-resolution TEM image of a PZT nanofiber. The inset image shows a SAED pattern of a PZT nanofiber.

**Figure 5.3** (a) Structural illustration of the flexible piezoelectric nanogenerator. (b and c) Photographic images of the devices assembled on a measurement station without deformations or with deformations, respectively.

**Figure 5.4** Piezoelectric voltage (a) and current (b) of PDMS-only nanogenerator.

**Figure 5.5** Piezoelectric voltage (a) and current (b) as a function of applied electric field

**Figure 5.6** (a and c) Output voltage and current under the forward connection. (b and d) Output voltage and current under the reverse connection.

**Figure 5.7** (a) Output voltage, and (b) current measured in a single layer PZT nanogenerator, as a function of the PZT layer thickness. The area of the PZT was 4 cm<sup>2</sup>. (c) The output voltage and (d) current measured in the two-layer PZT nanogenerator as a function of the thickness. The area of the PZT

was  $4 \text{ cm}^2$ . (e) The output voltage and (f) current of a two-layer PZT nanogenerator prepared with different areas. The thickness of each PZT was  $40 \text{ }\mu\text{m}$  (total  $80 \text{ }\mu\text{m}$ ).

**Figure 5.8** (a) Schematic diagram showing a flexible PZT nanogenerator embedded in different PZT textiles. (b) Output voltage and (c) current measured from three different nanogenerators under identical measurement conditions.

**Figure 5.9** Strain dependence of (a) the output voltage and (b) the output current as a function of the strain for three different nanogenerators.

**Figure 5.10** Strain rate dependence of (a) the output voltage and (b) the current of a flexible PZT nanogenerator. (c) Output current and (d) integrated charge of a flexible nanogenerator subject to two different strain rates under the same applied strain. Here, the device was assembled using a two-layer PZT nanogenerator ( $80 \text{ }\mu\text{m}$  and  $4 \text{ cm}^2$ ), and measurements were collected under an applied strain of  $0.18\%$ .

# Chapter 1

## 1. Introduction

### 1.1 Energy Harvester

With the growing threat of pollution, global warming, and energy crises caused by our strong dependence on the dwindling supply of nonrenewable fossil fuels, the search for clean and renewable alternative energy resources is one of the most urgent challenges to the sustainable development of human civilization.[1] In addition to the energy resources which drive human society today, such as petroleum, coal, hydraulic power, natural gas, wind power, and nuclear plants, a focus of active research and development is the exploration of alternative sustainable energy resources, such as solar energy,[2] geothermal power,[3] biomass/biofuel,[4] and hydrogen energy.[5] Although there is potential for the use of these alternative sources for the large-scale supply of power, the energy that can be harvested from these sources is still mainly used for small-scale powering applications.

There are a variety of sources available for energy scavenging by

micro/nano-scale devices system (MNS) from the ambient environment, including, but not limited to, energy in natural forms, such as wind, water flow, ocean waves, and solar power; mechanical energy, such as vibrations from machines, engines, and infrastructures; thermal energy, such as waste heat from heaters and joule heating of electronic devices; light energy from both domestic/city lighting and outdoor sunlight; and electromagnetic energy from inductor coils/transformers as well as from mobile electronic devices. Moreover, the human body itself provides a tremendous amount of energy that is available for harvesting and potential utilization in self-powered MNSs: mechanical energy due to vibration/motion from body movement, respiration, and even blood flow in vessels; thermal energy from body heat; and biochemical energy generated during physiological processes and metabolic reactions. In this research, we focused on solar energy for flexible Dye-Sensitized Solar Cells (DSSCs) and mechanical energy for flexible Piezoelectric Nanogenerator (NG) with nanostructured materials.

### **1.1.1 Solar Energy for Flexible DSSCs**

Solar energy is by far the most abundant exploitable renewable energy resource. More energy is provided to the earth by sunlight irradiation within

one hour than is consumed by human society globally in one year.[6] Semiconductor materials that exhibit a photovoltaic (PV) effect can be used to convert solar radiation into electricity through a photovoltaic process. PV technology has been growing and expanding rapidly. The total global energy production by PV processes reached 64 GW (1 GW=10<sup>9</sup> W) by the end of 2011.[7] Despite this considerable capacity, however, PV technology only accounts for 0.1 % of electricity generation globally,[8] largely as a result of the inability of existing PV technologies to produce electricity with an efficiency that fulfils the grid parity set by conventional power-generation routes.[9] Enormous efforts and resources have therefore been devoted to the development of new-generation PV technologies that operate with enhanced efficiency at lower cost.

Practically all PV devices, or solar cells, incorporate a p–n junction. Such junctions occur in various possible configurations. Solar cells containing multiple p–n junctions have recently been investigated intensively for the more efficient absorption of light with different wavelengths with the aim of reducing the inherent sources of energy loss in conventional single-junction cells. A conversion efficiency of 42.3 % was achieved by combining multijunction cells and concentrator technology.[10] However, the high efficiency of multijunction cells is offset by their

increased complexity and manufacturing cost, which limit their application mainly to aerospace exploration, for which a high power-to-weight ratio is desirable. The dominance of PV technology historically by inorganic solid-state junction devices is now being challenged by the emergence of a new generation of PV technologies built, for example, on nanostructured materials or conducting polymers. Such technologies offer the prospect of converting solar energy into electricity at low cost. Subsequent discussions on solar-energy harvesting are focused on micro-/nanotechnology-enabled PV technologies and their potential applications in MNSs.

### **1.1.2 Mechanical Energy for Flexible Piezoelectric NG**

Vibration-based mechanical energy is ubiquitous in the environment and more accessible than solar and thermal energy. Mechanical vibrations with frequencies spanning a broad spectrum, from a few hertz to several kilohertz, exist abundantly in the ambient, with available energy density ranging from a few hundred microwatts to milliwatts per cubic centimeter.[11] This energy can potentially facilitate the continuous and adaptable operation of sensors as well as electronic devices and systems, especially under circumstances in which other energy sources, such as solar or thermal

energy, are not readily available.[12] Several methods have been developed for the conversion of mechanical energy into electricity through the use of electromagnetic induction, static-electricity generation, and piezoelectric materials.[13] The harvesting of mechanical energy by piezoelectric materials in particular has received enormous attention owing to the ability of these materials to convert mechanical energy into electricity directly and the feasibility of this approach for integrated applications. Traditionally, lead zirconate titanate, or PZT, has been the material used most for mechanical-energy harvesting.[14] Nevertheless, the extremely brittle nature of PZT ceramic and the incorporation of lead create issues such as the reliability, durability, and safety of this material for long-term sustainable operation and hinder its application.

## **1.2 Fundamentals of Dye-Sensitized Solar Cells (DSSCs)**

Ever since the invention of the silicon solar cell in the 1940s, people have acknowledged the enormous potential of photovoltaic systems for large scale electricity production. However, semiconductor grade silicon wafers are expensive so great effort has been put into developing cheaper thin-film solar cells and modules. Such films may be purely inorganic

(amorphous silicon, cadmium telluride, copper-indium-diselenide) or contain organic materials as an essential part of the device.[15]

Dye-sensitized solar cells (DSSCs) have been attracting intensive interest for scientific research and industrial applications because of their high photon-to-electricity conversion efficiency and low cost compared with traditional photoelectrochemical cells.[16] Dye-sensitized solar cells (DSSCs) convert visible light energy to electrical energy through charge separation in sensitizer dyes adsorbed on a wide band gap semiconductor. Energy conversion from dye-sensitized  $\text{TiO}_2$  electrode immersed in an electrolyte was reported by Vlachopoulos [17] in 1988. Although the charge separation was able to occur at high efficiency, energy conversion efficiency was not high because of low light absorption coefficient of the solar cells. This was because the dyes were adsorbed onto a relatively flat surface of the semiconductor electrode, and light absorption by the monolayer of the dye was limited. In 1991, O'Regan and Grätzel [16] solved the issue by employing nanoporous  $\text{TiO}_2$  electrode. Since the electrode has huge surface area per projected area, solar cells made from the dye-adsorbed nanoporous  $\text{TiO}_2$  can drastically increase effective light absorption. By designing proper electrode thickness and sensitization dyes, DSSCs are able to absorb most of the visible light. The current highest energy conversion efficiency is over

11%,[18] and further increase of the efficiency is possible.

DSSC comprises a dye-sensitized nanoporous  $\text{TiO}_2$  electrode on transparent conducting oxide (TCO) electrode, electrolytes containing  $\text{I}^-/\text{I}_3^-$  redox couple filling the pore of the electrode, and a platinum counter electrode placed on the top of the  $\text{TiO}_2$  electrode. Figure 1.1 indicates the schematic structure and operating principle of the DSSC. Under the illumination of sunlight, photons enter through the photoactive electrode and can be absorbed by sensitizer molecules (S) at various depths in the film (1). The sensitizer molecules ( $\text{S}^*$ ) excited in this way inject electrons into the conduction band (CB) of the adjacent  $\text{TiO}_2$  particles ( $e_{\text{CB}}^-$ ), leaving an oxidized sensitizer molecule ( $\text{S}^+$ ) on the  $\text{TiO}_2$  surface (2). The injected electrons percolate through via the interconnected  $\text{TiO}_2$  particles to the TCO substrate and are fed into an electrical circuit, where work can be delivered (3). The oxidized sensitizer is reduced by the electron donor (I) present in the electrolyte, filling the pores (4). The triiodide ( $\text{I}_3^-$ ) produced in this way diffuses to the counter electrode, where it is reduced back to iodide by metallic platinum under uptake of electrons from the external circuit (5).[19]

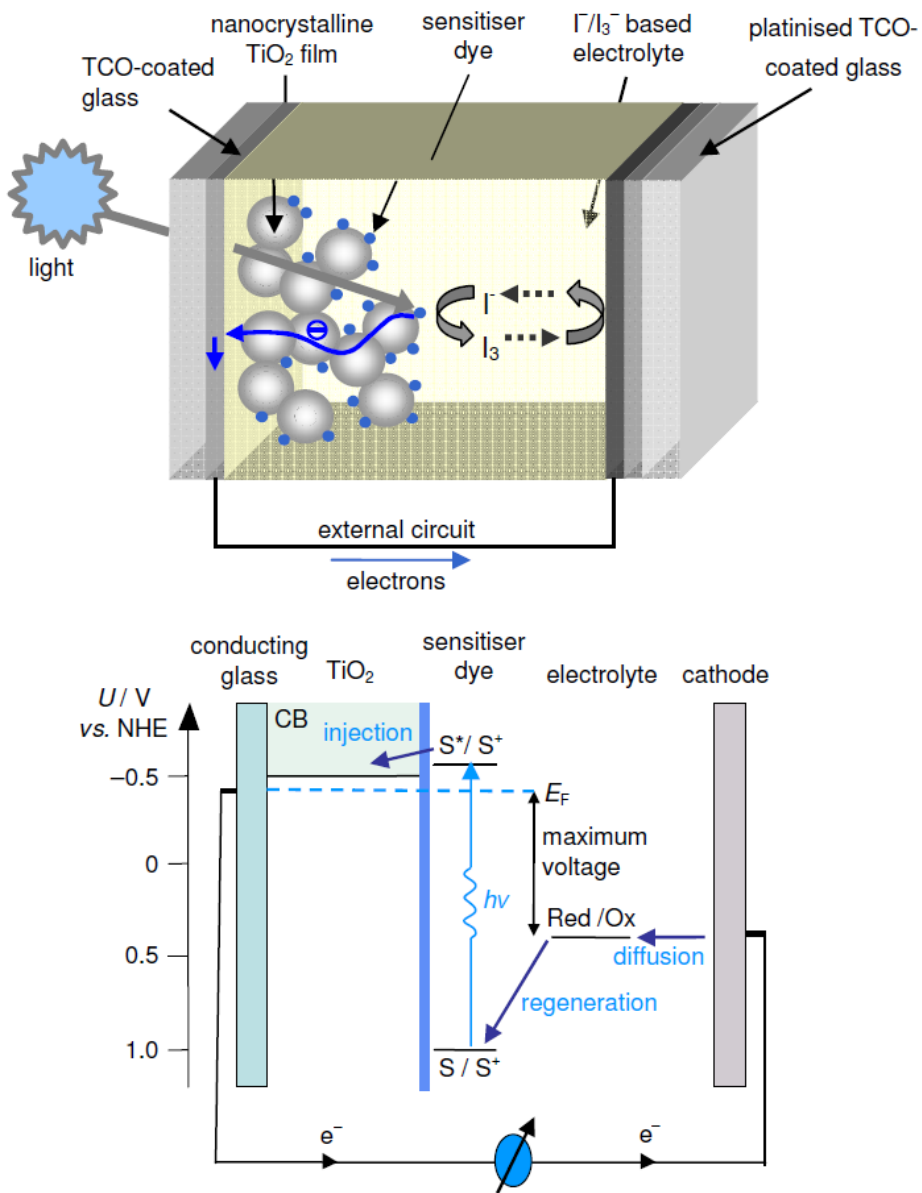


**Figure 1.1** Structure and operating principle of the DSSC



We describe briefly the parameters used to characterize the performance of photovoltaic devices. Figure 1.2 shows a schematic diagram of the photocurrent-voltage curves under illumination. Devices are generally characterized by the short-circuit current ( $J_{sc}$ ), open-circuit voltage ( $V_{oc}$ ), fill factor (FF). The short-circuit current ( $J_{sc}$ ) corresponds to the short-circuit condition when the impedance is low and is calculated when the voltage equals zero (0). The open-circuit voltage ( $V_{oc}$ ) occurs when there is no current passing through the cell. The power produced by the cell in Watts can be easily calculated along the J-V sweep by the equation  $P=IV$ . At the  $J_{sc}$  and  $V_{oc}$  points, the power will be zero and the maximum value for power will occur between the two. The voltage and current at the maximum power point are denoted as  $V_{max}$  and  $J_{max}$  respectively. The fill factor (FF) is essentially a measure of quality of the solar cell. It is calculated by comparing the maximum power to the theoretical power ( $P_T$ ) that would be

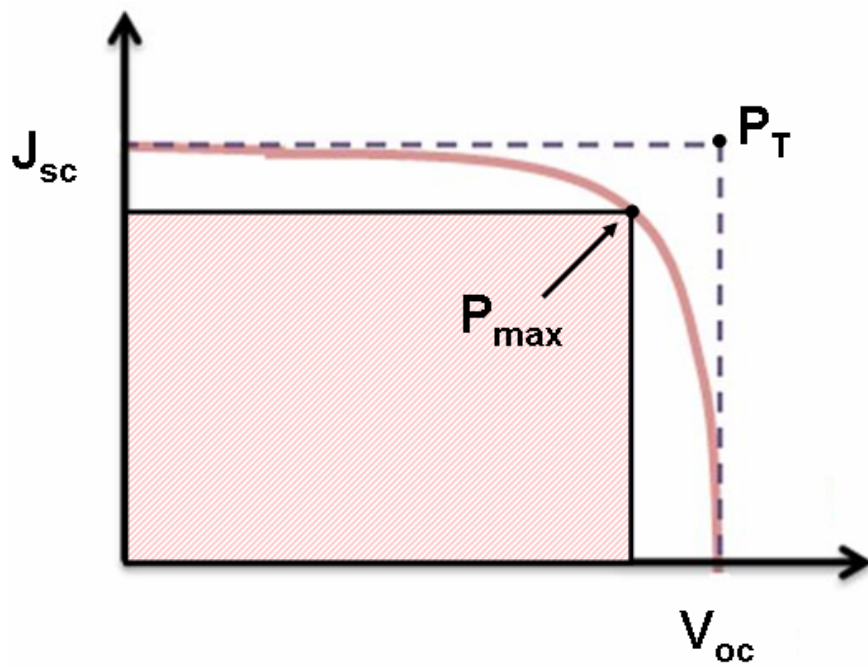


**Figure 1.2** Photocurrent-voltage curve of the dye-sensitized solar cell

output at both the  $V_{oc}$  and  $J_{sc}$  together. FF can also be interpreted graphically as the ratio of the rectangular areas depicted in Figure 1.2. A commonly used expression for the FF was the same as followed equation.

$$FF = \frac{P_{max}}{P_T} = \frac{V_{max} \times J_{max}}{V_{oc} \times J_{sc}}$$

A larger FF is desirable, and corresponds to a J-V sweep that is more square-like. Typically FFs range from 0.5 to 0.82. Fill factor is also often represented as a percentage. Efficiency is the ratio of the electrical power output  $P_{out}$ , compared to the solar power input,  $P_{in}$ , into the solar cell.  $P_{out}$  can be taken to the  $P_{max}$  since the solar cell can be operated up to its maximum power output to get the maximum efficiency. Efficiency,  $\eta$ , under illumination (e.g. AM1.5) can be obtained by the following equation.

$$\eta = \frac{P_{out}}{P_{in}} = \frac{J_{sc} (mAcm^{-2}) \times V_{oc} (V) \times FF}{P_{in}}$$

$P_{in}$  is taken as the product of the irradiance of the incident light, measured in  $mWcm^{-2}$  or 1 sun ( $100 mWcm^{-2}$ ), with the area of the solar cell ( $cm^2$ ).

The spectral response of photovoltaic cells is an important way to characterize such devices and optimize their performance. The device is illuminated by a monochromatic light source, generally consisting of a broadband illuminator dispersed through a monochromator. The incident

monochromatic photon-to-current conversion efficiency (IPCE), defined as the number of electrons generated by light in the external circuit divided by the number of incident photons as a function of excitation wavelength is expressed by the following equation.

$$IPCE = \frac{1240(eV \cdot nm) \times J_{sc} (mAcm^{-2})}{\lambda(nm) \cdot \Phi(mAcm^{-2})}$$

where  $J_{sc}$  is the short-circuit photocurrent density for monochromatic irradiation,  $\lambda$  is the wavelength, and  $\Phi$  is the monochromatic light intensity. As shown in Figure 1.3, solar cells sensitized by the Ru complex photosensitizers can efficiently convert visible light to current. The most widely used Ru complexes,[26-28] N3 dye ( $RuL_2(NCS)_2$ ) can absorb over a wide range of the visible regions from 400 to 800 nm. Black dye ( $RuL'(NCS)_3$ ) absorbs in the near-IR region up to 950 nm. IPCE's of around 80% at the absorption maximum of the dye have been reported for several Ru complex photosensitizer dyes on about 10  $\mu m$  thick nanocrystalline  $TiO_2$  films.[26,29] However, such high IPCE's correspond to almost 100% efficient collection because around 20% of the light is lost by absorption in the  $SnO_2$  layer, by reflection and scattering.

In recent years, plastic flexible DSSC based on a transparent conducting polymer has attracted a lot of interest because of their lightweight, flexibility,

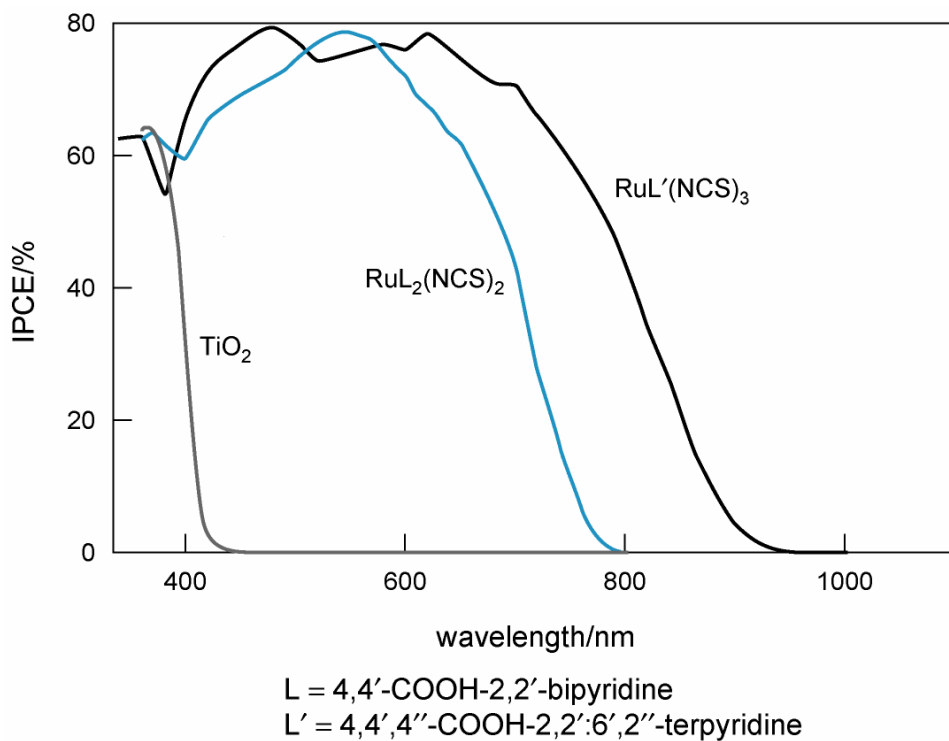


**Figure 1.3** Incident photon-to-electron conversion efficiency (IPCE) of Ru-sensitizers as a function of wavelength

and low cost production. Unlike glass-based DSSC, the entire manufacturing process with plastic substrates should be carried out at low temperature, as well as employ kinetically favorable polymer electrolytes.[30] Nanocrystalline  $\text{TiO}_2$  electrodes for DSSC have usually been prepared by coating an organic binder containing  $\text{TiO}_2$  paste on glass substrates, followed by heating at temperatures ranging from  $450^\circ\text{C}$  to  $500^\circ\text{C}$ . The organic binder is used to increase viscosity, enabling the forming of thick  $\text{TiO}_2$  films, and heat treatment is used to sinter nanoparticles, as well as burn out the organic binder. In case of a plastic substrate, however, conventional preparation technology is not suitable because of the low temperature resistance of plastics; temperature in excess of  $150^\circ\text{C}$  cannot be used. Accordingly the preparation of nanocrystalline  $\text{TiO}_2$  films with good connections between  $\text{TiO}_2$  nanoparticles at low temperatures less than  $150^\circ\text{C}$  becomes a key issue.

## **1.3 Fundamentals of Flexible Piezoelectric Nanogenerator**

**(NG)**

Vibration-based mechanical energy is ubiquitous in the environment and more accessible than solar and thermal energy. Mechanical vibrations with frequencies spanning a broad spectrum, from a few hertz to several kilohertz, exist abundantly in the ambient, with available energy density ranging from a few hundred microwatts to milliwatts per cubic centimeter.[31] This energy can potentially facilitate the continuous and adaptable operation of sensors as well as electronic devices and systems, especially under circumstances in which other energy sources, such as solar or thermal energy, are not readily available.[32] Several methods have been developed for the conversion of mechanical energy into electricity through the use of electromagnetic induction, static-electricity generation, and piezoelectric materials.[33] The harvesting of mechanical energy by piezoelectric materials in particular has received enormous attention owing to the ability of these materials to convert mechanical energy into electricity directly and the feasibility of this approach for integrated applications.

Piezoelectric behaviour was first found in some crystals. According to historical reviews on piezoelectricity [3-4] Charles Coloumb was the first

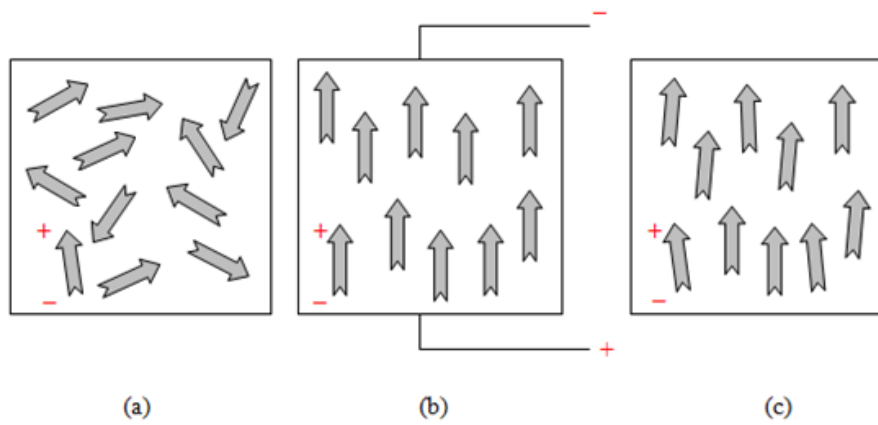
person who theorized in 1817 that electricity may be produced by the application of pressure to certain types of materials. However, it was only a notion until the actual discovery of the “direct-piezoelectric phenomenon” on quartz by Pierre and Jacque Curie.[5] They placed weights on the crystals and detected some charges on the surface and also observed that the magnitude of detected charge was proportional to the applied weight.

Piezoelectric effect exists in two domains; namely, direct piezoelectric effect and converse piezoelectric effect. Direct piezoelectric effect describes the ability to convert mechanical energy to electrical energy which is also known as generator or transducer effect while the converse piezoelectric effect describes the ability of transforming electrical energy to mechanical energy which is also known as motor/actuator effect. The electrical energy generated by direct piezoelectric effect can be stored to power electronic devices and it is known as “energy/power harvesting”.

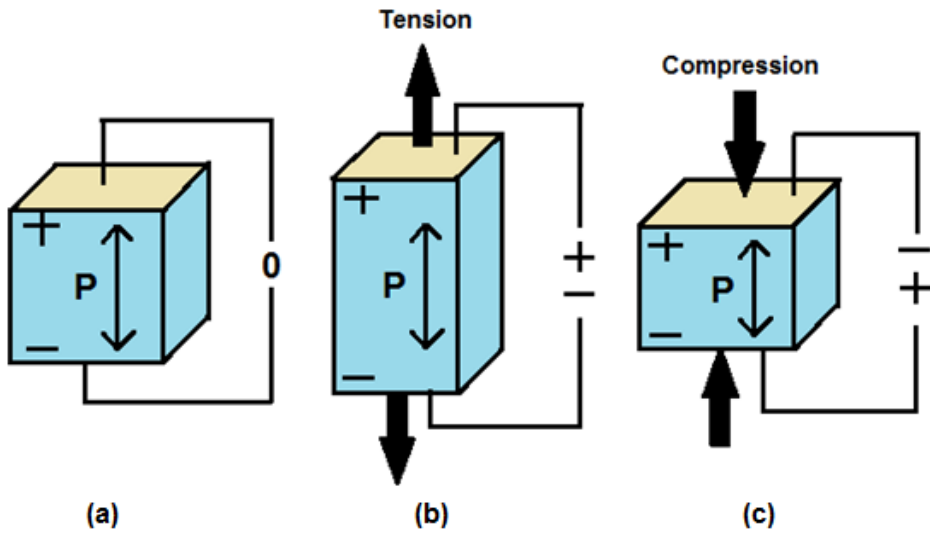
Piezoelectric materials are member of ferroelectrics so that the molecular structure is oriented such that the material exhibits a local charge separation, known as electric dipole. Electric dipoles in the artificial piezoelectric materials composition are randomly oriented, so the material does not exhibit the piezoelectric effect. However, the electric dipoles reorient themselves when a strong electrical field is applied as shown in

Figure 1.4. The orientation is dependent on the applied electrical field which is known as poling. Once the electric field is extinguished, the dipoles maintain their orientation and the material then exhibit the piezoelectric effect so that an electrical voltage can be recovered along any surface of the material when the material is subjected to a mechanical stress.[37] However, the alignment of the dipole moments may not be perfectly straight because each domain may have several allowed directions. The piezoelectric property gained is stable unless the material is heated to or above its Curie temperature ( $T_C$ ). However, it can be cancelled by the application of an electric field that is opposite to the direction of the material.

According to the definition of “direct piezoelectric effect”, when a mechanical strain is applied to crystals by an external stress, an electric charge occurs on the surface(s) of the crystal and the polarity of this observed electric charge on the surface(s) can be reversed by reversing the direction of the mechanical strain applied as shown in Figure 1.5. On the other hand, according to the definition of “converse piezoelectric effect”, when an electric field is applied to a crystal or a crystal is subjected to an electric field, a mechanical deformation on the surface is observed which is generally seen as a change in dimensions of the crystal. The direction of the mechanical strain can also be reversed as shown in Figure 1.6, by reversing



**Figure 1.4** Orientation of dipoles by polarization, (a) random orientation of polar domains, (b) application of high DC electric field (polarization), (c) remnant polarization after the electric field is extinguished.



**Figure 1.5** Schematic of direct piezoelectric effect; (a) piezoelectric material, (b) energy generation under tension, (c) energy generation under compression

the applied electric field.

## 1.4 Electrospray

Electrospraying is a well-known method of liquid atomization via electrical forces. These techniques (e.g. electrospraying and electrospinning) involve the use of a high potential to induce the formation of a liquid jet.[15] Electrospraying is a process of simultaneous droplet generation and charging by means of electric field. In this process, liquid flowing out from a capillary nozzle maintained at high potential, is subjected to an electric field, which causes elongation of the meniscus to a form of jet or spindle. The jet deforms and disrupts into droplets due to mainly to electrical force. The droplets obtained by this method can be extremely small, in special cases down to nanometers. In this process, droplets are highly charged, up to a fraction of the Rayleigh limit.[16] The Rayleigh limit is the magnitude of charge on a drop, which overcomes the surface tension force that leads to the drop fission. This charge is given by the following equation:

$$E_{Rayleigh} = \frac{2}{3} \cdot \frac{\epsilon_r + 2}{\epsilon_r} \cdot \sqrt{\frac{\sigma}{\epsilon_0 \cdot 0.5 \cdot d_0}}$$

Where  $\epsilon_0$  and  $\epsilon_r$  are permittivities of free space and the solution,  $d_0$  is the

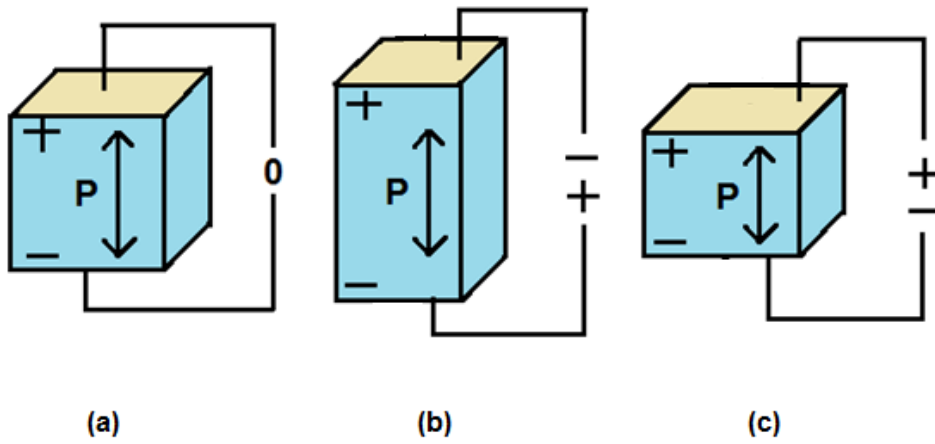


**Figure 1.6** Schematic of converse piezoelectric effect; (a) piezoelectric material, (b) dimensional change when an electrical charge applied, (c) dimensional change when an opposite electrical charge applied.

droplet diameter, and  $\sigma$  is the liquid surface tension.[17]

The charge and size of the droplets can be controlled to some extent by adjusting the liquid flow rate and the voltage applied to the nozzle.

The electrospraying has some advantages over conventional mechanical spraying systems with droplets charged by induction: [18]

1. Droplets have size smaller than those available from conventional mechanical atomizers, and can be smaller than 1  $\mu\text{m}$ .
2. The size distribution of the droplets is usually narrow, with low standard deviation
3. Charged droplets are self-dispersing in the space, those results in absence of droplet agglomeration and coagulation.
4. The motion of charged droplets can be easily controlled (including deflection or focusing) by electric fields.
5. The deposition efficiency of charged spray on an object is much higher than for un-charged droplets.

Figure 1.7 shows a schematic illustration of the basic setup for electrospray. It consists of three major components: a high voltage power supply, a spinneret (a metal capillary), and a collector (a grounded conductor). The spinneret is connected to a syringe in which the spraying solution. The syringe pump is used to feed the solution at a constant and

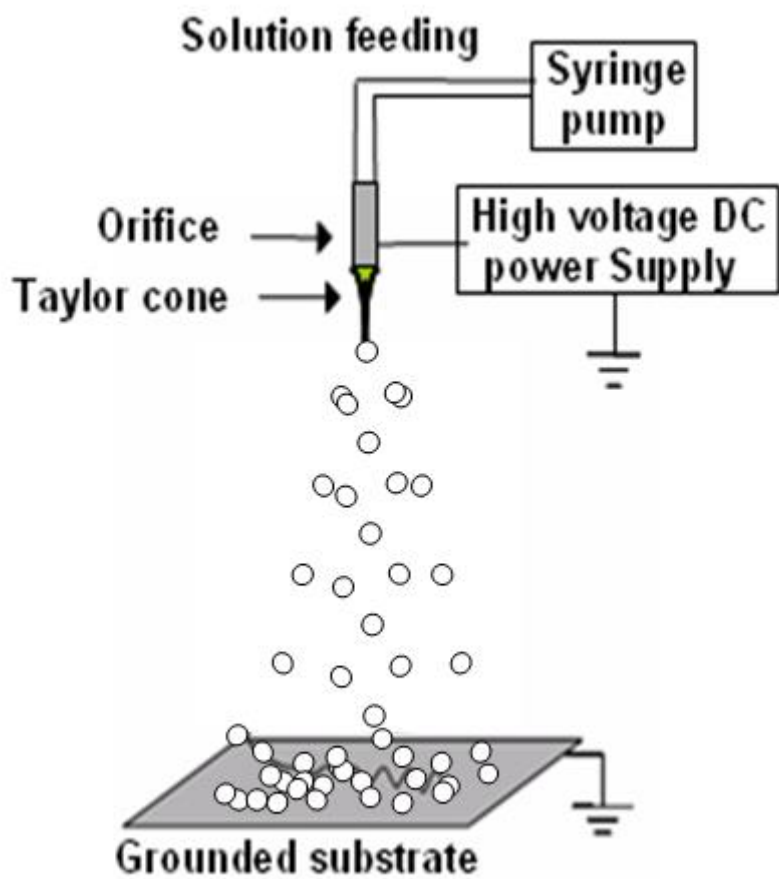


**Figure 1.7** Schematic illustration of basic setup for electrospay

controllable rate. Electrospray method has merits of uniform coating of large areas, inexpensive equipment, operation at atmospheric conditions, and easy control of deposition rate and film thickness by adjusting voltage and feed rate. Advances in electrospray applications will certainly continue in near future, particularly in nanotechnology and biotechnology.

## 1.5 Electrospinning

The formation of nanofibers through electrospinning is based on the uniaxial stretching of a viscoelastic solution. To understand and appreciate the process that enables the formation of various nanofiber assemblies, the principle of electrospinning and the different parameters that affect the process have to be considered. Unlike conventional fiber spinning methods like dry-spinning and melt-spinning, electrospinning makes use of electrostatic forces to stretch the solution as it solidifies. Similar to conventional fiber spinning methods, the drawing of the solution to form the fiber will continue as long as there is enough solution to feed the electrospinning jet. Thus, without any disruption to electrospinning jet the formation of the fiber will be continuous.

The electrospinning process basically consists of syringe to hold the solution, a nozzle, collector and high voltage power supply in the kV range as shown in Figure 1.8. When sufficient voltage is applied to a solution drop, the body of the viscous solution gets charged. As the electrostatic repulsion overcomes the surface tension, the polymer droplet becomes stretched; the liquid streams from the surface erupt at a critical point and the point of eruption is the Taylor cone. If the solution droplet has sufficient

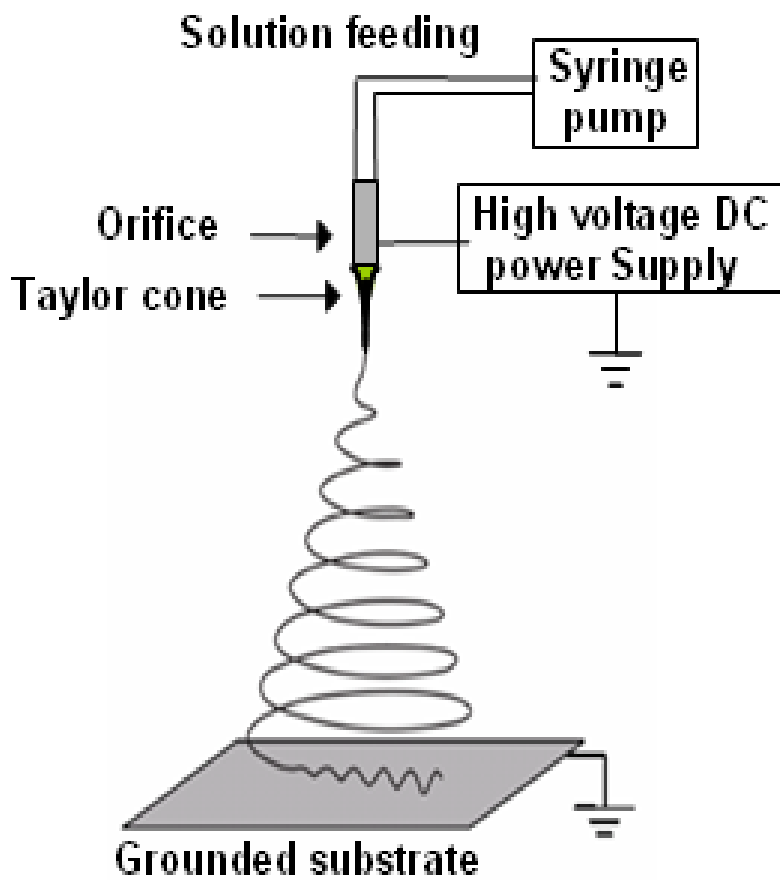


**Figure 1.8** Schematic illustration of basic setup for electrospinning

viscosity, a charged jet is formed. The charge causes the fibers to bend and electrostatic repulsion initiate. It causes a whipping process that elongates the liquid polymer jet. The fibers finally deposited on the collector. The elongation and thinning of the fibers leaded from the bending instability forms uniform fibers with nano or micrometer-scale diameters.[19,20] Electrospinning devices without the use of spinnerets have also been explored by various researchers. Generally, a grounded target is used to collect the resultant fibers which are deposited in the form of a nonwoven mesh. A few widely studied parameters include solution viscosity, conductivity, applied voltage, spinneret tip-to-collector distance and humidity. For example, by reducing the spinneret tip-to-collector distance mesh with inter-connected fibers can be collected, while reducing the solution concentration will reduce the electrospun fiber diameter. Although polymer chain entanglement is an important criterion for fiber formation in polymers, the viscosity of a solution is a more general parameter since ceramic precursor can also be electrospun despite their low molecular weight. To achieve various fiber assemblies, there are generally two main methods, one is to control the flight of the electrospinning jet through the manipulation of the electric field and the other is to use dynamic collection device. Nevertheless, by using different static collection devices, it is

possible to achieve some form of fiber assemblies. To overcome various limitations of the typical electrospinning set-up and to further the performance of the electrospun fibrous mesh, researchers have come out with other modification to the set-up.

## **1.6 Research Objective**

### 1.6.1 Flexible dye-sensitized solar cells (DSSCs)

Standard preparation of  $\text{TiO}_2$  photoelectrode on rigid glass substrate involves a high-temperature sintering process that is unsuitable for fabricating flexible DSSCs with polymeric flexible substrate. This means that alternative methods for the deposition and post-treatment of the  $\text{TiO}_2$  layer should be developed. The main purpose of high-temperature sintering process is to remove organic binder in the  $\text{TiO}_2$  paste and connect the individual  $\text{TiO}_2$  nanoparticles due to electric properties of  $\text{TiO}_2$  layer is affected by particle connectivity of  $\text{TiO}_2$  photoelectrode.[38]

Conductive flexible substrates, typically ITO-PET or ITO-PEN, are the most widely used alternatives for rigid glass substrates. While the obvious advantages for these flexible substrates are low-cost, light weight, and

processability for roll-to-roll type, the limitation of process temperature calls for alternative fabrication method. As the maximum process temperature for these polymeric substrates is around 150°C, the high-temperature sintering should be excluded. This precludes using organic-binder embedded TiO<sub>2</sub> paste during TiO<sub>2</sub> layer deposition, as they would remain in the TiO<sub>2</sub> layer under low-temperature condition. Absence of organic binders in the TiO<sub>2</sub> paste results in the formation of cracks in the film, thus reduce inter-particle necking and charge transport properties of TiO<sub>2</sub> layer. Decreased adhesion between TiO<sub>2</sub> layer and polymeric substrate are other challenges when polymeric flexible substrates are used due to the limitation of process temperature. Moreover, poor long-term stability of the flexible DSSCs due to desorption of adsorbed dye and penetration of moisture through the highly permeable polymer substrates is critical problem for real application. Thus, an additional post-treatment that has positive effect on the performance and long-term stability of device would be essential.[39]

In this study, first, we developed an electrospray method that can remove the use of organic binders or surfactants during the TiO<sub>2</sub> deposition process in order to overcome some limitations in low-temperature fabrication of flexible DSSCs. Especially, the 0-D hierarchically structured

TiO<sub>2</sub>s (HS-TiO<sub>2</sub>s) electrosprayed were formed due to ultrafast evaporation of volatile solvent. In the HS-TiO<sub>2</sub> structure, the electron transport was improved compared to non-HS ones. The HS-TiO<sub>2</sub>s were coated onto a flexible substrate using a binder-free dispersion of commercially available TiO<sub>2</sub> nanocrystalline powders (P25, Degussa). The formed HS-TiO<sub>2</sub>s showed highly crystalline phase. This nanocrystalline powder was, therefore, suitable for use in room-temperature fabrication method. This method is simple and cost-effective. All processes were performed under room-temperature conditions using large-area plastic substrates. Also, additional two post-treatment methods were tested in an effort to improve the interparticle connectivity under low-temperature condition. We characterized the effects of physical compression and TTB-treatment, introduced in an effort to improve the interparticle connectivity.

Second, we investigate the properties of room-temperature fabricated TiO<sub>2</sub> (R-TiO<sub>2</sub>) photoelectrode by considering the effects of different surface functionality on the photovoltaic performances and long-term stability. Also, we demonstrate a modification of dye anchoring on R-TiO<sub>2</sub> photoelectrode using stearic acid (SA) as co-adsorbent. The SA-treated R-TiO<sub>2</sub> (RS-TiO<sub>2</sub>) photoelectrode showed a dramatic enhancement in the long-term stability, 70.1% of its initial efficiency after 1000 h at 60°C under illumination of 100

$\text{mW cm}^{-2}$ . The SA-assisted binding mode of N719 dye on different  $\text{TiO}_2$  surface was proposed using UV-vis and ATR FT-IR spectroscopic studies.

Finally, we demonstrated a highly efficient approach for flexible DSSCs by co-sensitization of metal-free organic sensitizer (JH-1) and unsymmetrical squaraine dye (SQ2). The complementary spectral response of JH-1 and SQ2 dyes was obtained because of different absorption properties (400 nm ~ 550 nm for JH-1 and 550 nm ~ 700 nm for SQ2) of the individual sensitizers. The co-sensitization of  $\text{TiO}_2$  with high molar extinction sensitizers will be more effective for flexible DSSCs because of short diffusion length of room-temperature fabricated  $\text{TiO}_2$  layer.

### 1.6.2 Flexible piezoelectric nanogenerator (NG)

Since piezoelectric materials can convert mechanical energy into electrical energy with simple bulk-type structure, piezoelectric nanogenerator is highlighted as energy sources for self-powered system. The harvesting of mechanical energy by piezoelectric materials in particular has received enormous attention owing to the ability of these materials to convert mechanical energy into electricity directly and the feasibility of this approach for integrated applications. Traditionally, inorganic piezoelectric

ceramics, including BaTiO<sub>3</sub>, ZnO and PZT, have been used most for mechanical energy harvesting devices. Nevertheless, the extremely brittle property of inorganic piezoelectric ceramics and the incorporation of lead create issues such as flexibility, reliability, mechanical durability, and safety problem for long-term sustainable operation and hinder its real application.[40]

Recently, a variety of nanoparticle based piezoelectric materials, such as NaNbO<sub>3</sub>, KNbO<sub>3</sub>, ZnSnO<sub>3</sub> or PZT nanowire has been tested in flexible nanogenerator by dispersing piezoelectric particles in an elastic polydimethylsiloxane (PDMS) matrix. Although piezoelectric nanoparticles are more flexible than the bulk or thin film-based piezoelectric devices, the nanoparticle tend to be poorly dispersed in viscous PDMS and do not readily form percolating networks within the PDMS matrix. Power generation measurements collected from nanoparticle-based nanogenerators have revealed that these devices are strain-mode dependent. Electricity tends to be generated only under large compressive forces. The compressive forces can induce unavoidable electrostatic noise associated with the triboelectric effect due to the interfacial contact between the nanogenerator and the measurement equipment. Moreover, the PDMS matrix and the polymeric substrate, typically polyethylene terephthalate (PET) or

polyethylene naphthalate (PEN), are easily charged and induce electrostatic noises (triboelectric effects) that obscure a quantitative analysis of the piezoelectric output.

In this study, we characterized flexible piezoelectric nanogenerators using electrospun PZT nanofibers composited with PDMS. In particular, the flexible devices were loaded onto a measurement unit and were deformed by bending to minimize the triboelectric effects resulting from mechanical friction. We characterized the effects of the device thickness, PZT textile stacking arrangement, device area, and fiber orientations on the piezoelectric output generation. The relationship between the piezoelectric output and the applied strain was measured using PZT textiles having different orientations. Finally, we measured the piezoelectric outputs generated under different strain rates.

## **1.7 References**

- [1] Special Issue on Sustainability and Energy, *Science* **2007**, 315, 721
- [2] N. S. Lewis, *Science* **2007**, 315, 798
- [3] W. E. Glassley, *Geothermal Energy: Renewable Energy and the Environment*, CRC, Boca Raton, **2010**.

- [4] M. E. Himmel, *Science* **2007**, 316, 982
- [5] A. J. Bard, M. A. Fox, *Acc. Chem. Res.* **1995**, 28, 141
- [6] N. S. Lewis, D. G. Nocera, *Proc. Natl. Acad. Sci. USA* **2007**, 104, 20142
- [7] <http://www.ecnmag.com/News/2011/11/Global-PV-Installations-to-Hit-24-GW-in-2011-Predicts-IMS-Research/>
- [8] K. Palmer, D. Burtraw, *Energ. Econ.* **2005**, 27, 873
- [9] T. Eswam, P. T. Krein, B. T. Kuhn, R. S. Balog, P. L. Chapman, 2008 *IEEE Energy 2030 Conference* **2008**, pp. 594
- [10] S. Wojtczuk, X. Zhang, C. Harris, D. Pulver, M. Timmons in *Photovoltaic Specialists Conference (PVSC), 37th IEEE* **2011**.
- [11] S. Roundy, E. S. Leland, J. Baker, E. Carleton, E. Reilly, E. Lai, B. Otis, J. M. Rabaey, P. K. Wright, V. Sundararajan, *IEEE Pervas. Comput.* **2005**, 4, 28
- [12] C. Ó. Mathúna, T. O'Donnell, R. V. Martinez-Catala, J. Rohan, B. O'Flynn, *Talanta* **2008**, 75, 613
- [13] E. Bouendeu, A. Greiner, P. J. Smith, J. G. Korvink, *IEEE Sens. J.* **2011**, 11, 107
- [14] H. Chen, C. Jia, C. Zhang, Z. Wang, C. Liu in *2007 IEEE International Symposium on Circuits and Systems, Vols. 1–11*, **2007**, pp. 557–560
- [15] T. Soga, Nanostructured Materials for Solar Energy Conversion, p.194-

196

- [16] B. O'Regan, M. Grätzel, *Nature* **1991**, 353, 737
- [17] N. Vlachopoulos, P. Liska, J. Augustynski, M. Grätzel, *J. Am. Chem. Soc.* **1988**, 110, 1216
- [18] M. Grätzel, *J. Photochem. Photobiol. A Chem.* **2004**, 164, 3
- [19] C. J. Brabec, V. Dyakonov, J. Parisi, N. S. Sariciftci, *Organic Photovoltaics* p. 275-277
- [20] M. K. Nazeeruddin, A. Kay, I. Rodicio, R. Humphry-Baker, E. Mueller, P. Liska, N. Vlachopoulos, M. Grätzel, *J. Am. Chem. Soc.* **1993**, 115(4), 6382
- [21] M. K. Nazeeruddin, P. Pechy, T. Renouard, S. M. Zakeeruddin, R. Humphry-Baker, P. Comte, P. Liska, L. Cevey, E. Costa, V. Shklover, L. Spiccia, G. B. Beacon, C.A. Bignozzi, M. Grätzel, *J. Am. Chem. Soc.* 2001, **123**, 1613
- [22] P. Wange, S. M. Zakeeruddin, J. E. Moser, R. Humphry-Baker, P. Comte, V. Aranyos, A. Hagfeldt, M. K. Nazeeruddin, M. Grätzel, *Adv. Mater.* **2004**, 16, 1806
- [23] M. K. Nazeeruddin, P. Pechy, M. Grätzel, *Chem. Comm.* **1997**, 18, 1705
- [24] S. A. Haque, E. Palomares, H. M. Upadhyaya, L. Otley, R. J. Potter, A.

- B. Holmes, J. R. Durrant, *Chem. Commun.* **2003**, 3008
- [25] D. Li, Y. Xia, *Adv. Mater.* **2004**, 16, 1151
- [26] A. Jaworek, *J. Mater. Sci* **2007**, 42, 266
- [27] F. Schulz, S. Franzka, G. Schmid, *Adv. Funct. Mater.* **2001**, 12, 532
- [28] A. Jaworek, *Powder Technology* **2007**, 176, 18
- [29] D. Li, Y. Xia, *Adv. Mater.* **2004**, 16, 1151
- [30] W.E. Teo, T.C. Lim, Z. Ma, *An introduction to electrospinning and nanofibers*, **2005**, 15-17
- [31] X. Wang, *Nano Energy* **2012**, 1, 13
- [32] P. D. Mitcheson, E. M. Yeatman, G. K. Rao, A. S. Holmes, T. C. Green, *Proc. IEEE* **2008**, 96, 1457
- [33] P. D. Mitcheson, P. Miao, B. H. Stark, E. M. Yeatman, A. S. Holmes, T. C. Green, *Sens. Actuators A* **2004**, 115, 523
- [34] Cady, W.G. 1946, "Piezoelectricity", *New York: McGraw-Hill*, pp. 699.
- [35] Ballato, A., "Piezoelectricity: history and new thrusts", *IEEE Proceeding of Ultrasonic Symposium*, **1996**, vol. 13, 575-583
- [36] Curie, J. and Curie, P. "Development par compression de l'electricite polaire dans les cristaux hemiedres a faces inclinees", *Compt. Rend*, **1880**, vol. 91, pp. 383
- [37] Minazara, E., Vasic, D., Costa, F. "Piezoelectric Generator Harvesting

Bike Vibrations Energy to Supply Portable Devices" *Applied Mathematics and Mechanics*, **2008**

[38] D. Hwang, H. Lee, S. Y. Jang, S. M. Jo, D. Kim, Y. Seo, D. Y. Kim, *ACS Appl. Mater. Interfaces*, **2011**, 3 (7), 2719

[39] H. Lee, D. Hwang, S. M. Jo, D. Kim, Y. Seo, D. Y. Kim, *ACS Appl. Mater. Interfaces*, **2012**, 4 (6), 3308

[40] Z. L. Wang, W. Wu, *Angew. Chem. Int. Ed.* **2012**, 51, 11700

## **Chapter 2**

### **Low-temperature fabrication of TiO<sub>2</sub> electrodes for flexible dye-sensitized solar cells using an electro-spray process**

#### **2.1 Introduction**

Dye-sensitized solar cells (DSSCs) are one of the most attractive electrochemical devices capable of converting light energy into electrical energy because they may be fabricated at low cost in an eco-friendly manner.[1] Recently, a conversion efficiency exceeding 11% under A.M 1.5G, 1 sun illumination ( $100 \text{ mW cm}^{-2}$ )[2-4] was achieved using Ru complex sensitizers. Plastic substrate-based flexible DSSCs have been the focus of several investigations over the past few years. Flexible DSSCs have unique advantages in their flexibility, lightweight, roll-to-roll processability, and wide applicability. Nanocrystalline TiO<sub>2</sub> electrodes for conventional DSSCs are usually prepared by screen-printing a TiO<sub>2</sub> paste containing

organic binders onto an FTO glass substrate, followed by high-temperature sintering. In general, an organic binder is used to adjust the viscosity and facilitate the preparation of a TiO<sub>2</sub> layer of appropriate thickness. High-temperature sintering processes (>450 °C) can remove organic residues as well as sinter TiO<sub>2</sub> nanoparticles. The main challenge associated with the fabrication of flexible DSSCs is identifying techniques that reduce the processing temperatures because polymeric electrode substrates, such as ITO-sputtered PEN (polyethylene naphthalate) or PET (polyethylene terephthalate), undergo structural or chemical changes at higher temperatures. ITO/PEN and ITO/PET display a high transparency, are lightweight, provide a low sheet resistance, and are mechanically stable; however, their thermal stabilities are low. The development of processing techniques for fabricating photoelectrodes using polymeric flexible substrates at temperatures below 150 °C would be desirable.[5]

Several alternative approaches to the preparation of nanocrystalline TiO<sub>2</sub> without thermal sintering have been developed, including the transfer of TiO<sub>2</sub> layers,[6] doctor blading of titania paste,[7-13] electrophoretic deposition,[14-16] and spray-deposition.[17-19] Mechanical compression,[7, 8] chemical sintering,[11, 12, 20] and microwave sintering[21] methods have been developed to introduce good connections among the as-prepared

TiO<sub>2</sub> electrodes; however, many of these approaches are inefficient when applied to large-area fabrication techniques, and cell performances can be poor. The most critical factor underlying the low efficiency is poor interparticle connectivity among the TiO<sub>2</sub> particles due to absence of a thermal sintering process.

Several groups have reported zero-dimensional hierarchical structured metal oxides for the production of highly efficient glass-based DSSCs. Zero-dimensional (0D) hierarchical structured metal oxides are advantageous in that they provide (1) large surface areas, (2) meso- or microporous structures, (3) light scattering effects, and (4) rapid electron transport;[22-25] however, the majority of these reports have examined only glass-based conventional DSSCs fabricated through thermal sintering processes. To the best of our knowledge, few studies have reported the use of hierarchical structured TiO<sub>2</sub> (HS-TiO<sub>2</sub>) for the fabrication of flexible DSSCs at room temperature.[16, 18] Cha et al. described the preparation of presintered TiO<sub>2</sub> microballs for sinter-free processing using air-spray deposition onto flexible substrates;[18] however, the performances of DSSCs assembled using this method were poor. In addition to the poor performance, these processes were not binder-free. Organic surfactants, such as hydroxybenzoic acid, were added to the TiO<sub>2</sub> suspension to yield

spherical microball aggregates. Chen et al. reported the room-temperature electrophoretic deposition of mesoporous TiO<sub>2</sub> nanoparticles to produce secondary aggregates consisting of primary anatase nanoparticles for the fabrication of flexible DSSCs.[16] Although these DSSCs performed well, the method was not practical for obtaining large-area photoelectrodes.

To overcome some limitations in low temperature fabrication of flexible DSSCs, we adopt an electrospray method that can remove the use of binders or surfactants during the process. The electrostatic spray technique has recently been considered as a cheap and simple process to directly deposit thin films from their colloidal solutions. The techniques can be applied widely in modern material technologies, microelectronics, nanotechnology.[26] During the electrospray deposition known as induction or conduction charging, the droplets can be charged of their atomization by mechanical forces in the presence of electric field between the solution and the depositing substrates.[27] The deposition efficiency of the charged droplets is usually much higher than that of the uncharged droplets, which can improve the adhesion between the materials and substrates.

We recently developed this method for the fabrication of 0D hierarchically structured TiO<sub>2</sub> (HS-TiO<sub>2</sub>s) for the production of highly efficient DSSCs on FTO glass substrates. In the HS-TiO<sub>2</sub> structure, the

electron transport was improved compared to non-HS ones.[25] The HS-TiO<sub>2</sub>s were coated onto a flexible substrate using a binder-free dispersion of commercially available TiO<sub>2</sub> nanocrystalline powders (P25, Degussa). The formed HS-TiO<sub>2</sub>s showed highly crystalline phase because the TiO<sub>2</sub> purity of P25 nanocrystalline powder is more than 99.5%, which consist of 70% anatase and 30% rutile. This nanocrystalline powder was, therefore, suitable for use in room-temperature fabrication methods. This method is simple and cost-effective. All processes were performed under room-temperature conditions using large-area plastic substrates. DSSCs prepared using the 0D HS-TiO<sub>2</sub> electrodes fabricated by electrospray displayed a high efficiency as a result of the hierarchical morphological structure of the electrode coating.

Two post-treatment techniques were tested in an effort to improve the interparticle connectivity: mechanical compression and chemical sintering using titanium n-tetrabutoxide (TTB). We characterized the effects of physical compression and optimized the conditions for fabricating highly efficient flexible DSSCs at low temperatures. Finally, we examined the performance of electrodes fabricated using TTB treatment, introduced in an effort to improve the interparticle connectivity.

## 2.2 Experimental

### 2.2.1 Materials

Indium–tin-oxide (ITO)-coated polyethylene naphthalate (PEN) (Pecell, sheet resistance 13  $\Omega$ /sq, 200  $\mu$ m) was used as a transparent conducting substrate. A Pt/Ti-sputtered PEN film (Pecell, sheet resistance 5  $\Omega$ /sq) was used as a counter electrode in the flexible DSSCs. The nanocrystalline P25 powder was purchased from Degussa to prepare a TiO<sub>2</sub> dispersion for electrospray processing. A ruthenium complex sensitizer (Ru535-bisTBA, Solaronix SA), cis-diisothiocyanato-bis(2,2'-bipyridyl-4,4'-dicarboxylato) ruthenium(II) bis(tetrabutylammonium), generally known as N719, was purified using ion exchange column chromatography. Iodine (I<sub>2</sub>, 99.99+%, Aldrich), 4-*tert*-butylpyridine (TBP, 99%, Aldrich), lithium iodide (LiI, 99.9%, Aldrich), 1-butyl-3-methylimidazolium iodide (BMII, 99%, C-tri), acetonitrile (ACN, 99.8%, Aldrich), valeronitrile (VN, 99.5%, Aldrich), and titanium n-tetrabutoxide (TTB, 97%, Aldrich) were used as purchased without further purification.

### **2.2.2 Preparation of the HS-TiO<sub>2</sub> Electrodes**

The HS-TiO<sub>2</sub> was prepared according to the reported procedure.[25] The 10% (wt/v) P25 was dispersed in anhydrous ethanol using an ultra apex mill (Model UAM-015, Kotobuki). The stabilized P25 dispersion was loaded into a plastic syringe infusion pump (KD Scientific Model 220) connected to a high-voltage power supply (BERTAN SERIES 205B). The solution was then electrospayed directly onto the conducting ITO-PEN film (Pecell, 13 Ω/sq, 10 cm × 10 cm). An electric field of 1.5 kV cm<sup>-1</sup> was applied between the metal orifice and the conducting substrate with a feed rate of 40 μL min<sup>-1</sup>. A motion control system governed by a microprocessor (Dasa Tech) was used to control the nozzle and substrate during deposition to produce a uniformly thick film over a large area.

### **2.2.3 TTB treatment**

Post-treatment with titanium n-tetrabutoxide (TTB) was implemented by soaking the as-pressed HS-TiO<sub>2</sub> photoelectrodes in a 0.2 M TTB/n-butanol solution for 1 h, then the photoelectrode was rinsed several times using same solution. The TTB-treated HS-TiO<sub>2</sub> photoelectrode was dried at room

temperature for 1 h, immersed in deionized water at 100°C for 4 h, then dried in a vacuum oven at 80°C for 4 h. After cooling to room temperature, the TTB-treated HS-TiO<sub>2</sub> electrodes were immersed in a 0.3 mM N719 solution for 24 h at room temperature.

### **2.2.3 Device Fabrication**

After electrospray processing, the as-sprayed HS-TiO<sub>2</sub> flexible photoelectrode was pressed for 10 min at 80°C. Typical applied pressures were 10 MPa. The pressed photoelectrode was then immersed in a purified 0.3 mM N719 tert-butanol/acetonitrile (50/50 v/v) solution for 24 h at room temperature. The counter electrode was prepared by washing a Pt/Ti-sputtered PEN film with anhydrous ethanol, followed by cleaning in an ultrasonic bath containing IPA for 20 min. The dye-adsorbed HS-TiO<sub>2</sub> electrodes were rinsed with anhydrous ethanol and dried under a nitrogen flow. The dye-adsorbed TiO<sub>2</sub> electrodes were assembled and sealed along with the counter electrode using a thermal adhesive film (Surlyn, Dupont 1702, 60 μm thick) as a spacer to fabricate sandwich-type cells. The typical active area of a cell was 0.25 cm<sup>2</sup>. The liquid electrolyte consisted of 0.65 M 1-butyl-3-methylimidazolium (BMII), 0.03 M iodine (I<sub>2</sub>), 0.1 M lithium

iodide (LiI), and 0.5 M 4-tert-butylpyridine (TBP) in a mixture of acetonitrile (ACN) and valeronitrile (VN) (85/15 v/v). An electrolyte solution was injected through a predrilled hole in the counter electrode.

#### **2.2.4 Characterization of the Flexible DSSCs**

The morphology of the HS-TiO<sub>2</sub> coating was investigated using a field-emission scanning electron microscopy (FE-SEM, Hitachi S-4100) with an accelerating voltage of 15 kV. The surface area and pore distribution properties were measured using a Sorptomatic 1990, the surface area was determined by the Brunauer–Emmett–Teller (BET) method, and the pore volume and size distributions were determined by the Barrett–Joyner–Halenda (BJH) method using the adsorption branches of the isotherms. The quantity of dye adsorbed onto the HS-TiO<sub>2</sub> surfaces was determined by desorbing the dye a 0.1 M NaOH aqueous solution, and the absorption spectra of the desorbed dye solution were measuring using a UV–vis spectrophotometer (Agilent 8453). Photovoltaic measurements of the DSSCs were conducted using an AM 1.5 solar simulator and a 450 W Xe lamp. The intensity of the simulated light was calibrated using a Si reference solar cell to yield AM 1.5 global irradiation. The photovoltaic characteristics

of the DSSC were obtained by applying an external potential bias to the cells and by measuring the photocurrent generated using a Keithley model 2400 source meter. The IPCE was measured as a function of the wavelength from 350 to 800 nm using an IPCE system designed especially for DSSCs (PV measurement, Inc.). A 75 W xenon lamp was used as the light source to generate a monochromatic beam. A NIST calibrated silicon photodiode was used as the standard during calibration. IPCE values were collected at a low chopping speed of 10 Hz. The electron transport time and electron recombination lifetime were measured by intensity-modulated photocurrent spectroscopy (IMPS) and intensity-modulated photovoltage spectroscopy (IMVS). A diode laser with variable power and modulation control (Coherent Lab-laser, 40 mW, 446 nm) was used as the light source. Illumination was always incident on the working electrode side of the solar cell. The light intensity was measured using a calibrated Si photodiode. IMVS was performed under open-circuit conditions. The output of the solar cell was connected directly to a frequency response analyzer (Schlumberger–Solartron SI 1260). IMPS measurements were performed by connecting the solar cell via a potentiostat amplifier (EG&G PAR 273) to the frequency response analyzer. During the IMPS and IMVS measurements, the cell was illuminated with sinusoidal modulated light having a small AC

component (10% or less of the DC component).

## **2.3 Results and discussion**

### **2.3.1 Morphological Changes in the HS-TiO<sub>2</sub> after Mechanical Compression**

The electro spraying process generates microdroplets and simultaneously applies a charge by means of an electric field. SEM images of HS-TiO<sub>2</sub> photoelectrodes are shown in Figure 2.1. Hierarchically structured TiO<sub>2</sub> (HS-TiO<sub>2</sub>) spherical particles with an average diameter of 600 nm were prepared via a binder-free electro spray method (Figure 2.1a and 2.1b). The individual HS-TiO<sub>2</sub> spherical particles consisted of P25 primary particles and were uniformly stacked on a conductive ITO-PEN substrate. The as-sprayed HS-TiO<sub>2</sub> spheres packed tightly in the film because of the ultrafast evaporation of the solvent during the electro spray process. Although well-structured HS-TiO<sub>2</sub> spheres were fabricated using the electro spray method, physical adhesion among the individual HS-TiO<sub>2</sub> spheres and/or the substrate was weak. The as-sprayed HS-TiO<sub>2</sub> films could be damaged even by weak brushing. During the electro spray process, particle stacking proceeded under the forces of the electric field and gravity. No binder

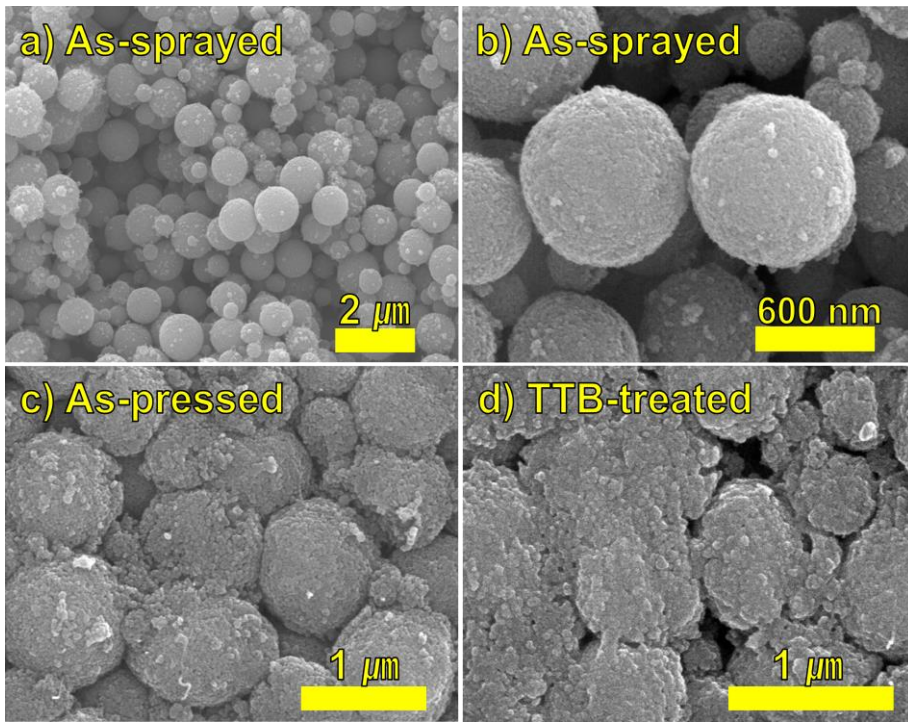


**Figure 2.1** SEM images of (a) and (b) as-sprayed, (c) as-pressed, and (d) TTB-treated HS-TiO<sub>2</sub> photoelectrode

materials were used during the electrospray process. Other approaches to improving the connectivity among HS-TiO<sub>2</sub> particles are needed. Some methods for improving interparticle connectivity have been reported, such as TiCl<sub>4</sub> treatment, but these methods are not suitable for low-temperature processing. Mechanical compression was introduced in an effort to improve particle adhesion and connectivity.

Compression of the as-sprayed HS-TiO<sub>2</sub> photoelectrode at pressures of 10 MPa increased the HS-TiO<sub>2</sub> sphere interface area of the as-pressed HS-TiO<sub>2</sub> photoelectrodes (Figure 2.1c) relative to the as-sprayed HS-TiO<sub>2</sub> photoelectrode spheres. The morphological change after compression treatment was characterized using BJH and BET measurements.

As shown in Table 1, the pore volume of the as-pressed HS-TiO<sub>2</sub> was reduced from 1.36 to 0.84 cm<sup>3</sup> g<sup>-1</sup> after compression treatment. The structures of the as-sprayed HS-TiO<sub>2</sub> were highly porous; however, many pores remained in the as-pressed HS-TiO<sub>2</sub> after compression treatment. The surface area of as-pressed HS-TiO<sub>2</sub> was reduced from 76.68 to 58.74 m<sup>2</sup> g<sup>-1</sup>, indicating that the interface area among the as-pressed HS-TiO<sub>2</sub> spheres increased upon compression treatment. The pore size distributions of the as-sprayed and as-pressed HS-TiO<sub>2</sub> films are shown in Figure 2.2. Bimodal distributions were observed for both HS-TiO<sub>2</sub> samples, reflecting two types

of particle interface in the electrospayed HS-TiO<sub>2</sub> films: the interface formed by the boundaries between primary P25 particles with micropores, and the interface formed by the boundaries between secondary HS-TiO<sub>2</sub> spheres with macro-pores. The total volume of macro-pores 100 nm in diameter was reduced, but the total volume of micropores 15 nm in diameter remained constant upon compression treatment. These results support that (1) the primary TiO<sub>2</sub> particles formed highly dense hierarchical structure due to the ultrafast evaporation of the solvent during the electro-spray process, (2) the as-sprayed HS-TiO<sub>2</sub> spheres weakly adhered to their neighboring ones, and (3) the contact area between each as-pressed HS-TiO<sub>2</sub> spheres was enlarged through mechanical compression treatment. Also, these morphological characteristics of electrospayed HS-TiO<sub>2</sub> imply that the internal electron transport within an HS-TiO<sub>2</sub> sphere proceed more rapidly than electron transport between adjacent HS-TiO<sub>2</sub> ones.

HS-TiO <sub>2</sub> type	Surface area ( m <sup>2</sup> g <sup>-1</sup> )	Pore volume ( cm <sup>3</sup> g <sup>-1</sup> )	Adsorbed dye ( mol mg <sup>-1</sup> )
As-sprayed	76.88	1.3621	4.55 × 10 <sup>-8</sup>
As-pressed	58.74	0.8391	4.41 × 10 <sup>-8</sup>

**Table 2.1** Physical characteristics of as-sprayed and as-pressed HS-TiO<sub>2</sub> particles

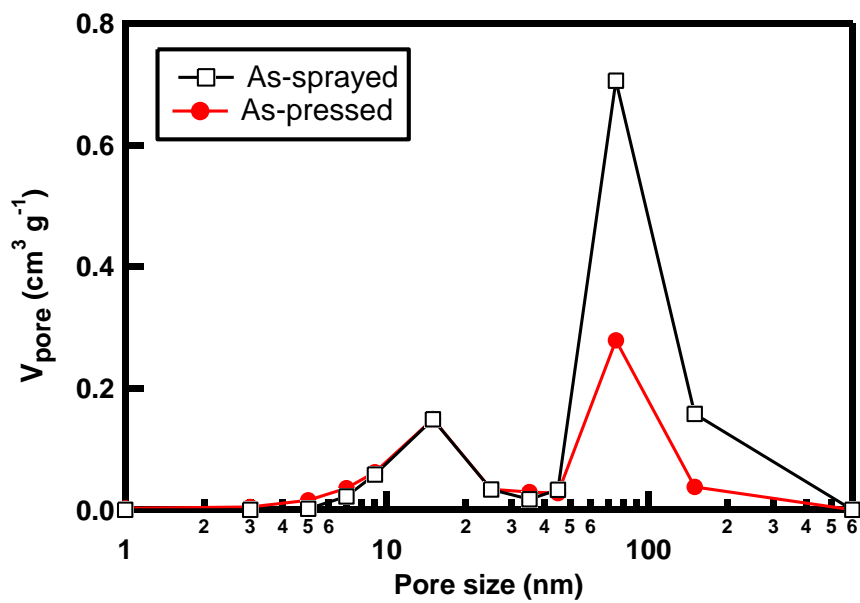


**Figure 2.2** Pore volume distribution of as-sprayed and as-pressed HS-TiO<sub>2</sub> particles

### **2.3.2 Photovoltaic Performance upon Compression Treatment**

Figure 2.3a shows the J–V characteristics of assembled flexible DSSCs. The open squares and closed circles in Figure 2.3a indicate the J–V curves associated with the as-sprayed and as-pressed HS-TiO<sub>2</sub> photoelectrodes, respectively. Table 2 summarizes the photovoltaic properties of each flexible DSSC. The conversion efficiency of the cell fabricated with the as-sprayed HS-TiO<sub>2</sub> film was 2.09%. The poor cell performance, particularly at a low photocurrent density, arose from the weak physical adhesion among the as-sprayed HS-TiO<sub>2</sub> spheres. The low fill factor of the as-sprayed HS-TiO<sub>2</sub> provided further evidence for the poor adhesion of the HS-TiO<sub>2</sub> film to the ITO-PEN substrate; however, after compression treatment, the power conversion efficiency of the as-pressed HS-TiO<sub>2</sub> cell increased to 5.02%. The photocurrent density increased by more than a factor of 2. The difference between the photocurrents generated by the as-sprayed and as-pressed HS-TiO<sub>2</sub> electrodes was investigated by measuring the incident photon-to-current conversion efficiency (IPCE). The key parameter determining the photocurrent density is the IPCE. Figure 2.3b shows the IPCE spectra of the as-sprayed and as-pressed HS-TiO<sub>2</sub> photoelectrodes.

The quantum efficiency of the as-pressed HS-TiO<sub>2</sub> photoelectrode was higher than that of the as-sprayed HS-TiO<sub>2</sub> for all incident light wavelengths. Maximum IPCE values of 51 and 29% were achieved using the as-sprayed and as-pressed HS-TiO<sub>2</sub> photoelectrode, respectively. These results were consistent with the current density values listed in Table 2. The IPCE depends on the light harvesting efficiency ( $\eta_{\text{LH}}$ ), the electron injection efficiency ( $\eta_{\text{INJ}}$ ), and the electron collection efficiency ( $\eta_{\text{COL}}$ ). The light harvesting, electron injection, and electron collection efficiencies are related to the amount of dye adsorbed onto the TiO<sub>2</sub>, the fraction of photons absorbed by the dye that are converted into conduction band electrons, and the degree of TiO<sub>2</sub> interparticle connectivity.[5] As stated above, mechanical compression affected the morphological parameters of the HS-TiO<sub>2</sub> particles, including the surface area and porosity. These morphological changes can alter the amount of dye adsorbed onto the HS-TiO<sub>2</sub> or the charge transport properties in terms of the  $\eta_{\text{LH}}$  or  $\eta_{\text{COL}}$ . The amount of dye adsorbed in the as-sprayed HS-TiO<sub>2</sub> film was  $4.55 \times 10^{-8}$  mol mg<sup>-1</sup>, nearly identical to that adsorbed in the as-pressed HS-TiO<sub>2</sub> film ( $4.41 \times 10^{-8}$  mol mg<sup>-1</sup>), as shown in Table 1. The difference between the quantities of dye adsorbed onto the HS-TiO<sub>2</sub> could not explain the difference in the photocurrent generation in terms of  $\eta_{\text{LH}}$ . These results agreed with our previous report.[25] The other

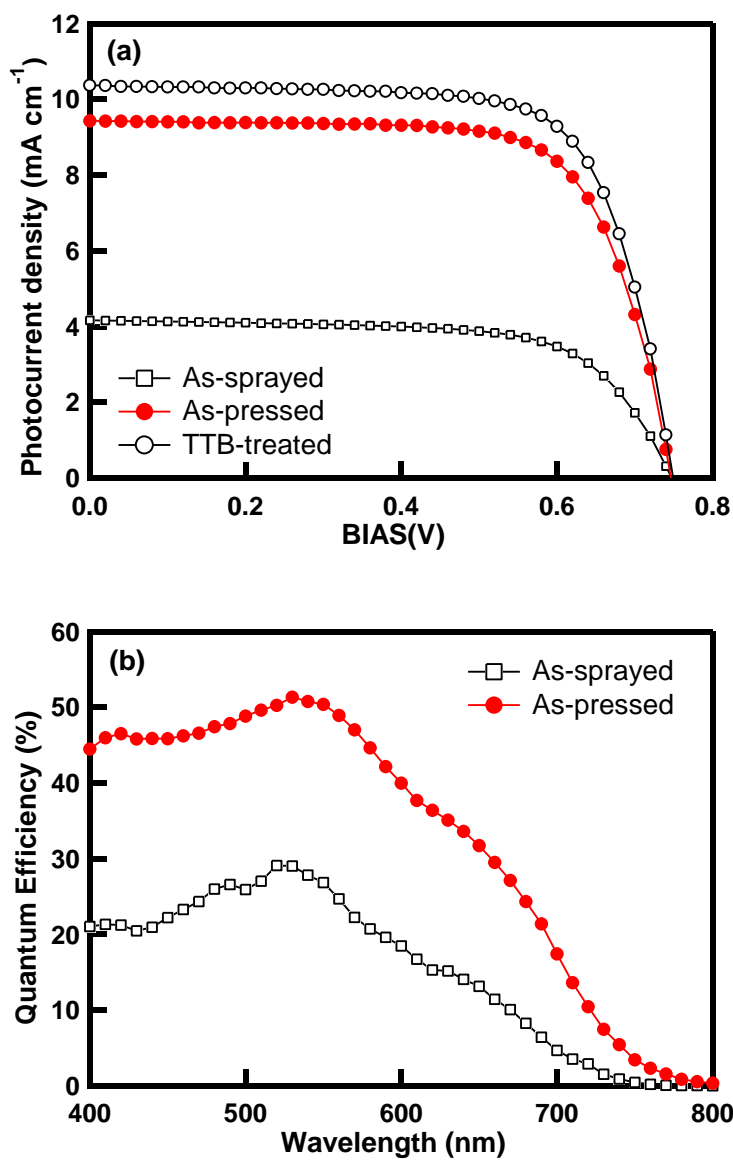


**Figure 2.3** J-V curves (a) and IPCE spectra (b) of the DSSCs based as-sprayed and as-pressed HS-TiO<sub>2</sub> photoelectrodes

HS-TiO <sub>2</sub> type	V <sub>oc</sub> ( V )	J <sub>sc</sub> ( mA cm <sup>-2</sup> )	FF	EFF ( % )
As-sprayed	0.748	4.16	67.2	2.09
As-pressed	0.747	9.43	71.3	5.02
TTB-treated	0.749	10.36	71.7	5.57

**Table 2.2** Photovoltaic properties of the DSSCs using as-sprayed, as-pressed and TTB-treated HS-TiO<sub>2</sub> photoelectrode with a film thickness of 9μm

key parameter,  $\eta_{\text{COL}}$ , is associated with the electron diffusion coefficient and the electron recombination lifetime. As mentioned, we introduced a mechanical compression treatment to increase the interparticle connectivity and the photocurrent density levels from the low values associated with the as-sprayed HS-TiO<sub>2</sub>. The mechanism underlying the photocurrent increase as a result of compression was investigated by measuring the charge transport properties of the as-sprayed and as-pressed HS-TiO<sub>2</sub> electrodes through intensity-modulated photocurrent spectroscopy (IMPS) and intensity-modulated photovoltage spectroscopy (IMVS) measurements. Figure 2.4 shows typical IMPS and IMVS plots of the assembled flexible DSSCs. The diffusion coefficient was calculated from the IMPS curve according to eq 1,

$$D = \frac{d^2}{2.5\tau_d}$$

where  $D$ ,  $d$ , and  $\tau_d$  are the diffusion coefficient, thickness of the TiO<sub>2</sub> layer, and electron transport time, respectively. The electron transport time could be estimated from the relation 2,

$$\tau_d = \frac{1}{2\pi f_{\min, \text{IMPS}}}$$

where  $f_{\min}$  is the characteristic frequency at the minimum of the imaginary component of the IMPS curve (Figure 2.4a). The electron recombination lifetimes in the DSSCs were determined using eq 3,

$$\tau_r = \frac{1}{2\pi f_{\min, \text{IMVS}}}$$

where  $f_{\min}$  is the characteristic frequency at the minimum of the imaginary component of IMVS (Figure 2.4b). The calculated results are shown in Figure 2.5. The diffusion coefficients of the as-pressed HS-TiO<sub>2</sub> were 1 order of magnitude higher than those of the as-sprayed HS-TiO<sub>2</sub> within the measured photon flux range. This IMPS result indicated that mechanical compression treatment enlarged the contact area among HS-TiO<sub>2</sub> spheres, and the electron diffusion properties of the HS-TiO<sub>2</sub> electrode improved with the mechanical compression treatment, leading to a higher photocurrent density. Figure 2.5b shows the recombination lifetimes of the assembled flexible DSSCs. Although the  $\tau_r$  values of the as-pressed HS-TiO<sub>2</sub> films were slightly longer than those of the as-sprayed HS-TiO<sub>2</sub> films over the

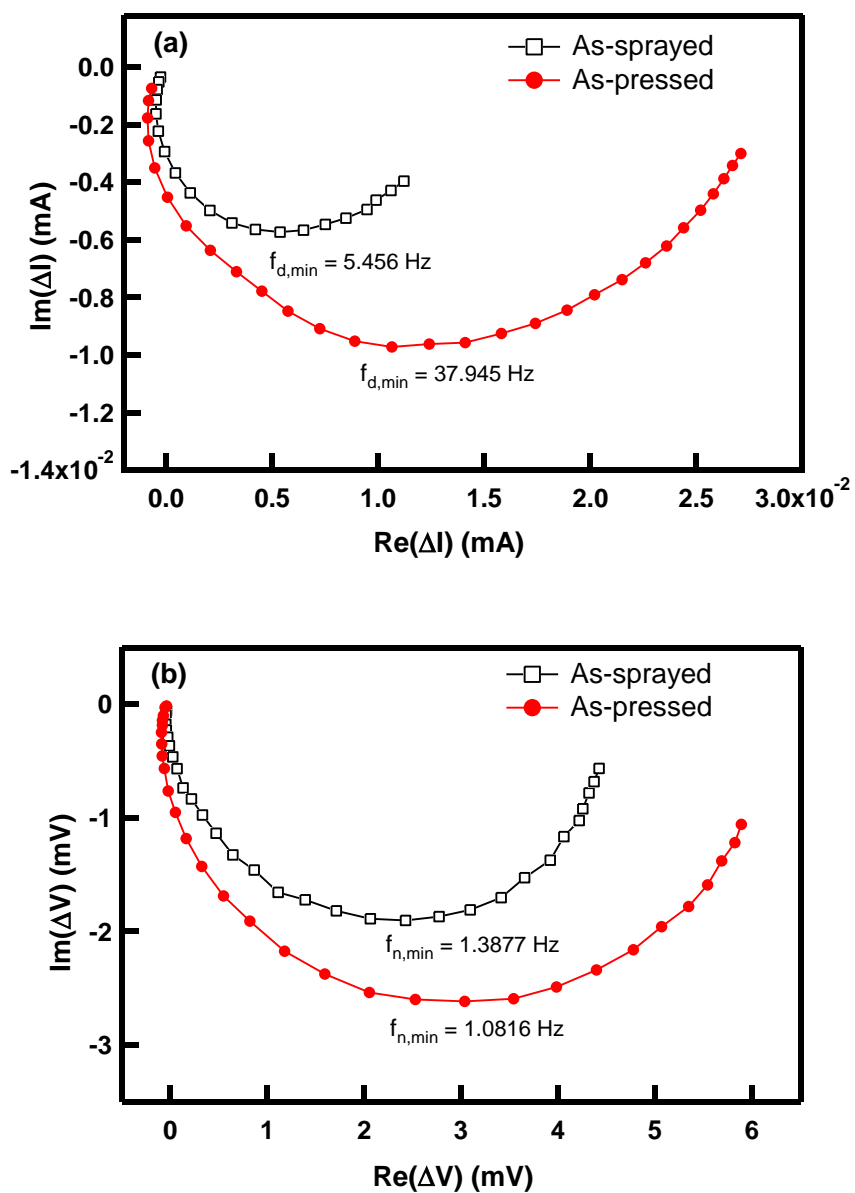


**Figure 2.4** Typical IMPS (a) and IMVS (b) plots of the DSSCs based as-sprayed and as-pressed HS-TiO<sub>2</sub> photoelectrodes

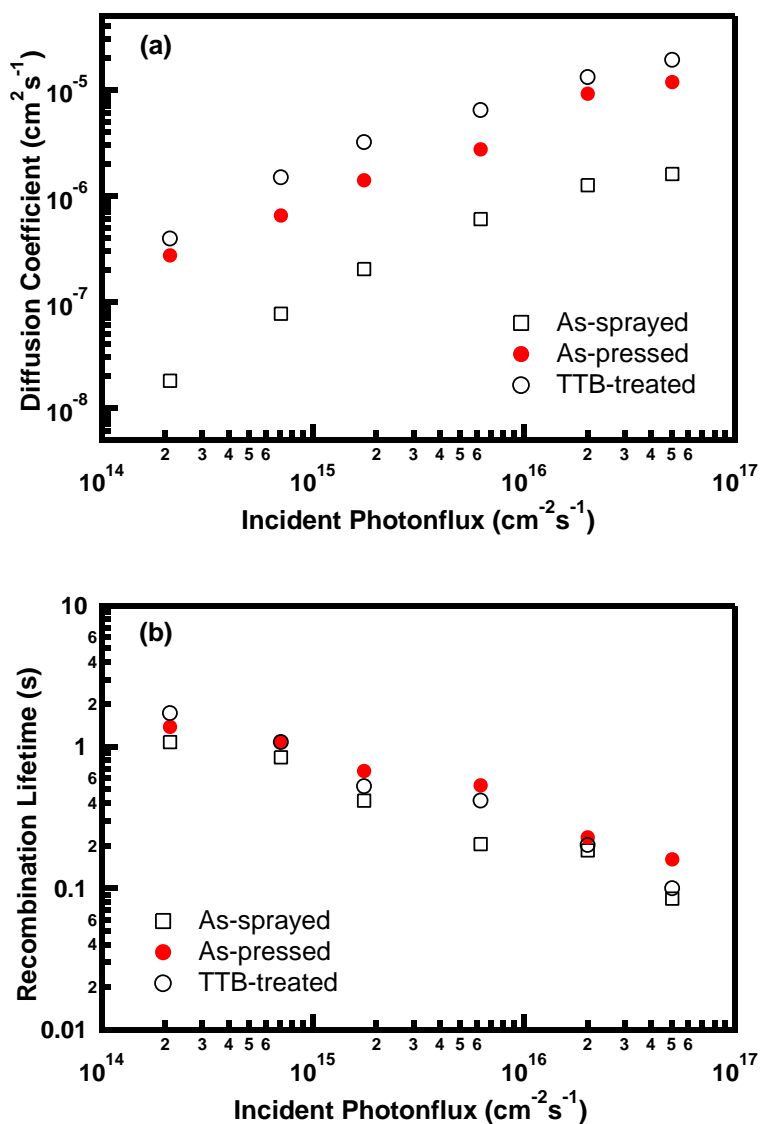


**Figure 2.5** Electron diffusion coefficient (a) and recombination lifetime (b) of the DSSCs based as-sprayed, as-pressed, and TTB-treated HS-TiO<sub>2</sub> photoelectrodes as a function of the incident photonflux for 446 nm modulated (<10%) laser illumination

measured photon flux range, the difference in the recombination lifetime was insignificant and could not explain the higher photocurrent density after compression treatment. It was concluded that the higher photocurrent density did not arise from the longer recombination lifetimes, but rather from the faster electron transport (i.e., a larger electron diffusion coefficient). Morphologically, the average electron transport path length in the as-pressed HS-TiO<sub>2</sub> was shorter than that in the as-sprayed HS-TiO<sub>2</sub> film for an equal TiO<sub>2</sub> film weight because the as-pressed HS-TiO<sub>2</sub> particles were more dense (i.e., less porous) in structure. The structural features of the as-pressed HS-TiO<sub>2</sub> films facilitated rapid electron diffusion and generated a high photocurrent.

### **2.3.3 Thickness Dependence of the As-pressed HS-TiO<sub>2</sub>**

#### **Photo-electrodes.**

The optimum thickness of the as-pressed HS-TiO<sub>2</sub> photoelectrodes was determined by measuring the efficiency parameters of the cell as a function of the thickness, from 3 to 21 μm. Figure 2.6 and Table 2.3 show the photovoltaic performances of DSSCs prepared with photoelectrodes with as-pressed HS-TiO<sub>2</sub> films of various thicknesses. The photoelectrode

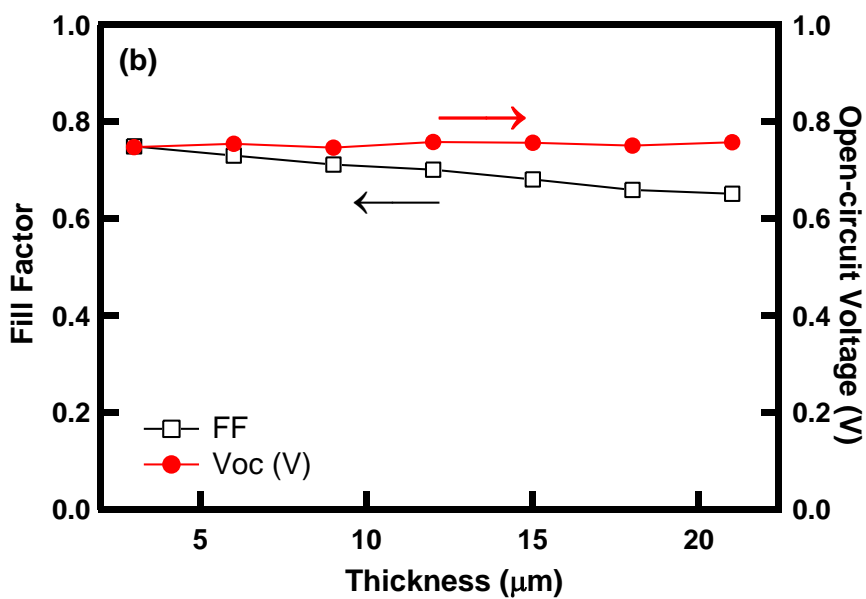
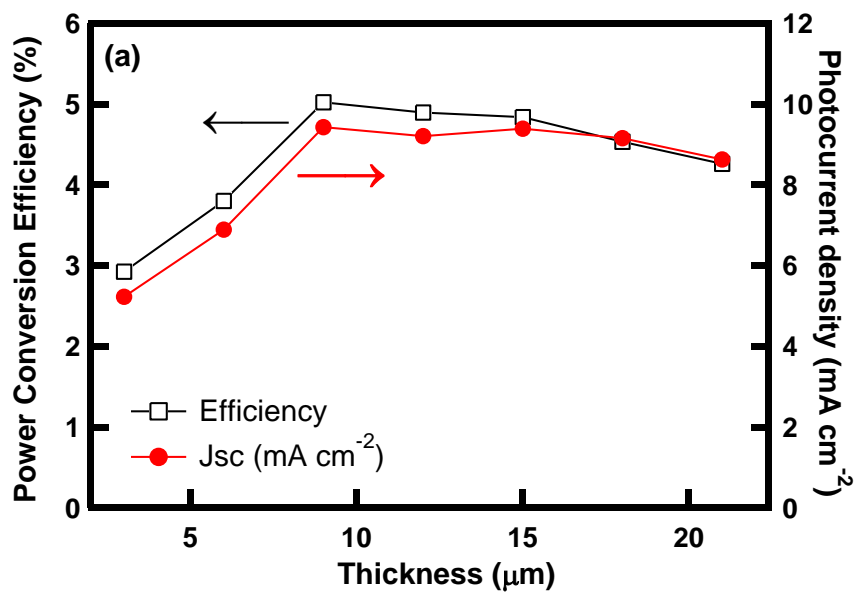


**Figure 2.6** Photovoltaic properties of DSSCs prepared with photoelectrodes with as-pressed HS-TiO<sub>2</sub> films of various thicknesses

Thickness ( $\mu\text{m}$ )	3	6	9	12	15	18	21
$V_{OC}$ (V)	0.748	0.755	0.747	0.759	0.757	0.751	0.758
$J_{SC}$ ( $\text{mA cm}^{-2}$ )	5.23	6.89	9.43	9.21	9.39	9.16	8.63
FF	74.3	73.1	71.3	70.1	68.1	66.0	65.1
EFF (%)	2.93	3.80	5.02	4.90	4.84	4.53	4.26

**Table 2.3** Summary of photovoltaic performance of DSSC prepared with photoelectrode with as-pressed HS-TiO<sub>2</sub> films of various thickness

thicknesses were easily controlled by adjusting the electrospray deposition time. All sample thickness values were measured after compression treatment using a surface profiler. In general, the total amount of adsorbed dye was proportional to the thickness of the photoelectrode; therefore, as the thickness of the as-pressed HS-TiO<sub>2</sub> increased, the photocurrent density and conversion efficiency increased. The conversion efficiency of the as-pressed HS-TiO<sub>2</sub> cell reached its highest value of 5.02% at 9 μm; however, beyond 9 μm, the photocurrent density and conversion efficiency decreased slightly. This trend was observed because the electron pathway from the top of the photoelectrode to the conducting substrate was too long to permit transport without recombination. The open circuit voltages of the as-pressed HS-TiO<sub>2</sub> photoelectrodes were constant over the range of measured thickness values, and the fill factors of the as-pressed HS-TiO<sub>2</sub> decreased continuously. The decrease in the fill factor as the thickness increased resulted from an increase in the resistance of the thick HS-TiO<sub>2</sub> electrode. The DSSC photovoltaic performances for the various photoelectrode thicknesses are summarized in Table 3.

The optimum thickness was quantitatively analyzed by calculating the electron diffusion length ( $L_n$ ) using the measured IMPS and IMVS results, according to eq 4

$$L = \sqrt{D_n \tau_r}$$

where  $D_n$  and  $\tau_r$  are the diffusion coefficient and recombination lifetime of electrons, respectively. The electron diffusion length represents the average distance that injected electron can travel through a photoelectrode prior to recombination. This relation implies that the electron diffusion length,  $L_n$ , should be longer than the thickness of the photoelectrode in order to effectively collect the photocurrent. The calculated average  $L_n$  of the as-pressed HS-TiO<sub>2</sub> film was 10.77  $\mu\text{m}$ , longer than the optimum thickness (9  $\mu\text{m}$ ) of the as-pressed HS-TiO<sub>2</sub> photoelectrode. For this reason, the optimum efficiency occurred at a thickness of 9  $\mu\text{m}$ , and the conversion efficiency of the as-pressed HS-TiO<sub>2</sub> cells decreased above a thickness of 12  $\mu\text{m}$ .

### **2.3.4 TTB-treatment after Compression Treatment**

As mentioned, the low efficiency of the as-sprayed HS-TiO<sub>2</sub> films was overcome and well-structured HS-TiO<sub>2</sub> photoelectrodes were prepared by introducing a physical post-treatment. The mechanical compression treatment improved the physical interparticle necks of the HS-TiO<sub>2</sub> spheres,

as well as the electron transport properties, which increased the photocurrent density of the cells. Although a higher efficiency was achieved using this physical treatment of the as-pressed HS-TiO<sub>2</sub> electrodes, further improvements were achieved by introducing chemical post-treatments using a titanium precursor.

Conventional FTO-based DSSCs include a preparation step involving a chemical post-treatment using, for example, TiCl<sub>4</sub>[25, 31, 32] or TTIP,[33] which improved the conversion efficiency of the as-prepared photoelectrodes. Our group reported conversion efficiency improvements using TiCl<sub>4</sub> treatment of the HS-TiO<sub>2</sub> films in conjunction with a thermal sintering process;[25] however, these chemical post-treatments were not suitable for plastic-based flexible DSSCs because a high-temperature thermal treatment process was necessary to crystallize the as-treated titanium precursor. Moreover, the ITO-PEN surface could be corroded under acidic conditions during the TiCl<sub>4</sub> treatment. Alternative low-temperature processing approaches must be tested for the fabrication of flexible DSSCs. In this research, titanium n-tetrabutoxide (TTB) treatment was introduced to improve the HS-TiO<sub>2</sub> interparticle physical necks. Recently, Fan et al. used TTB as a sintering medium under ambient atmospheric conditions to prepare flexible DSSCs;[28] however, this method was unfavorable for

electron transport applications because the product of TTB hydrolysis under such conditions is amorphous.[28, 29] Tan et al. reported that a hydrothermal reaction of TTB with water at 100 °C under atmospheric pressure induced formation of a crystalline anatase TiO<sub>2</sub>.[30] Therefore, we applied this method to fabricate crystalline TiO<sub>2</sub> because the hydrothermal conditions were suitable for flexible substrates. Hot water treatment of TTB was implemented by immersing air-dried TTB-treated photoelectrodes in 100°C water for 4 h to crystallize the amorphous TTB into an anatase phase. Prior to the post-treatment of TTB, XRD patterns of the air-dried TTB and hot water-treated TTB were investigated. The air-dried TTB was amorphous, but the hydrolyzed phase of the hot water-treated TTB was anatase, as shown in Figure 2.7. This indicated that the newly formed anatase phase from the hot water-treated TTB could assist electron transport among the HS-TiO<sub>2</sub> spheres, unlike the amorphous air-dried TTB.

Figure 2.1d shows an SEM image of the TTB-treated HS-TiO<sub>2</sub> electrode. Each as-pressed HS-TiO<sub>2</sub> sphere was well-connected by the hydrolyzed TTB. The anatase coating, newly introduced by hydrolysis of the TTB layer on the as-pressed HS-TiO<sub>2</sub> spheres, improved the interparticle connectivity, which improved electron transport through the as-pressed HS-TiO<sub>2</sub> photoelectrode. The J–V curves of the TTB-treated cell and as-pressed cell

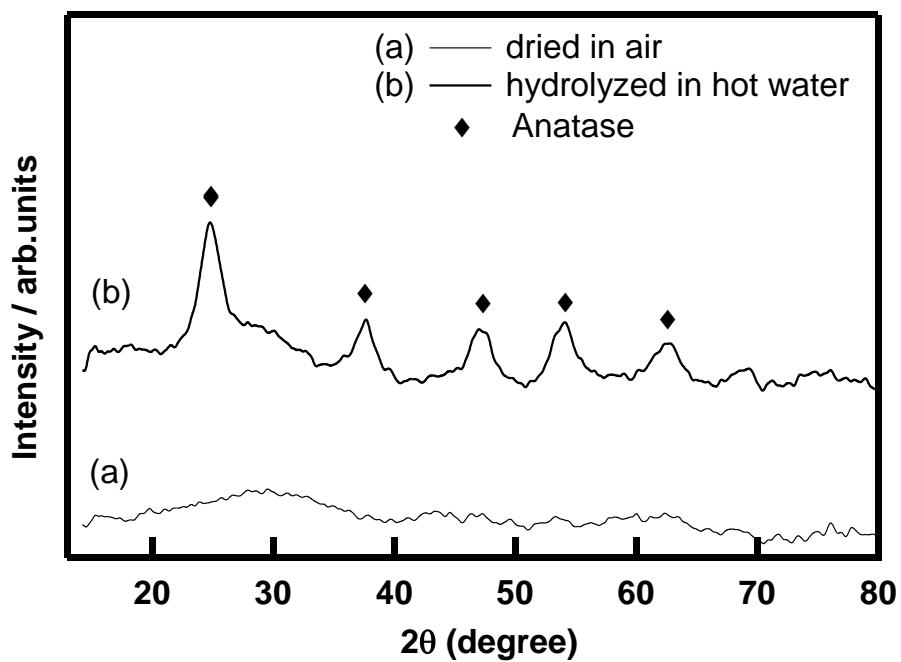


**Figure 2.7** XRD diffraction patterns of air-dried TTB (a) and hot water-treated TTB (b)

are illustrated in Figure 2.3a, and the photovoltaic parameters of these cells are summarized in Table 2. As mentioned above, the best efficiency achieved for the as-pressed HS-TiO<sub>2</sub> photoelectrodes was 5.02%. The V<sub>OC</sub> and FF of TTB-treated cells were comparable to the values of the as-pressed cell, whereas a higher conversion efficiency of  $\eta = 5.57\%$  was obtained in conjunction with a higher photocurrent density. This higher photocurrent density could be interpreted as improved interparticle connectivity among the HS-TiO<sub>2</sub> spheres. Panels a and b in Figure 2.5 show the diffusion coefficients and recombination lifetimes of the as-pressed HS-TiO<sub>2</sub> and TTB-treated HS-TiO<sub>2</sub> cells, calculated from IMPS and IMVS measurements in an effort to investigate the mechanism underlying the photocurrent improvement. The diffusion coefficients of the TTB-treated HS-TiO<sub>2</sub> electrode were higher across all measured photon flux ranges compared with those of the as-pressed HS-TiO<sub>2</sub> electrode. The rapid electron transport was consistent with a higher photocurrent density in the TTB-treated HS-TiO<sub>2</sub> electrodes; however, the recombination lifetime of the TTB-treated TiO<sub>2</sub> was indistinguishable from the corresponding value in the as-pressed HS-TiO<sub>2</sub> electrodes. Unlike general chemical treatments, such as TiCl<sub>4</sub>, [31, 32] the TTB treatment could not retard the recombination rate of the injected electrons. This result indicated that the TTB treatment could not change the

TiO<sub>2</sub> conduction band edge or the surface state, although it facilitated electron diffusion through the new anatase TiO<sub>2</sub> coating.

## 2.4 Conclusion

In this study, we proposed a new simple fabrication process for preparing flexible DSSCs at room temperature. We prepared HS-TiO<sub>2</sub> photoelectrodes using an electrospray method with a binder-free TiO<sub>2</sub> dispersion. The HS-TiO<sub>2</sub> film formed by this method yielded a large surface area and a highly porous structure. The conversion efficiency of the as-sprayed HS-TiO<sub>2</sub> particles on the plastic ITO-PEN substrate was poor due to poor interparticle connectivity among the as-sprayed HS-TiO<sub>2</sub> spheres. Two post-treatments were tested in an effort to enhance the interparticle connectivity. First, we mechanically compressed the films to form physically well-connected HS-TiO<sub>2</sub> structures. The conversion efficiency improved by a factor of 2 using this method. By optimizing the thickness of the photoelectrode and the compression conditions, the conversion efficiency of the flexible DSSCs reached a value of 5% for the as-pressed HS-TiO<sub>2</sub> photoelectrodes. An additional TTB low-temperature chemical treatment was applied, yielding highly efficient flexible DSSCs. The

resulting TTB-treated HS-TiO<sub>2</sub> photoelectrode displayed rapid electron transport, resulting in a maximum conversion efficiency of 5.57% under 1 sun illumination (100 mW cm<sup>-2</sup>). This simple, cost-effective electrospray method using two types of post-treatment shows promise for the fabrication of highly efficient flexible DSSCs.

## 2.5 Reference

- [1] O'regan, B.; Gratzel, M. *Nature* **1991**, 353, 737
- [2] Chiba, Y.; Islam, A.; Watanabe, Y.; Komiyama, R.; Koide, N.; Han, L. *Jpn. J. Appl. Phys* **2006**, 45, 638
- [3] Gratzel, M. *Inorg. Chem.* **2005**, 44, 6841
- [4] Nazeeruddin, M. K.; De Angelis, F.; Fantacci, S.; Selloni, A.; Viscardi, G.; Liska, P.; Ito, S.; Takeru, B.; Gratzel, M. *J. Am. Chem. Soc.* **2005**, **127**, 16835
- [5] Toivola, M.; Halme, J.; Miettunen, K.; Aitola, K.; Lund, P. D. *Int. J. Energy Res.* **2009**, 33, 1145
- [6] Durr, M.; Schmid, A.; Obermaier, M.; Rosselli, S.; Yasuda, A.; Nelles, G. *Nat. Mater.* **2005**, 4, 607
- [7] Yamaguchi, T.; Tobe, N.; Matsumoto, D.; Nagai, T.; Arakawa, H. *Sol. Energy Mater. Sol. Cells* **2010**, 94, 812
- [8] Boschloo, G.; Lindstrom, H.; Magnusson, E.; Holmberg, A.; Hagfeldt, A. *J. Photochem. Photobiol., A* **2002**, 148, 11
- [9] Zhang, D.; Yoshida, T.; Furuta, K.; Minoura, H. *J. Photochem. Photobiol., A* **2004**, 164, 159
- [10] Miyasaka, T.; Ikegami, M.; Kijitori, Y. *J. Electrochem. Soc.* **2007**, 154,
- [11] Li, X.; Lin, H.; Li, J.; Wang, N.; Lin, C.; Zhang, L. *J. Photochem.*

*Photobiol., A* **2008**, 195, 247

[12] Kim, K.; Lee, G. W.; Yoo, K.; Kim, D. Y.; Kim, J. K.; Park, N. G. *J.*

*Photochem. Photobiol., A* **2009**, 204, 144

[13] Zhang, D.; Yoshida, T.; Oekermann, T.; Furuta, K.; Minoura, H. *Adv.*

*Funct. Mater.* **2006**, 16, 1228

[14] Yum, J. H.; Kim, S. S.; Kim, D. Y.; Sung, Y. E. *J. Photochem.*

*Photobiol., A.* **2005**, 173, 1

[15] Grinis, L.; Kotlyar, S.; Ruhle, S.; Grinblat, J.; Zaban, A. *Adv. Funct.*

*Mater.* **2010**, 20, 282

[16] Chen, H. W.; Liang, C. P.; Huang, H. S.; Chen, J. G.; Vittal, R.; Lin, C.

Y.; Kevin, C. W. W.; Ho, K. C. *Chem. Commun.* **2011**, 47, 8346

[17] Fujimoto, M.; Kado, T.; Takashima, W.; Kaneto, K.; Hayase, S. J.

*Electrochem. Soc.* **2006**, 153, A826

[18] Cha, S. I.; Koo, B. K.; Hwang, K. H.; Seo, S. H.; Lee, D. Y. *J. Mater.*

*Chem.* **2011**, 21, 6300

[19] Li, X.; Zhang, Y.; Zhang, Z.; Zhou, J.; Song, J.; Lu, B.; Xie, E.; Lan, W.

*J. Power Sources* **2010**, 196, 1639

[20] Park, N. G.; Kim, K. M.; Kang, M. G.; Ryu, K. S.; Chang, S. H.; Shin,

Y. J. *Adv. Mater.* **2005**, 17, 2349

[21] Uchida, S.; Tomiha, M.; Takizawa, H.; Kawaraya, M. *J. Photochem.*

*Photobiol., A* **2004**, 164, 93

[22] Chou, T. P.; Zhang, Q.; Fryxell, G. E.; Cao, G. *Adv. Mater.* **2007**, 19, 2588

[23] Chen, D.; Huang, F.; Cheng, Y. B.; Caruso, R. A. *Adv. Mater.* **2009**, 21, 2206

[24] Kim, Y. J.; Lee, M. H.; Kim, H. J.; Lim, G.; Choi, Y. S.; Park, N. G.; Kim, K.; Lee, W. I. *Adv. Mater.* **2009**, 21, 3668

[25] Hwang, D.; Lee, H.; Jang, S.-Y.; Jo, S. M.; Kim, D.; Seo, Y.; Kim, D. Y. *ACS Appl. Mater. Interfaces* **2011**, 3, 2719

[26] Jaworek, A. *J. Mater. Sci.* **2007**, 42, 266

[27] Jaworek, A. *Powder Technol.* **2007**, 176, 18

[28] Fan, K.; Peng, T.; Chen, J.; Dai, K. *J. Power Sources* **2010**, 196, 2939

[29] Park, N. G.; Van de Lagemaat, J.; Frank, A. *J. Phys. Chem. B* **2000**, 104, 8989

[30] Tan, W.; Chen, J.; Zhou, X.; Zhang, J.; Lin, Y.; Li, X.; Xiao, X. *J. Solid State Electrochem.* **2009**, 13, 651

[31] Sommeling, P. M.; O'Regan, B. C.; Haswell, R. R.; Smit, H. J. P.; Bakker, N. J.; Smits, J. J. T.; Kroon, J. M.; van Roosmalen, J. A. M. *J. Phys. Chem. B* **2006**, 110, 19191

[32] O'Regan, B. C.; Durrant, J. R.; Sommeling, P. M.; Bakker, N. J. *J. Phys.*

*Chem. C* **2007**, 111, 14001

# Chapter 3

## **Enhanced long-term stability of room-temperature fabricated DSSCs by stabilized binding of N719 dye**

### **3.1 Introduction**

Flexible substrate-based dye-sensitized solar cells (DSSCs) have several advantages among the various next-generation solar cells: they are bendable, light-weight, flexible, and may be fabricated through eco-friendly processes [1-3]. Flexible DSSCs with polymeric substrates, such as PET (polyethylene terephthalate) or PEN (polyethylene naphthalate), should generally be fabricated without high-temperature sintering processes due to the poor thermal stability of the polymeric substrates. The limits on the fabrication temperature result in poor interparticle necking and slow electron transport, i.e., poor photovoltaic performances [4]. For this reason, a large number of studies over the last decade have focused on processes for fabricating highly efficient flexible photoelectrodes, such as doctor-blading of binder-free titania [5-7], mechanical compression [8-11], chemical sintering [12-16], electrode transfer [17], electrophoretic deposition [18-21], microwave/laser

sintering [22-24], and spray deposition [25-27]. Although improving the efficiency of devices fabricated under low-temperature condition is important, the long-term stability of low-temperature fabricated TiO<sub>2</sub> photoelectrode is also important. The long-term stability of high-temperature sintered TiO<sub>2</sub> photoelectrode for glass-substrate based devices has been studied extensively, including electrolyte durability [28,29], dye anchoring durability [30,31], and surface treatment of TiO<sub>2</sub> electrode [32,33]. On the contrary, few researches have been studied with low-temperature fabricated TiO<sub>2</sub> photoelectrode due to the limiting factor such as humidity permeability of polymeric substrate, sealing problem, and degradable electronic properties of ITO conductive layer under acid or base condition [34,35].

Ikegami *et al.* demonstrated DSSC module consisting of a LiI-free electrolyte, which shows better long-term stability than LiI containing electrolyte on flexible substrate [36]. Lee *et al.* reported that introduction of tetrabutylammonium iodide in an liquid electrolyte shows better long-term stability [37]. Ho *et al.* reported that an insertion of TiO<sub>x</sub> buffer layer enhance the mechanical durability of flexible TiO<sub>2</sub> photoelectrode and SJW-1 organic sensitizer shows better long-term stability than N719 dye [7] .

Cheng *et al.* suggested the degradation mechanism of flexible DSSCs prepared by cold isostatic compression method [9].

Recently, our group reported the binder-free low-temperature fabrication of a highly efficient flexible DSSC using electrospray methods [38]. We obtained hierarchically structured TiO<sub>2</sub> (HS-TiO<sub>2</sub>) spheres with an average diameter of 600 nm. The HS-TiO<sub>2</sub> photoelectrode prepared by electrospray method exhibited a highly porous structure (Figure 3.1(a) and 3.1(b)). The power conversion efficiency (PCE) under 100 mW cm<sup>-2</sup> illumination of a glass-based substrate reached 10.4%, whereas the PCE of a flexible PEN-based substrate reached 5.5% [38,39]. The primary nanocrystalline TiO<sub>2</sub> particles were bead-milled in order to create stabilized TiO<sub>2</sub> dispersions without an organic binder prior to electrospray deposition. The surface functional groups on the primary TiO<sub>2</sub> particles may change under the strong mechanical friction among zirconia beads and TiO<sub>2</sub> particles in a hydrophilic medium (ethanol) during bead-milling processes. ATR-FTIR studies revealed the presence of excess surface hydroxyl groups on the bead-milled TiO<sub>2</sub> surfaces. The presence of additional surface OH groups was reduced after applying a high-temperature sintering process (Figure 3.2). This different surface functionality of R-TiO<sub>2</sub> photoelectrode may induce different binding environment of adsorbed dye and photovoltaic properties.

Although much research has focused on the binding mode of the N719 dyes with various TiO<sub>2</sub> photoelectrode, these studies have not discussed the photovoltaic performances or long-term stability of the TiO<sub>2</sub> surface functional groups.

Here, we first investigated the properties of room-temperature fabricated TiO<sub>2</sub> (R-TiO<sub>2</sub>) photoelectrode by considering the effects of different surface functionality on the photovoltaic performances and long-term stability. Also, we demonstrate a modification of dye anchoring on R-TiO<sub>2</sub> photoelectrode using stearic acid as co-adsorbent. The competitive adsorption of N719 dye with stearic acid (SA) can decrease adsorption rate of N719 dye and increase the fraction of strongly bound dye on TiO<sub>2</sub> surface [40]. The SA-treated R-TiO<sub>2</sub> (RS-TiO<sub>2</sub>) photoelectrode showed a dramatic enhancement in the long-term stability, 70.1% of its initial efficiency after 1000 h at 60°C under illumination of 100 mW cm<sup>-2</sup>. Finally, we proposed stabilized binding mode of dye on different TiO<sub>2</sub> photoelectrode. UV-vis and ATR FT-IR spectroscopic studies were conducted to identify the dye adsorption/desorption mechanism and bound state of N719. The high-temperature sintered TiO<sub>2</sub> (H-TiO<sub>2</sub>) photoelectrode was also examined using the same methods as reference electrode. The enhanced long-term

stability of R-TiO<sub>2</sub> photoelectrode reported here can provide useful information for achieving more stable flexible DSSCs.

## 3.2 Experimental

### 3.2.1 Materials

Fluorine-doped tin oxide (FTO) glass (TEC-8, Pilkington) was used as a transparent conducting substrate. The nanocrystalline P25 powder was purchased from Degussa and used to prepare a TiO<sub>2</sub> dispersion for electrospray processing. A ruthenium complex sensitizer (Ru535-bisTBA, Solaronix SA), *cis*-diisothiocyanato-bis(2,2'-bipyridyl-4,4'-dicarboxylato) ruthenium(II) bis(tetrabutylammonium), generally known as N719, was purified using ion exchange column chromatography. Iodine (I<sub>2</sub>, 99.99+%, Aldrich), 4-*tert*-butylpyridine (TBP, 99%, Aldrich), lithium iodide (LiI, 99.9%, Aldrich), 1-butyl-3-methylimidazolium iodide (BMII, 99%, C-tri), acetonitrile (ACN, 99.8%, Aldrich), valeronitrile (VN, 99.5%, Aldrich), and

stearic acid (SA, 99.5%, Fluka) were used as purchased without further purification.

### **3.2.2 Preparation of TiO<sub>2</sub> photoelectrodes**

The hierarchically structured mesoporous TiO<sub>2</sub> photoelectrodes were prepared according to the reported procedure.[38,39] The 10% (wt/v) P25 (Degussa) was dispersed in anhydrous ethanol using an ultra apex mill (Model UAM-015, Kotobuki). The stabilized P25 dispersion was loaded into a plastic syringe infusion pump (KD Scientific Model 220) connected to a high-voltage power supply (Bertan Series 205B). The solution was then electrospayed directly onto the conducting FTO (TEC-8, Pilkington) substrate. Environmental effects, such as electrolyte leakage, were minimized by assembling all devices with FTO glass. An electric field of 1.5 kV cm<sup>-1</sup> was applied between the metal orifice and the conducting substrate with a feed rate of 40 μL min<sup>-1</sup>. A motion control system governed by a microprocessor (Dasa Tech) was used to control the nozzle and substrate during deposition to produce a uniformly thick film over a large area.

### 3.2.2 Device Fabrication

After electrospray processing, the as-sprayed TiO<sub>2</sub> photoelectrode was pressed for 10 min with a pressures of 10 MPa. The as-pressed photoelectrode was then immersed in a purified 0.3 mM N719 tert-butanol/acetonitrile (50/50 v/v) solution for 24 h at room temperature to produce the room-temperature fabricated TiO<sub>2</sub> (R-TiO<sub>2</sub>) electrode. High-temperature sintered TiO<sub>2</sub> (H-TiO<sub>2</sub>) electrodes were prepared by sintering the as-pressed TiO<sub>2</sub> photoelectrodes at 500°C for 30 min under ambient air. After cooling to room temperature, the H-TiO<sub>2</sub> electrodes were immersed in a 0.3 mM N719 solution for 24 h at room temperature. After 24 h, the immersed TiO<sub>2</sub> electrodes were rinsed with anhydrous ethanol and dried under a nitrogen flow. A Pt counter electrode was prepared by drop-casting 5 mM H<sub>2</sub>PtCl<sub>6</sub> in isopropyl alcohol onto the washed FTO glass, followed by sintering at 400°C for 20 min. The dye-sensitized TiO<sub>2</sub> and Pt electrodes were assembled and sealed carefully using a thermal adhesive film (Surlyn, DuPont 1702, 60 μm thick) as a spacer to fabricate sandwich-type cells. The active area of a cell was typically 0.25 cm<sup>2</sup>. The liquid electrolyte consisted

of 0.65 M 1-butyl-3-methylimidazolium (BMII), 0.03 M iodine (I<sub>2</sub>), 0.1 M lithium iodide (LiI), and 0.5 M 4-*tert*-butylpyridine (TBP) in a mixture of acetonitrile (ACN) and valeronitrile (VN) (85/15 v/v). An electrolyte solution was injected through a pre-drilled hole in the counter electrode. Finally, the pre-drilled holes were sealed using a thermal adhesive film and cover glass.

### **3.2.3 UV-Vis spectroscopy measurement**

The quantities of adsorbed dye present on the TiO<sub>2</sub> surfaces were measured by UV-Vis spectroscopy. The amount of dye adsorbed onto a TiO<sub>2</sub> surface was determined by immersing the dye-sensitized TiO<sub>2</sub> electrode in a 0.1 M NaOH aqueous solution, and the absorbance of the resulting solution was measured. The absorption spectra of the solutions were measured using a UV-Vis spectrophotometer (Agilent 8453).

### **3.2.4 ATR FT-IR spectroscopy measurement**

The prepared dye-sensitized TiO<sub>2</sub> photoelectrodes were analyzed using attenuated total reflectance FT-IR (ATR FT-IR) spectrometry (Nicolet 6700, Thermo Scientific). Spectra were obtained from 64 scans at a resolution of 4 cm<sup>-1</sup>. The samples were analyzed under the constant mechanical force of an ATR accessory used to press the samples. The effects of the environmental contamination or adsorbed organic molecules on the TiO<sub>2</sub> surfaces were minimized by rinsing the prepared TiO<sub>2</sub> electrodes with acetonitrile and ethanol. The washed TiO<sub>2</sub> photoelectrodes were then stored in vacuum chambers prior to collecting the measurements.

### **3.2.5 Photoelectrochemical characterization**

Photovoltaic measurements of the DSSCs were conducted using an AM 1.5 solar simulator and a 450 W Xe lamp. The intensity of the simulated light was calibrated using a Si reference solar cell to yield AM 1.5 global irradiation. The photovoltaic characteristics of the DSSC were obtained by applying an external potential bias to the cells and by measuring the photocurrent generated using a Keithley model 2400 source meter. The electron transport time and electron recombination lifetime were measured using intensity-modulated photocurrent spectroscopy (IMPS) and intensity-

modulated photovoltage spectroscopy (IMVS). A diode laser with variable power and modulation control (Coherent Lab-laser, 40 mW, 446 nm) was used as the light source. The illumination was always applied incident to the working electrode side of the solar cell. The light intensity was measured using a calibrated Si photodiode. IMVS was performed under open-circuit conditions. The output of the solar cell was connected directly to a frequency response analyzer (Schlumberger–Solartron SI 1260). IMPS measurements were performed by connecting the solar cell via a potentiostat amplifier (EG&G PAR 273) to the frequency response analyzer. During the IMPS and IMVS measurements, the cell was illuminated with sinusoidally modulated light having a small AC component (10% or less of the DC component). Long-term stability measurements were performed in a simulator at 60°C under illumination of 100 mW cm<sup>-2</sup>. A halogen lamp was used as the light source for the stability test. The temperature was controlled using a thermocouple and cooling fan in an adiabatic chamber.

## **3.3 Results and discussion**

### **3.3.1 Initial efficiency**

The room-temperature fabricated TiO<sub>2</sub> photoelectrodes (R-TiO<sub>2</sub>) and high-temperature sintered TiO<sub>2</sub> photoelectrodes (H-TiO<sub>2</sub>) were made using electrospray method. A major difference between R-TiO<sub>2</sub> and H-TiO<sub>2</sub> is that the TiO<sub>2</sub> electrode in the former is fabricated without thermal sintering and in the latter is sintered at 500°C for 30 min. The TiO<sub>2</sub> photoelectrodes prepared by binder-free electrospray method showed hierarchical structure as shown in Figure 1(a) and 1(b). The individual secondary TiO<sub>2</sub> spheres with an average size of 600 nm consisted of nanocrystalline P25 TiO<sub>2</sub> particles. This hierarchically structured metal oxide particles are advantageous in that they provide (1) large surface area, (2) porous structure, and (3) rapid electron transport [38,39]. Figure 1(c) and Table 1 shows initial J-V characteristics and photovoltaic parameters of the assembled devices. The H-TiO<sub>2</sub> cell displayed an efficiency of 8.1%, whereas the R-TiO<sub>2</sub> cell showed an efficiency of 6.3%. As shown in Figure 1(c) and Table 1, the low conversion efficiency of the R-TiO<sub>2</sub> cell arose from its low photocurrent density (11.64 mA cm<sup>-2</sup> for R-TiO<sub>2</sub> and 15.76 mA cm<sup>-2</sup> for H-TiO<sub>2</sub>). In general, the photoelectrodes prepared without thermal sintering showed poor charge collection efficiency due to a lack of inter-particle connectivity at the grain boundaries [4].

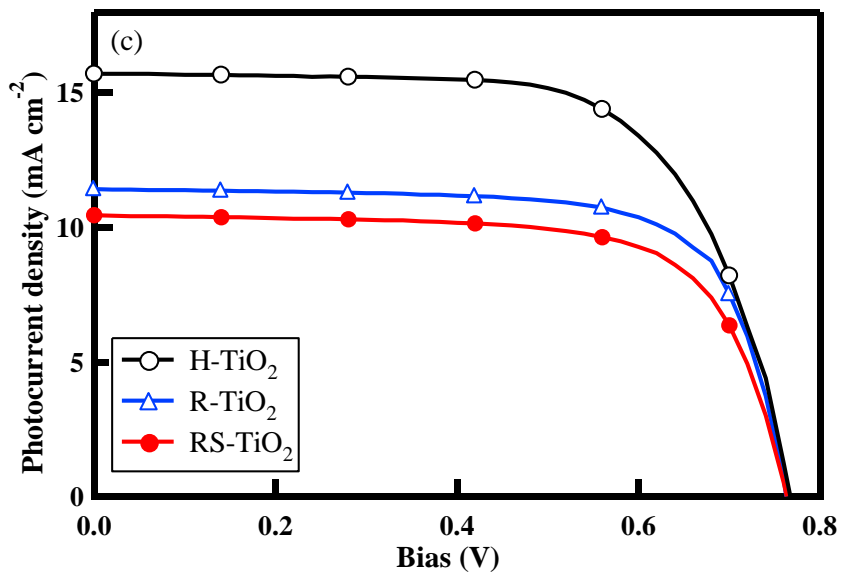
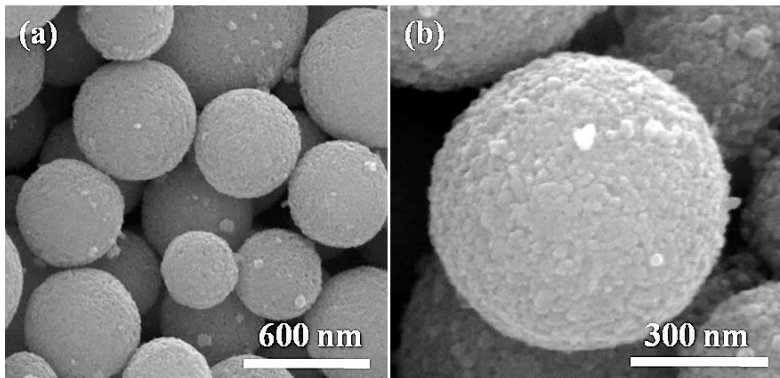


**Figure 3.1** (a), (b) SEM images of hierarchically structured R-TiO<sub>2</sub> photoelectrode and (c) Initial J-V characteristics of H-TiO<sub>2</sub>, R-TiO<sub>2</sub>, and RS-TiO<sub>2</sub> photoelectrodes

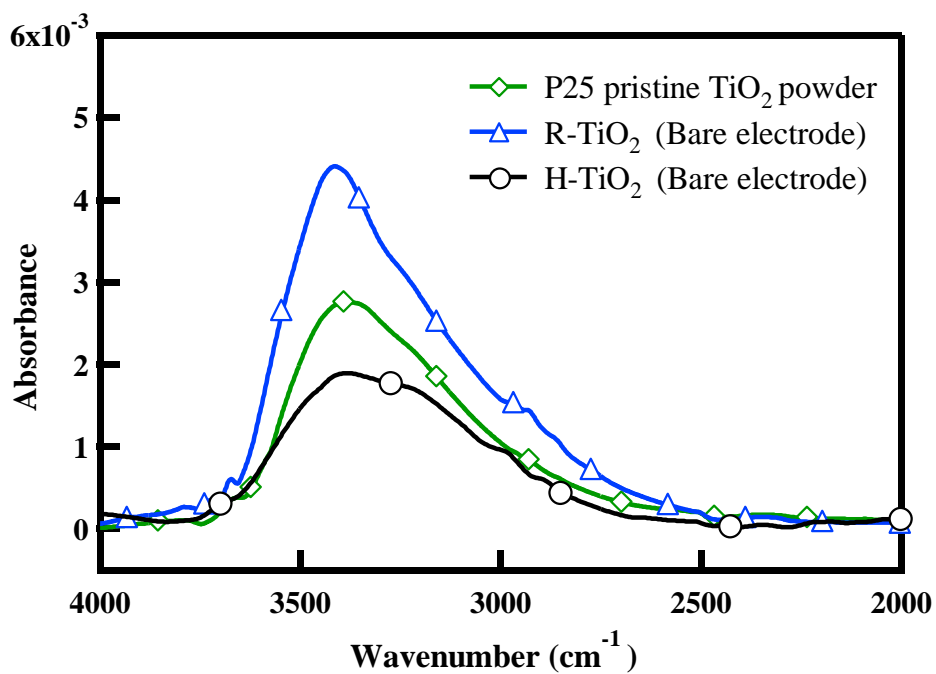


**Figure 3.2** ATR-FTIR spectra of P25 pristine TiO<sub>2</sub> powder (dashed green), H-TiO<sub>2</sub> (solid black) and R-TiO<sub>2</sub> (solid blue), bare electrodes

Photoelectrode	Time (h)	V <sub>oc</sub> (V)	J <sub>sc</sub> (mA cm <sup>-2</sup> )	FF	PCE (%)	J <sub>sc(t)</sub> / J <sub>sc(0)</sub> (%)	PCE <sub>(t)</sub> / PCE <sub>(0)</sub> (%)
H-TiO <sub>2</sub>	0	0.767	15.76	0.67	8.10	100	100
	400	0.760	13.54	0.68	7.00	85.9	84.9
	1000	0.722	11.96	0.71	6.13	75.9	75.7
R-TiO <sub>2</sub>	0	0.764	11.64	0.71	6.30	100	100
	400	0.724	6.38	0.70	3.22	54.8	51.3
	1000	0.702	4.28	0.73	2.20	36.8	34.8
RS-TiO <sub>2</sub>	0	0.767	10.55	0.72	5.82	100	100
	400	0.765	8.48	0.71	4.61	80.4	79.1
	1000	0.731	7.86	0.71	4.08	74.5	70.1

**Table 3.1** Photovoltaic properties of the H-TiO<sub>2</sub>, R-TiO<sub>2</sub>, and RS-TiO<sub>2</sub> photoelectrode with a TiO<sub>2</sub> film thickness of 9 μm as function of aging time

The charge collection efficiencies of the H-TiO<sub>2</sub> and R-TiO<sub>2</sub> were confirmed using IMPS (Intensity Modulated Photocurrent Spectroscopy) and IMVS (Intensity Modulated Photovoltage Spectroscopy). The calculated electron diffusion coefficients and recombination lifetimes were plotted in Figure 3.3. The H-TiO<sub>2</sub> electrode displayed an order of magnitude greater electron diffusion coefficient and a slightly slower recombination rate compared to the R-TiO<sub>2</sub> electrode. The superior charge transport properties increased  $J_{SC}$  in the H-TiO<sub>2</sub> devices. The difference between the  $J_{SC}$  values of the H-TiO<sub>2</sub> and R-TiO<sub>2</sub> devices could be explained as resulting from the higher electron diffusion coefficient of the H-TiO<sub>2</sub> photoelectrode, which had been submitted to thermal sintering. The H-TiO<sub>2</sub> and R-TiO<sub>2</sub> electrodes in our e-sprayed TiO<sub>2</sub> system differed in another important way: the R-TiO<sub>2</sub> electrode surface presented a larger number of hydroxyl groups than the H-TiO<sub>2</sub> electrode (See Figure 3.2). Therefore, the adsorption rate and amounts of adsorbed dye on TiO<sub>2</sub> surface were estimated using UV absorption spectra measurements (as summarized in Figure 3.4(a) and Table 3.2). As shown in Figure 3.4(a), the N719 dyes were adsorbed on rapidly in a few hours, and then the dye-loading slowed down afterward reaching saturation. But, dye uptake on L-TiO<sub>2</sub> photoelectrode was faster than H-TiO<sub>2</sub> photoelectrode. The faster adsorption kinetics of N719 dye results

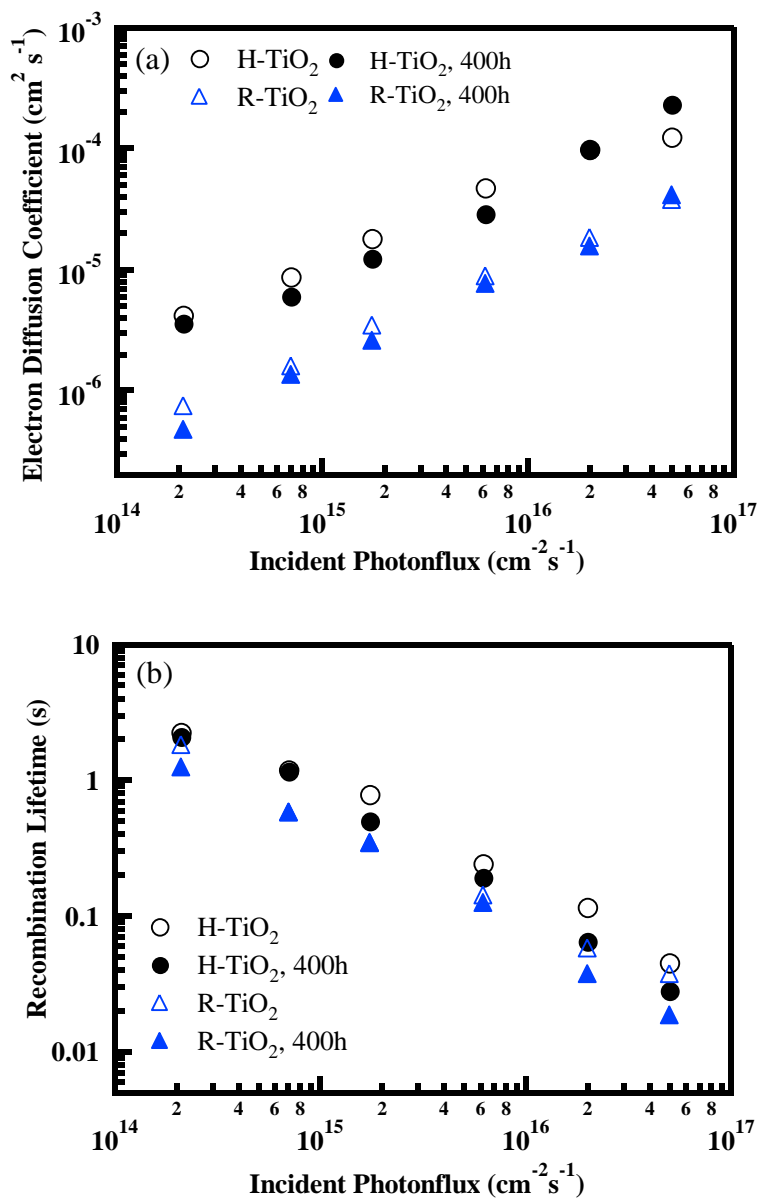


**Figure 3.3** Electron diffusion coefficients (a) and recombination lifetime (b) of the DSSCs based H-TiO<sub>2</sub>, and R-TiO<sub>2</sub> photoelectrodes as a function of incident photon flux for 446 nm modulated (<10%) laser illumination.

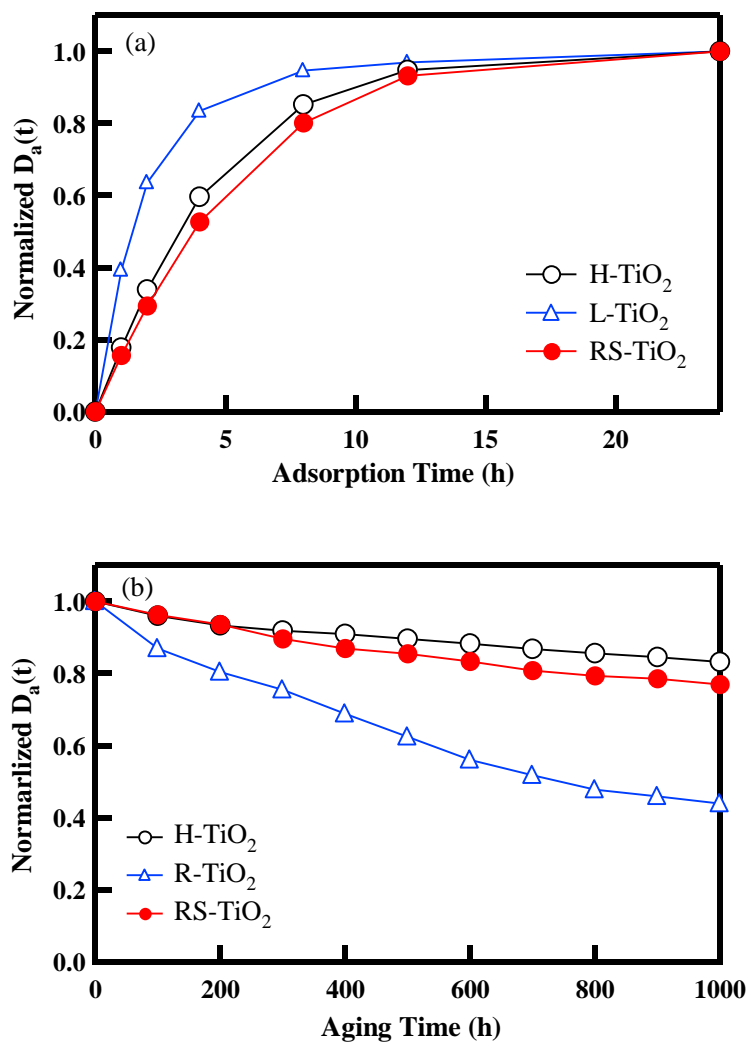


**Figure 3.4** (a) Normalized amounts of adsorbed dye on each  $\text{TiO}_2$  surface in 0.3 mM N719 solution as a function of adsorption time and (b) aging time at  $60^\circ\text{C}$  under illumination of  $100 \text{ mW cm}^{-2}$ . Y-axis is normalized by saturation amount of adsorbed dye on  $\text{TiO}_2$  surface

from OH-rich surface of L-TiO<sub>2</sub> photoelectrode. Also, The quantity of dye molecules ( $6.22 \times 10^{-8}$  mol mg<sup>-1</sup>) adsorbed onto the R-TiO<sub>2</sub> electrode exceeded that absorbed onto the H-TiO<sub>2</sub> electrode ( $5.55 \times 10^{-8}$  mol mg<sup>-1</sup>), since the excess hydroxyl groups on the R-TiO<sub>2</sub> surface increased dye loading (Table 2). These results were consistent with the ATR FT-IR results shown in Figure 3.2 and the data previously reported results [41]. The initial low photocurrent density in the R-TiO<sub>2</sub> cells appeared to arise from the poor charge transport properties of the electrode, despite a high dye loading on the R-TiO<sub>2</sub> surface due to large amount of surface hydroxyl group. The anchoring modes of adsorbed dyes on each TiO<sub>2</sub> photoelectrode will be discussed in detail..

### **3.3.2 Long-term stability**

Figure 3.5 and Table 3.1 show the long-term stability performances and photovoltaic parameters of the H-TiO<sub>2</sub> and R-TiO<sub>2</sub> electrodes over 1000 h at 60°C with illumination of 100 mW cm<sup>-2</sup>. The power conversion efficiencies (PCE) of both the H-TiO<sub>2</sub> and R-TiO<sub>2</sub> devices decreased steadily over 1000 h, but the slopes of the efficiency as a function of time was different. The PCE of the H-TiO<sub>2</sub> device operated over 400 h was 7.00%, that is, 84.9% of

its initial efficiency. After 1000 h, the PCE was 6.13%, that is, 75.7% of its initial efficiency. In contrast with the H-TiO<sub>2</sub> device, the R-TiO<sub>2</sub> devices showed poor long-term stability. The PCE of R-TiO<sub>2</sub> after 400 h was 3.22%, 51.3% of its initial efficiency. After 1000 h, the PCE decreased even further to 2.20%, 34.8% of its initial efficiency. Interestingly, the PCE degradation trend agreed with the  $J_{SC}$  degradation obtained for both the H-TiO<sub>2</sub> and R-TiO<sub>2</sub> devices as shown in Table 3.1. This observation indicated that the  $J_{SC}$  of the device was key to the long-term stability of the dye-sensitized solar cell performance.

Theoretically,  $J_{SC}$  can be calculated using the IPCE spectrum (Equation 1)

$$J_{SC} = \int eIPCE(\lambda)I_S(\lambda)d\lambda \quad \text{Eq. 1}$$

Where  $e$ ,  $IPCE(\lambda)$ ,  $I_S(\lambda)$ , and  $\lambda$  are the electron charge, incident photon to current efficiency, incident photon flux density, and incident photon wavelength, respectively.

The IPCE efficiency is the product of three quantum efficiencies, as expressed by Equation 2,

$$IPCE(\lambda) = \eta_{LHE} \times \eta_{INJ} \times \eta_{COL} \quad \text{Eq.2}$$

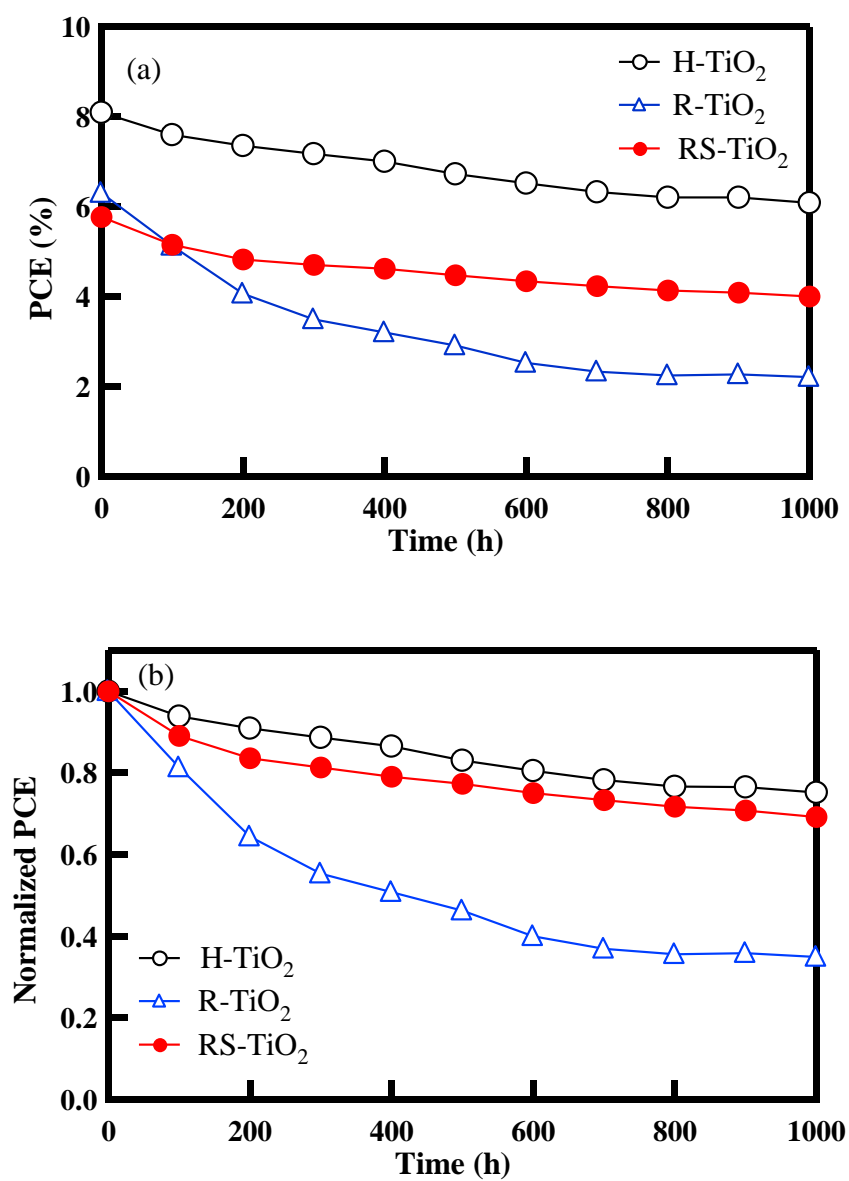


**Figure 3.5** (a) Power conversion efficiencies (PCE) and (b) normalized PCE of H-TiO<sub>2</sub>, R-TiO<sub>2</sub>, and RS-TiO<sub>2</sub> photoelectrodes as a function of aging time

where  $\eta_{LHE}$ ,  $\eta_{INJ}$ , and  $\eta_{COL}$  are the light harvest efficiency, charge injection efficiency, and charge collection efficiency, respectively. The light harvesting, charge injection and charge collection efficiencies are related to the adsorbed dye concentration, the fraction of photons absorbed by the dye that are converted into conduction band electrons, and the degree of TiO<sub>2</sub> inter-particle connectivity. We found that the major differences between R-TiO<sub>2</sub> and H-TiO<sub>2</sub> photoelectrode were amount of adsorbed dye and charge transport properties. Therefore, we evaluated the light harvesting efficiency and charge collection efficiency of the R-TiO<sub>2</sub> photoelectrode as function of aging time in order to demonstrate  $J_{SC}$  degradation mechanism of R-TiO<sub>2</sub> devices.

First, the amount of adsorbed dyes on H-TiO<sub>2</sub> and R-TiO<sub>2</sub> were examined as a function of aging time using UV spectroscopy. Figure 3.5(b) and Table 3.2 show the calculated amount of adsorbed N719 dye on each TiO<sub>2</sub> photoelectrode. As shown in Figure 3.5(b), the amount of bound N719 dyes on R-TiO<sub>2</sub> surface decreased rapidly as time goes on. The calculated concentration of dye molecules adsorbed on the R-TiO<sub>2</sub> surface aging for 400 h,  $D_{400}$  (R-TiO<sub>2</sub>) was  $4.28 \times 10^{-8}$  mol mg<sup>-1</sup>, 68.8% ( $D_{400}/D_0$ ) of the total initial amount of dye molecules adsorbed onto the TiO<sub>2</sub> surface,  $D_0$  (R-TiO<sub>2</sub>). After 1000 h, only  $2.73 \times 10^{-8}$  mol mg<sup>-1</sup> ( $D_{1000}$ ), 43.9% ( $D_{1000}/D_0$ ) of

Photoelectrode	D <sub>0</sub> (mol mg <sup>-1</sup> ) <sup>a</sup>	D <sub>400</sub> (mol mg <sup>-1</sup> ) <sup>a</sup>	D <sub>1000</sub> (mol mg <sup>-1</sup> ) <sup>a</sup>	D <sub>400</sub> / D <sub>0</sub> (%)	D <sub>1000</sub> / D <sub>0</sub> (%)
H-TiO <sub>2</sub>	5.55 × 10 <sup>-8</sup>	5.05 × 10 <sup>-8</sup>	4.61 × 10 <sup>-8</sup>	91.0	83.1
R-TiO <sub>2</sub>	6.22 × 10 <sup>-8</sup>	4.28 × 10 <sup>-8</sup>	2.73 × 10 <sup>-8</sup>	68.8	43.9
RS-TiO <sub>2</sub>	5.84 × 10 <sup>-8</sup>	5.08 × 10 <sup>-8</sup>	4.49 × 10 <sup>-8</sup>	87.0	76.9

**Table 3.2** Summary of the amount of adsorbed N719 dye on each TiO<sub>2</sub> photoelectrodes with different aging time at 60°C under illumination of 100 mW cm<sup>-2</sup>

- a. D<sub>0</sub>, D<sub>400</sub>, and D<sub>1000</sub> are measured amount of adsorbed on TiO<sub>2</sub> surface after 0 h, 400 h, and 1000 h, respectively. The amount of adsorbed dye on aged TiO<sub>2</sub> surface was measured by opening the assembled cells after a number of aging hours and desorbing the dye from aged TiO<sub>2</sub> surface.

the total initial amount of dye remained on R-TiO<sub>2</sub> surface. In the case of sintered H-TiO<sub>2</sub> photoelectrodes, D<sub>400</sub> and D<sub>1000</sub> were  $5.05 \times 10^{-8}$  mol mg<sup>-1</sup> and  $4.61 \times 10^{-8}$  mol mg<sup>-1</sup>, which were 91.0% (D<sub>400</sub>/D<sub>0</sub>) and 83.1% (D<sub>1000</sub>/D<sub>0</sub>) of initial amount of adsorbed dye on TiO<sub>2</sub> surface, respectively. Figure 3.6 shows photographic images of the H-TiO<sub>2</sub> (top) and R-TiO<sub>2</sub> (middle) photoelectrodes after aging for different times at 60°C under the illumination of 100 mW cm<sup>-2</sup>. The N719 dyes on the R-TiO<sub>2</sub> surface were found to be significantly desorbed from the surface. These results indicated the  $J_{SC}$  values of the R-TiO<sub>2</sub> device were related to the amount of dye adsorbed on TiO<sub>2</sub> photoelectrode, as characterized by  $\eta_{LHE}$ .

The electron diffusion coefficient and recombination lifetimes of the H-TiO<sub>2</sub> and R-TiO<sub>2</sub> electrodes after aging for 400 h were also investigated in relation to  $\eta_{COL}$ . The calculated diffusion coefficients and recombination lifetimes are shown in Figure 3.3. As discussed above, the diffusion coefficients of H-TiO<sub>2</sub> were an order of magnitude higher than those of the R-TiO<sub>2</sub> electrode in its initial state. Unlike the dye desorption measurements, the diffusion coefficients and recombination lifetimes in both the H-TiO<sub>2</sub> and R-TiO<sub>2</sub> photoelectrodes aged for 400 h showed similar values to the initial values over a given incident photon flux. In other words, the charge transport properties (i.e.,  $\eta_{COL}$ ) in both cells remained constant after aging

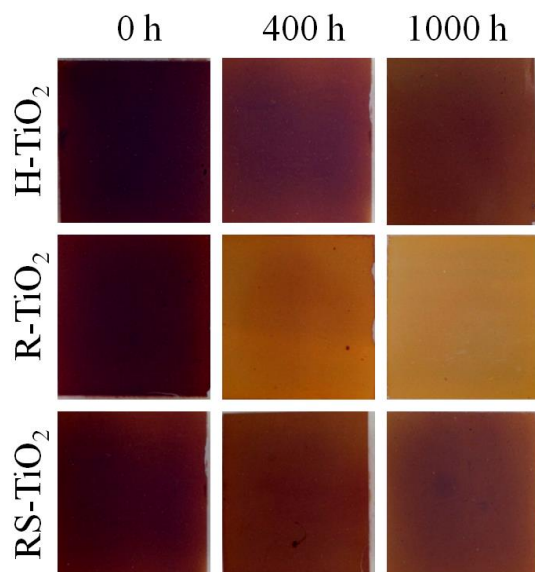


**Figure 3.6** Photographs of the N719-sensitized H-TiO<sub>2</sub> (top), R-TiO<sub>2</sub> (middle), and RS-TiO<sub>2</sub> (bottom) after aging

for 400 h. We concluded that the significant decrease in  $J_{SC}$  for the R-TiO<sub>2</sub> devices arose not from the degradation of the charge transport properties, but from the desorption of anchored N719 dyes on the R-TiO<sub>2</sub> surface.

### **3.3.3 Binding mode of N719 on H-TiO<sub>2</sub> and R-TiO<sub>2</sub> electrode**

The anchoring mode of ruthenium (II) complexes containing polypyridyl ligands, such as N719, on TiO<sub>2</sub> surface has been examined largely using vibrational spectroscopy [42-45]. The N719 dye binds to the TiO<sub>2</sub> surface through carboxylic acid groups. Anchoring through all four carboxylic acid groups was deemed unfavorable for steric reasons, and only two carboxylic acid groups on N719 are thought to be involved in a bidentate bridge coordination geometry. The detailed mechanism by which N719 dyes anchor onto TiO<sub>2</sub> surface functional groups has not yet been elucidated. Nazeeruddinet *et al.* and Shkloveret *et al.* have presented data in support of N719 chemisorption through two carboxylic acid groups [43,46]. Demopoulos *et al.* proposed that only one carboxylic acid group formed a covalent bidentate bond and the other carboxylic acid group attached onto

the TiO<sub>2</sub> surface through electrostatic interactions and hydrogen bonding via surface OH groups [45]. Hirose *et al.* proposed that the adsorption of N719 on the TiO<sub>2</sub> surface was facilitated by the presence of surface OH sites [47,48]. Wang *et al.* reported that surface OH groups introduced by O<sub>2</sub> plasma treatment increased dye adsorption [49]. Also, Several groups have reported the spectra of pure TiO<sub>2</sub> and N719-sensitized TiO<sub>2</sub> films as part of their investigations of the N719 binding mode; however, spectra of dye-sensitized TiO<sub>2</sub> photoelectrodes prepared under room-temperature condition have not been extensively described.

The relation between amount of surface hydroxyl groups and dye binding mode was investigated using ATR FT-IR. All TiO<sub>2</sub> samples showed a broad band at 3380 cm<sup>-1</sup>, indicating surface hydroxyl groups. The intensity of the peak corresponding to hydroxyl groups present on the R-TiO<sub>2</sub> photoelectrode surface was strong in comparison to that of the H-TiO<sub>2</sub> photoelectrode. As shown in Figure 3.4(a) and Table 2, the abundant surface hydroxyl groups not only facilitated dye loading on the R-TiO<sub>2</sub> photoelectrode, they increased the first carboxylation reaction rate on the TiO<sub>2</sub> surface, which was the rate-limiting step in the dye anchoring process.[40] If the reaction rate of the first carboxylation reaction were to increase to a level equal to the rate of the second (intramolecular)

carboxylation reaction, the second carboxylic acid in a given N719 dye may compete with the first carboxylic acid in a second dye in the reaction with a neighbor hydroxyl anchoring site. Competition between the first and second carboxylic reactions would produce weakly bound N719 molecules with only one covalently bound carboxylate group. Therefore, the weakly bound N719 molecules, bound via one covalent bond on the R-TiO<sub>2</sub> surface, most likely resulted from conditions that favored the faster adsorption of N719 in the presence of abundant surface hydroxyl groups on R-TiO<sub>2</sub>.

Figure 3.7 shows the relative ATR FT-IR spectra of the N719-sensitized TiO<sub>2</sub> photoelectrodes over the range 1300 cm<sup>-1</sup> – 1800 cm<sup>-1</sup>. All spectra were normalized by the amount of adsorbed dye on TiO<sub>2</sub> surface for quantitative analysis at the signal of 1540 cm<sup>-1</sup> (bipyridyl  $\nu(\text{C}=\text{C})$  absorption from N719 molecule). The spectra of the TiO<sub>2</sub> electrodes sensitized by N719 showed two strong bands at 1595 cm<sup>-1</sup> and 1370 cm<sup>-1</sup>, assigned to the asymmetric and symmetric stretching modes of the carboxylate groups  $\nu(\text{COO}^-)$ , respectively.[45] The sharp and slight weaker peaks at 1420 cm<sup>-1</sup> and 1544 cm<sup>-1</sup> were assigned to the bipyridyl  $\nu(\text{C}=\text{C})$  adsorption within the adsorbed N719 dye molecules on the TiO<sub>2</sub> surface.[50,51] The weak band at 1470 cm<sup>-1</sup> was assigned to the  $\delta(\text{CH}_2)$  band of the Bu<sub>4</sub>N<sup>+</sup> cations. Lastly, the band at 1730 cm<sup>-1</sup> was assigned to the  $\nu(\text{C}=\text{O})$  group in the free carboxylic

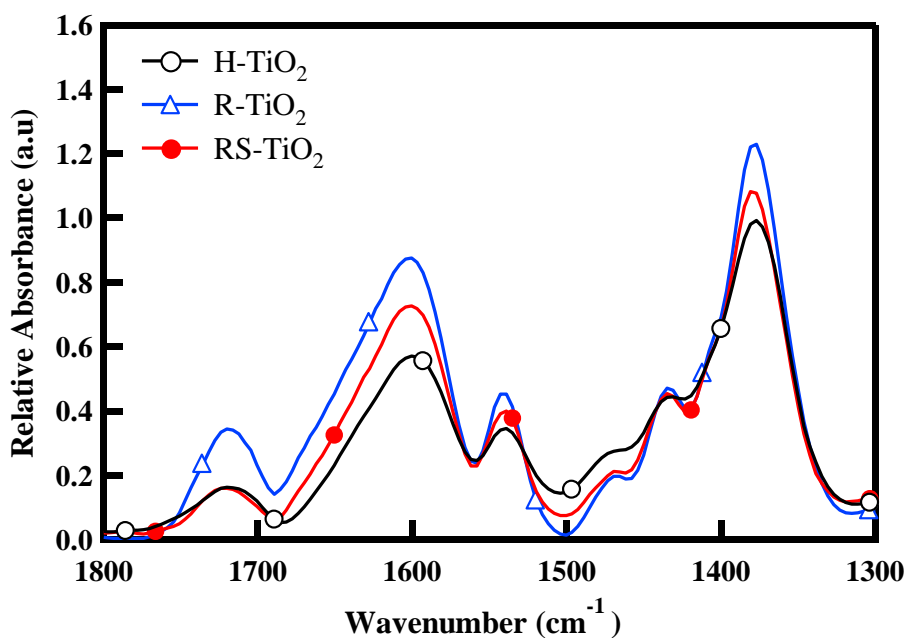


**Figure 3.7** Relative ATR FT-IR spectra of the TiO<sub>2</sub> electrodes sensitized 0.3 mM of N719 (H-TiO<sub>2</sub> and R-TiO<sub>2</sub>) and sensitized 0.3 mM of N719 with 3 mM of stearic acid (RS-TiO<sub>2</sub>). All spectra were normalized by the amount of adsorbed dye on each TiO<sub>2</sub> surface for quantitative analysis at the signal of 1540 cm<sup>-1</sup> (bipyridyl n(C=C) adsorption from N719 molecules).

acid group of the N719 molecule.[45,51,52] The band intensities shown in Figure 3.7 were assigned as follows:  $1370\text{ cm}^{-1}$  indicated the amounts of carboxylate groups that formed covalent bonds with the N719 molecules on the  $\text{TiO}_2$  surfaces,  $1540\text{ cm}^{-1}$  indicated the total amount of absorbed N719, and  $1730\text{ cm}^{-1}$  indicated the amount of weakly bound N719 molecules bonded through one covalent bond to the  $\text{TiO}_2$  surface and with one unreacted carboxylic acid.[40] This unreacted carboxylic acid groups in the N719 molecules may have been stabilized by hydrogen bonds to the hydroxyl groups on the  $\text{TiO}_2$  surface.[45] Therefore, the amount of weakly bound N719 could be evaluated based on the intensity of the peak at  $1730\text{ cm}^{-1}$ . As shown in Figure 3.7, the  $1730\text{ cm}^{-1}$  peak intensity in the spectrum obtained from the R- $\text{TiO}_2$  photoelectrode was much stronger than that of the H- $\text{TiO}_2$  photoelectrode. In other words, the quantity of weakly bound N719 molecules on the R- $\text{TiO}_2$  surface was larger than that present on the H- $\text{TiO}_2$  surface. This observation was consistent with our experimental results showing that dye desorption rarely occurred on the H- $\text{TiO}_2$  surfaces, but significantly occurred on the R- $\text{TiO}_2$  surface.

### **3.3.4 Effects of stearic acid (SA) on the efficiency and durability**

Recently, Park *et al.* investigated the stable anchoring of N719 sensitizer molecules by thermodynamically modifying the binding process through the introduction of stearic acid (SA) as a co-adsorbent [40]. The carboxylation of the SA coadsorbent competed with the first carboxylation reaction of N719 during the anchoring process on the surface hydroxyl groups so that the first carboxylation reaction associated with the N719 adsorption reaction was slowed. This SA-induced slowing of the first carboxylation anchoring process afforded N719 dyes with sufficient time for anchoring onto the TiO<sub>2</sub> surfaces through two carboxylic acid groups within the same dye. In other words, a lower first carboxylation reaction rate due to competition with SA enabled complete anchoring through two carboxylic acid groups in the N719 molecule. Park *et al.* also demonstrated that the N719 molecules adsorbed in the presence of SA exhibited slower desorption in the presence of an aqueous KOH solution. The N719-sensitized TiO<sub>2</sub> photoelectrodes prepared with SA showed enhanced long-term stability [40]. This approach was thought to be potentially effective for our own hydroxyl-rich R-TiO<sub>2</sub> surface because the presence of excess surface OH groups on R-TiO<sub>2</sub> results in large amounts of weakly bound N719 molecules on the TiO<sub>2</sub> surface. The slowing of N719 adsorption upon the addition of SA during the dye adsorption process may have potentially enabled strong binding between the

N719 dye molecules and the hydroxyl-rich-R-TiO<sub>2</sub> surfaces to provide superior long-term stability. We anchored the N719 molecules on the R-TiO<sub>2</sub> photoelectrode with 0.3 mM SA as a co-adsorbent (denoted RS-TiO<sub>2</sub>) to modify the binding mode of N719 on the R-TiO<sub>2</sub> surface. First, we measured the photovoltaic performance and the long-term stability. Figure 3.3(c) and Table 3.1 summarize the photovoltaic performances of the RS-TiO<sub>2</sub> cells. The initial conversion efficiency of the RS-TiO<sub>2</sub> cell showed 10.55 mA cm<sup>-2</sup> and 5.82% of  $J_{SC}$  and PCE, respectively. The effects on the dye concentration in RS-TiO<sub>2</sub> are summarized in Figure 3.5(a) and Table 2. Not only the RS-TiO<sub>2</sub> photoelectrodes showed slower dye adsorption rate, but the RS-TiO<sub>2</sub> photoelectrode yielded lower levels of dye adsorption ( $5.84 \times 10^{-8}$  mol mg<sup>-1</sup>) on the TiO<sub>2</sub> surface, representing 93.9% of the R-TiO<sub>2</sub> photoelectrode capacity. The lower dye adsorption on the RS-TiO<sub>2</sub> surfaces indicated that small numbers of anchoring groups on the RS-TiO<sub>2</sub> surface were blocked by SA during the adsorption process. Also, this result coincided with a lower photocurrent density in the RS-TiO<sub>2</sub> devices. We concluded that the slightly lower photocurrent density within the RS-TiO<sub>2</sub> photoelectrode resulted from lower dye loading levels induced by a competitive adsorption reaction between N719 and SA.

The long-term stability of the RS-TiO<sub>2</sub> photoelectrodes at 60°C under illumination of 100 mW cm<sup>-2</sup> is plotted in Figure 3.5 and Table 3.1. Although the RS-TiO<sub>2</sub> cells showed slightly lower PCE than the R-TiO<sub>2</sub> cells during the initial stages of the measurement, the PCE of RS-TiO<sub>2</sub> cells was as much stable as that of H-TiO<sub>2</sub> cells. Even the RS-TiO<sub>2</sub> devices displayed higher PCE than the R-TiO<sub>2</sub> cells after 100 h. The RS-TiO<sub>2</sub> photoelectrode aged for 400 h showed a  $J_{SC}$  of 8.48 mA cm<sup>-2</sup>, a  $V_{OC}$  of 0.765 V, a FF of 0.71, and PCE of 4.61%, 79.1% of its initial efficiency. After 1000 h, a PCE of 4.08% was obtained from the RS-TiO<sub>2</sub> device, which was 70.1% of its initial efficiency. We expected that the enhanced long-term stability of the RS-TiO<sub>2</sub> devices arose from the superior anchoring properties of the N719 molecules on the RS-TiO<sub>2</sub> surfaces. The amounts of dye molecules adsorbed on the RS-TiO<sub>2</sub> surface were measured using UV-vis spectroscopy as function of aging time, as shown in Figure 3.4(b) and Table 3.2. Surprisingly, the adsorbed dyes on RS-TiO<sub>2</sub> photoelectrode were as stable as those on H-TiO<sub>2</sub> photoelectrode. The amount of adsorbed dye molecules on the RS-TiO<sub>2</sub> surface after aging for 400 h and 1000 h was  $5.08 \times 10^{-8}$  mol mg<sup>-1</sup> ( $D_{400}$ ) and  $4.49 \times 10^{-8}$  mol mg<sup>-1</sup> ( $D_{1000}$ ), 87.0% ( $D_{400}/D_0$ ) and 76.9% ( $D_{1000}/D_0$ ) of initial amount of adsorbed dye on RS-TiO<sub>2</sub> surface, respectively. This significantly reduced amount of

dye molecules desorbed from the RS-TiO<sub>2</sub> surface was confirmed by photograph images, as shown in Figure 3.6. The superior long-term stability of the RS-TiO<sub>2</sub> cells supported the notion that modifying the adsorption process by introducing SA could retard desorption of N719 dyes from the RS-TiO<sub>2</sub> photoelectrode. This result suggested that the amount of weakly bound N719 molecules on the RS-TiO<sub>2</sub> photoelectrode could be decreased to the levels observed on the H-TiO<sub>2</sub> photoelectrode. The binding mode of N719 on the RS-TiO<sub>2</sub> surface was investigated using ATR FT-IR methods and is plotted in Figure 3.7. As discussed above, the intensity at 1730 cm<sup>-1</sup>, as shown in Figure 3.7, corresponded to the amounts of N719 molecules weakly bound via only one covalent bond, with anchoring groups on the TiO<sub>2</sub> surfaces. The absorption intensity at 1730 cm<sup>-1</sup> for the RS-TiO<sub>2</sub> photoelectrode was as weak as that of the H-TiO<sub>2</sub> photoelectrode. This was in a good agreement with previous dye desorption experiments and long-term stability measurements. This result confirmed that the amount of weakly bound N719 molecules on the RS-TiO<sub>2</sub> surface could be reduced to a level comparable to the amount of weakly bound N719 molecules on the H-TiO<sub>2</sub> surface.

### **3.3.5 Stabilized binding mode of N719 dye by addition of SA**

The amounts N719 molecules that were weakly anchored due to the large number of OH groups on the TiO<sub>2</sub> surface were measured through dye desorption experiments and ATR-FTIR measurements. Based on our experimental results, including the ATR-FTIR and UV-vis spectroscopy data, we propose that the anchoring modes of N719 dye molecules on H-TiO<sub>2</sub>, R-TiO<sub>2</sub>, and RS-TiO<sub>2</sub> photoelectrodes are as shown in Figure 3.8. A larger number of surface OH group anchoring sites on R-TiO<sub>2</sub> increased the N719 dye loading levels on the R-TiO<sub>2</sub> photoelectrode; however, large amounts of N719 dye molecules tended to anchor onto the R-TiO<sub>2</sub> surface through only one covalent bond due to the rapid adsorption of N719 dyes in the presence of large amount of OH groups on the R-TiO<sub>2</sub> photoelectrode. Unlike the R-TiO<sub>2</sub> photoelectrodes, the H-TiO<sub>2</sub> photoelectrode displayed a lower concentration of surface OH anchoring groups after introduction of a high-temperature thermal sintering process. The smaller number of anchoring groups slowed the adsorption rate of N719 dyes onto the H-TiO<sub>2</sub> surface, which increased the amounts of strongly bound N719 molecules, that is, N719 dye molecules bound to the H-TiO<sub>2</sub> surface through two

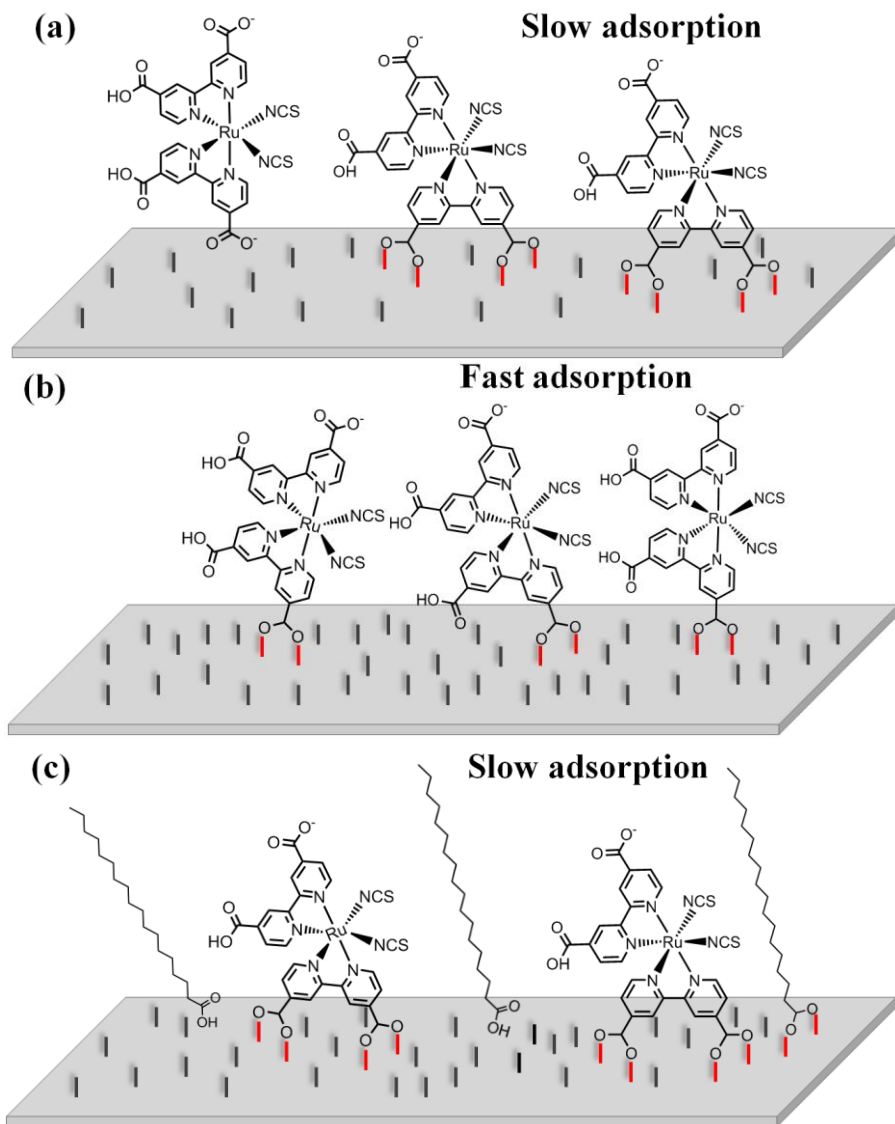


**Figure 3.8** Plausible binding mode of N719 on (a) H-TiO<sub>2</sub> surface, (b) R-TiO<sub>2</sub>, and (c) RS-TiO<sub>2</sub> surface

covalent bonds. N719 dye molecules adsorbed to the RS-TiO<sub>2</sub> photoelectrode surface at a slower rate due to the competitive binding of SA molecules to the OH groups during the sensitization process. Although competitive adsorption of N719 and SA molecules reduced the N719 dye loading on the RS-TiO<sub>2</sub> surfaces, the strong adsorption of N719 dyes on the TiO<sub>2</sub> photoelectrodes, via two carboxylate groups within the N719 molecules, was promoted. Therefore, the RS-TiO<sub>2</sub> devices showed enhanced resistance to detachment of the bound dye molecules from the OH-rich TiO<sub>2</sub> surface. These devices also exhibited improved long-term stability properties.

### **3.4 Conclusion**

In conclusion, we analyzed the relationship between the binding mode of N719 and the long-term stability using room-temperature fabricated TiO<sub>2</sub> photoelectrodes. The high-temperature sintered TiO<sub>2</sub> (H-TiO<sub>2</sub>) devices exhibited good stability after 1000 h (75.7% of its initial efficiency); however, the TiO<sub>2</sub> device fabricated at room temperatures (R-TiO<sub>2</sub>) exhibited poor long-term stability after 1000 h (34.8% of its initial

efficiency) due to the desorption of adsorbed N719 dye molecules from the R-TiO<sub>2</sub> surface. The binding modes of N719 molecules on the H-TiO<sub>2</sub> and R-TiO<sub>2</sub> photoelectrodes were analyzed by ATR-FTIR. The presence of excess surface OH groups on R-TiO<sub>2</sub> surface led to a large amount of weakly adsorbed N719 molecules on the TiO<sub>2</sub> surfaces. Dye desorption from the R-TiO<sub>2</sub> surfaces was prevented by modifying the N719 anchoring process through the addition of SA co-adsorbents to the dye solution (RS-TiO<sub>2</sub>). Although the total amounts of N719 molecules adsorbed onto the RS-TiO<sub>2</sub> surface were slightly reduced due to the competitive anchoring process between the SA and N719 dye molecules, the slow adsorption of N719 molecules increased the amounts of strongly anchored N719 on the RS-TiO<sub>2</sub> surface. The RS-TiO<sub>2</sub> device yielded a stable performance after 1000 h (70.1% of its initial efficiency). This result provides a new approach to developing long-term stable DSSCs fabricated under low-temperature/ambient conditions. We are currently systematically analyzing the effects of the binding mode on the electron injection properties.

### **3.5 References**

- [1] B. O'regan, M. Grätzel, *Nature* **1991**, 353, 737
- [2] Z. Wang, H. Wang, B. Liu, W. Qiu, J. Zhang, S. Ran, H. Huang, J. Xu, H. Han, D. Chen, G. Shen, *ACS Nano* **2011**, 5 8412
- [3] Y. Kijitori, M. Ikegami, T. Miyasaka, *Chem.Lett.* 2007, 190
- [4] M. Toivola, J. Halme, K. Miettunen, K. Aitola, P. D. Lund, *Int. J. Energy. Res.* **2009**, 33 1145
- [5] T. Yamaguchi, N. Tobe, D. Matsumoto, T. Nagai, H. Arakawa, *Sol. Energy Mater. Sol. Cells* **2010**, 94, 812
- [6] L.-C. Chen, J.-M. Ting, Y.-L. Lee, M.-H Hon, *J. Mater. Chem.* **2012**, 22, 5596
- [7] K.-M. Lee, S.-J. Wu, C.-Y. Chen, C.-G. Wu, M. Ikegami, K. Miyoshi, T. Miyasaka, K.-C. Ho, *J. Mater. Chem.* **2009**, 19, 5009
- [8] C.-R. Ke, L.-C. Chen J.-M. Ting, *J. Phys. Chem. C*, **2012**, 116, 2600
- [9] Y. Han, J. M. Pringle, Y.-B. Cheng, *RSC Advances*, 2014, 4, 1393
- [10] F. Huang, D. Chen, Y. Chen, R. A. Caruso, Y.-B. Cheng, *J. Mater. Chem. C*, **2014**, 2, 1284

- [11] J. Lin Y. Peng, A.R. Pascoe, F. Huang, Y.B. Cheng, Y.-U. Heo, A. Nattestad, W. Seung, S.K. Kim, H.J. Yoon, S.W. Kim, Y. Yamauchi, S.X. Dou, J.H. Kim, *J. Mater. Chem. A*, **2015**, 3, 4679
- [12] N.-G. Park, K. M. Kim, M. G. Kang, K. S. Ryu, S. H. Chang, Y. J. Shin, *Adv. Mater.* **2005**, 17, 2349
- [13] D. Zhang, T. Yoshida, K. Furuta, H. Minoura, *J. Photochem. Photobiol. A: Chem.* **2004**, 164, 159
- [14] D. Zhang, T. Yoshida, H. Minoura, *Adv. Mater.* **2003**, 15, 814
- [15] X. Li, H. Lin, J. Li, N. Wang, C. Lin, L. Zhang, *J. Photochem. Photobiol. A: Chem.* **2008**, 195, 247
- [16] K. Kim, G.-W. Lee, K. Yoo, D. Y. Kim, J.-K. Kim, N.-G Park, *J. Photochem. Photobiol. A: Chem.* **2009**, 204, 144
- [17] M. Dürr, A. Schmid, M. Obermaier, S. Rosselli, A. Yasuda, G. Nelles, *Nat. Mater.* **2005**, 4, 607
- [18] J.-H. Yum, S.-S. Kim, D.-Y. Kim, Y.-E. Sung, *J. Photochem. Photobiol. A: Chem.* **2005**, 173, 1

- [19] L. Grinis, S. Kotlyar, S. Rühle, J. Grinblat, A.Zaban, *Adv. Funct. Mater.* **2010**, 20, 282
- [20] H.-W. Chen, C.-P. Liang, H.-S. Huang, J.-G. Chen, R. Vittal, C.-Y. Lin, K.C.W. Wu, K.-C. Ho, *Chem. Commun.* **2011**, 47, 8346
- [21] F. Shao, J. Sun, L. Gao, J. Chen, S. Yang, *RSC Advances* **2014**, 4, 7805
- [22] S. Uchida, M. Tomiha, N. Masaki, A. Miyazawa, H. Takizawa, *Sol. Energy Mater. Sol. Cells* **2004**, 81, 135
- [23] S. Uchida, M. Tomiha, H. Takizawa, M. Kawaraya, *J. Photochem. Photobiol. A: Chem.* **2004**, 164, 93
- [24] L. Ming, H. Yang, W. Zhang, X. Zeng, D. Xiong, Z. Xu, H. Wang, W. Chen, X. Xu, M. Wang, J. Duan, Y.-B. Cheng, J. Zhang, Q. Bao, Z. Wei, S. Yang, *J. Mater. Chem. A*, **2014**, 2, 4566
- [25] M. Fujimoto, T. Kado, W. Takashima, K. Kaneto, S. Hayase, *J. Electro-chem.Soc.* **2006**, 153, A826
- [26] X. Li, Y. Zhang, Z. Zhang, J. Zhou, J. Song, B. Lu, E. Xie, W. Lan, *J. Power Sources*, **2011**, 196, 1639

- [27] X.-L. He, G.-J. Yang, C.-J. Li, C.-X. Li, S.-Q. Fan, *J. Power Sources*, **2014**, 251, 122
- [28] Y. Bai, Y. Cao, J. Zhang, M. Wang, R. Li, P. Wang, S.M. Zakeeruddin, M. Grätzel, *Nat. Mater.* 2085, 7, 626
- [29] J. N. Freitas, A. F. Nogueira, M.D. Paoli, *J. Mater. Chem.* **2009**, 19, 5279
- [30] P. Wang, C. Klein, J.-E. Moser, R.H.-Baker, N.-L. Cevey-Ha, R. Charvet, P. Comte, S.M. Zakeeruddin, M. Grätzel, *J. Phys. Chem. B* **2004**, 108, 17553
- [31] C. Baik, D. Kim, M.S. Kang, S.O. Kang, J. Ko, M.K. Nazeeruddin, M. Grätzel, *J. Photochem. Photobiol. A: Chem.* **2009**, 201, 168
- [32] Z. Zhang, S.M. Zakeeruddin, B.C. O'Regan, R. Humphry-Baker, M. Grätzel, *J. Phys. Chem. B* **2009**, 109, 2163
- [33] M. Wang, C. Grätzel, S.J. Moon, R. Humphry-Baker, N. Rossier-Iten, S.M. Zakeeruddin, M. Grätzel, *Adv. Funct. Mater.* **2009**, 19, 2163
- [34] F. Nüesch, L. J. Rothberg, E. W. Forsythe, Q. T. Le, Y. Gao, *Appl. Phys. Lett.* **1999**, 74, 880

- [35] S. Gardonio, L. Gregoratti, D. Scaini, C. Castellarin-Cudia, P. Dudin, P. Melpignano, V. Biondo, R. Zamboni, S. Caria, M. Kiskinova, *Org. Electron.* **2008**, 9, 253
- [36] M. Ikegami, J. Suzuki, K. Teshima, M. Kawaraya, T. Miyasaka, *Sol. Energy Mater. Sol. Cells* **2009**, 93, 836
- [37] K.-M. Lee, W.-H. Chiu, M.-D. Lu, W.-F. Hsieh, *J. Power Sources* **2011**, 196, 8897
- [38] H. Lee, D. Hwang, S. M. Jo, D. Kim, Y. Seo, D. Y. Kim, *ACS Appl. Mater. Interfaces* **2012**, 4, 3308
- [39] D. Hwang, H. Lee, S.-Y. Jang, S. M. Jo, D. Kim, Y. Seo, D. Y. Kim, *ACS Appl. Mater. Interfaces* **2011**, 3, 2719
- [40] J. Lim, Y. S. Kwon, S.-H. Park, I. Y. Song, J. Choi, T. Park, *Langmuir* **2011**, 27, 14647
- [41] D. Zhang, J. A. Downing, F. J. Knorr, J. L. McHale, *J. Phys. Chem. B* **2006**, 110, 21890
- [42] K. S. Finnie, J. R. Bartlett, J. L. Woolfrey, *Langmuir* **1998**, 14, 2744

- [43] M. K. Nazeeruddin, R. Humphry-Baker, P. Liska, M. Grätzel, *J. Phys. Chem. B* **2003**, 107, 8981
- [44] C. Pérez León, L. Kador, B. Peng and M. Thelakkat, *J. Phys. Chem. B* **2006**, 110, 8723
- [45] K. E. Lee, M. A. Gomez, S. Elouatik, G. P. Demopoulos, *Langmuir* **2010**, 26, 9575
- [46] V. Shklover, Y. E. Ovchinnikov, L. S. Braginsky, S. M. Zakeeruddin, M. Grätzel, *Chem. Mater.* **1998**, 10, 2533
- [47] F. Hirose, K. Kuribayashi, T. Suzuki, Y. Narita, Y. Kimura, M. Niwano, *Electrochem. Solid-State Lett.* **2008**, 11, A109
- [48] K. Kuribayashi, H. Iwata, F. Hirose, *ECS Transactions*, **2007**, 6, 15
- [49] J. Wang, Z. Lin, *Chem. Mater.* **2009**, 22, 579
- [50] K. Kilså, E. I. Mayo, B. S. Brunshwig, H. B. Gray, N. S. Lewis, J. R. Winkler, *J. Phys. Chem. B* **2004**, 108, 15640
- [51] T. Luitel, F. P. Zamborini, *Langmuir* **2013**, 29, 13582

[52] J. Singh, A. Gusain, V. Saxena, A. K. Chauhan, P. Veerender, S. P. Koiry, P. Jha, A. Jain, D. K. Aswal, S. K. Gupta, *J. Phys. Chem. C* **2013**, 117, 21096

## Chapter 4

### Highly efficient photon harvesting by co-sensitization for flexible dye-sensitized solar cells

#### 4.1 Introduction

In the past few year, dye-sensitized solar cells (DSSCs) made from nanocrystalline  $\text{TiO}_2$  electrode have gained much attention and been investigated as a promising, cost-effective renewable energy harvester. [1-4] Although the highest efficiency of DSSC has been obtained with rigid glass-based DSSCs using high-temperature sintered  $\text{TiO}_2$  film, plastic substrate-based flexible DSSCs have been subjected of recent study.[5-10] In general, plastic substrate-based flexible DSSCs were fabricated under low-temperature condition due to thermal instability of polymeric substrate. This low-temperature process results in absence of particle necking between  $\text{TiO}_2$  particles and poor conversion efficiency. So far, many alternative methods have been developed, including the transfer of  $\text{TiO}_2$  layers,[11] doctor blading of titania paste,[12-18] electrophoretic deposition,[19-21] spray-deposition,[22-24] mechanical compression,[12,13] chemical sintering, [16,17,25] and microwave sintering. [26]

We recently reported electrospray method for the fabrication flexible TiO<sub>2</sub> photoelectrode with 0-D hierarchically structured TiO<sub>2</sub> (HS-TiO<sub>2</sub>) on conductive substrate.[27] In the HS-TiO<sub>2</sub> structure, the electron transport was improved compared to non-HS ones. The HS-TiO<sub>2</sub>s were coated onto a flexible substrate using a binder-free dispersion of commercially available TiO<sub>2</sub> nanocrystalline powders (P25, Degussa). Also, we introduced additional mechanical compression and titanium n-tetrabutoxide (TTB) treatment in order to improve interparticle connectivity.[28] The resulting post-treated flexible TiO<sub>2</sub> electrode with Ru-sensitizer (N719) displayed an efficiency of 5.57% under 1 sun illumination (100 mW cm<sup>-2</sup>). Although the introduced processes is effective approach for flexible DSSCs, the combination of Ruthenium sensitizer and low-temperature fabricated electrode is still questionable because of following limitation: 1) TiO<sub>2</sub> electrode should be thin because of poor charge transport properties, and 2) molar extinction coefficient of Ruthenium sensitizer is not high as much as metal-free organic sensitizer. In general, DSSCs based on Ruthenium complex sensitizer yield maximum efficiency with use of a thick TiO<sub>2</sub> film (>15 μm) because of molar extinction coefficient being lower than 20,000 M<sup>-1</sup> cm<sup>-1</sup> due to metal-ligand charge transfer excitation.[29] To overcome this limitation, metal-free organic sensitizer with high molar extinction

coefficient was used for light absorber on TiO<sub>2</sub> electrode.[30-33] Compared with Ru-sensitizer, organic sensitizer generally has higher molar extinction coefficients. This high molar extinction coefficient of organic sensitizer enables thinner TiO<sub>2</sub> film and makes minimize charge recombination. However, the narrow absorption spectrum of organic sensitizer weakens the light harvesting efficiency. Therefore, the co-sensitization of organic dyes, which responses complementary light absorption, has been regard as effective strategy for broadening of light harvesting property. Several groups have demonstrated the co-sensitization of TiO<sub>2</sub> with combination of mixed dye solution for high-temperature sintered TiO<sub>2</sub> electrode.[34-36] Kuang et al. investigated co-sensitized TiO<sub>2</sub> electrode with SQ2 and JK2 sensitizer and obtained an efficiency of 6.4%, which is higher than those achieved from individual sensitizer.[34] Yella et al. used zinc porphyrin dye of YD2-o-C8 and organic dye of Y123. Co-sensitization of YD2-o-C8 with Y123 dye further enhances the performance of the device, leading to a measured conversion efficiency of 12.3% under simulated AM 1.5G sunlight.[35] Huang et al. fabricated flexible DSSCs containing multiple dyes in discrete layers. Two different dyes, N719 and GD3, have been adsorbed onto two separate layers of TiO<sub>2</sub> on plastic substrates. This electrode gave more intense absorption than the single N719 or GD3 electrode, and hence

resulted in a much improved conversion efficiency of 4.9%. [36]

In this study, metal-free organic sensitizer synthesized in our group (JH-1) and unsymmetrical squaraine dye (SQ2) were used for co-sensitization of flexible TiO<sub>2</sub> electrode. The JH-1 sensitizer has a molar extinction coefficient of 50,000 M<sup>-1</sup> cm<sup>-1</sup>, and showed absorption range of 400 nm to 550 nm in ethanol solution. The best efficiency of 9.18% under 1 Sun illumination was achieved with HS-TiO<sub>2</sub> photoelectrode by the resonant multiple light scattering.[37] The SQ2 dye reported by Geiger et al. is another highly efficient organic dye, with a molar extinction coefficient of 319,000 M<sup>-1</sup> cm<sup>-1</sup> and exhibited an absorption range of 550 nm to 700 nm in DMF solution, which is complementary absorption for JH-1 sensitizer.[38] The absorption properties and photovoltaic parameters of co-sensitized flexible TiO<sub>2</sub> electrode were investigated by controlling the molar ratio of mixed dye solution.

## 4.2 Experimental

### 4.2.1 Materials

Fluorine-doped tin oxide (FTO) glass (TEC-8, Pilkington) and Indium–tin-oxide (ITO)-coated polyethylene naphthalate (PEN) (Pecell, sheet resistance 13  $\Omega$ /sq, 200  $\mu$ m) were used as a transparent conducting substrate. A Pt/Ti-sputtered PEN film (Pecell, sheet resistance 5  $\Omega$ /sq) was used as a counter electrode in the flexible DSSCs. The nanocrystalline P25 powder was purchased from Degussa and used to prepare a TiO<sub>2</sub> dispersion for electrospray processing. An organic sensitizer (JH-1) was synthesized according to our previous report. [R] Squaraine sensitizer (SQ2) was purchased from Solaronix. Iodine (I<sub>2</sub>, 99.99+%, Aldrich), 4-*tert*-butylpyridine (TBP, 99%, Aldrich), Guanidium thiocyanate (GSCN, 99.9%, Aldrich), 1-butyl-3-methylimidazolium iodide (BMII, 99%, C-tri), acetonitrile (ACN, 99.8%, Aldrich), valeronitrile (VN, 99.5%, Aldrich), and Deoxycholic acid (DCA, 99.5%, Fluka) were used as purchased without further purification.

#### **4.2.2 Preparation of the HS-TiO<sub>2</sub> Electrode**

The hierarchically structured mesoporous TiO<sub>2</sub> photoelectrodes were prepared according to the reported procedure. [R] The 10% (wt/v) P25 (Degussa) was dispersed in anhydrous ethanol using an ultra apex mill

(Model UAM-015, Kotobuki). The stabilized P25 dispersion was loaded into a plastic syringe infusion pump (KD Scientific Model 220) connected to a high-voltage power supply (Bertan Series 205B). The solution was then electro sprayed directly onto the conducting FTO glass or ITO-PEN substrate. An electric field of  $1.5 \text{ kV cm}^{-1}$  was applied between the metal orifice and the conducting substrate with a feed rate of  $40 \text{ }\mu\text{L min}^{-1}$ . A motion control system governed by a microprocessor (Dasa Tech) was used to control the nozzle and substrate during deposition to produce a uniformly thick film over a large area.

### **4.2.3 Device Fabrication**

After electro spray processing, the as-sprayed  $\text{TiO}_2$  photoelectrode was pressed for 10 min with a pressures of 10 MPa. The as-pressed photoelectrode was then immersed in a 0.3 mM JH-1 or SQ2 and 1.5 mM DCA ethanol solution for 24 h at room temperature to produce the flexible DSSCs. High-temperature sintered  $\text{TiO}_2$  electrodes for conventional glass-substrate DSSCs were prepared by sintering the as-pressed  $\text{TiO}_2$  photoelectrodes at  $500^\circ\text{C}$  for 30 min under ambient air. After cooling to room temperature, the  $\text{TiO}_2$  electrodes were immersed in a 0.3 mM dye

solution for 24 h at room temperature. After 24 h, the immersed TiO<sub>2</sub> electrodes were rinsed with anhydrous ethanol and dried under a nitrogen flow. A Pt counter electrode for conventional glass-based DSSCs was prepared by drop-casting 5 mM H<sub>2</sub>PtCl<sub>6</sub> in isopropyl alcohol onto the washed FTO glass, followed by sintering at 400°C for 20 min. The dye-sensitized TiO<sub>2</sub> and Pt electrodes were assembled and sealed carefully using a thermal adhesive film (Surlyn, DuPont 1702, 60 μm thick) as a spacer to fabricate sandwich-type cells. The active area of a cell was typically 0.25 cm<sup>2</sup>. The liquid electrolyte consisted of 0.65 M 1-butyl-3-methylimidazolium (BMII), 0.03 M iodine (I<sub>2</sub>), 0.1 M lithium iodide (LiI), and 0.5 M 4-*tert*-butylpyridine (TBP) in a mixture of acetonitrile (ACN) and valeronitrile (VN) (85/15 v/v). An electrolyte solution was injected through a pre-drilled hole in the counter electrode. Finally, the pre-drilled holes were sealed using a thermal adhesive film and cover glass.

#### **4.2.4 Amount of adsorbed dye measurement**

The quantities of adsorbed dye present on the TiO<sub>2</sub> surfaces were measured by UV-Vis spectroscopy. The amount of dye adsorbed onto a TiO<sub>2</sub> surface was determined by immersing the dye-sensitized TiO<sub>2</sub> electrode in a

0.02 M KOH ethanol or 2-methoxyethanol solution, and the absorbance of the resulting solution was measured. The absorption spectra of the dye-dissolved solutions were measured using a UV-Vis spectrophotometer (Agilent 8453).

#### **4.2.5 Characterization of the DSSCs**

Photovoltaic measurements of the DSSCs were conducted using an AM 1.5 solar simulator and a 450 W Xe lamp. The intensity of the simulated light was calibrated using a Si reference solar cell to yield AM 1.5 global irradiation. The photovoltaic characteristics of the DSSC were obtained by applying an external potential bias to the cells and by measuring the photocurrent generated using a Keithley model 2400 source meter. The electron transport time and electron recombination lifetime were measured using intensity-modulated photocurrent spectroscopy (IMPS) and intensity-modulated photovoltage spectroscopy (IMVS). A diode laser with variable power and modulation control (Coherent Lab-laser, 40 mW, 446 nm) was used as the light source. The illumination was always applied incident to the working electrode side of the solar cell. The light intensity was measured using a calibrated Si photodiode. IMVS was performed under open-circuit

conditions. The output of the solar cell was connected directly to a frequency response analyzer (Schlumberger–Solartron SI 1260). IMPS measurements were performed by connecting the solar cell via a potentiostat amplifier (EG&G PAR 273) to the frequency response analyzer. During the IMPS and IMVS measurements, the cell was illuminated with sinusoidally modulated light having a small AC component (10% or less of the DC component). Long-term stability measurements were performed in a simulator at 60°C under illumination of 100 mW cm<sup>-2</sup>. A halogen lamp was used as the light source for the stability test. The temperature was controlled using a thermocouple and cooling fan in an adiabatic chamber.

## **4.3 Results and discussion**

### **4.3.1 Absorption spectra of mixed dye solution**

Before the optimize device performance, the optoelectrical characteristics of individual sensitizers were investigated. Figure 4.1 shows the molecular structures of novel organic sensitizer (JH-1, left) and unsymmetrical squaraine dye (SQ2, right) and the corresponding absorption

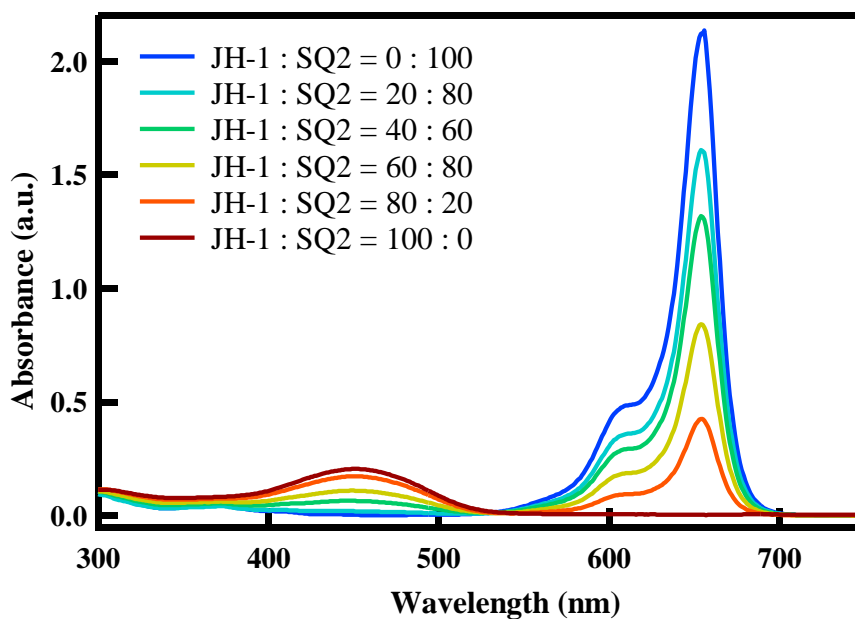
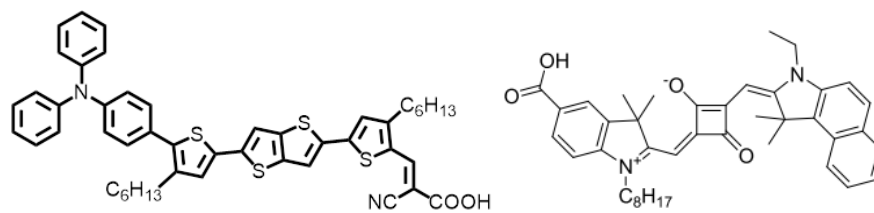


**Figure 4.1** Molecular structures of (a) JH-1, (b) SQ2, and (c) absorption spectra of mixed dye solution with different molar ratio in ethanol.

spectra at in ethanol. The absorption spectra of JH-1 sensitizer exhibit broad peak at the 450 nm in ethanol (red) due to the  $\pi$ - $\pi^*$  transitions of the conjugated molecule. On the other hand, the SQ2 sensitizer shows strong absorption band of the peak at 647 nm (blue) in ethanol. Obviously, the molar extinction coefficient of SQ2 squaraine sensitizer is extremely high ( $319,000 \text{ M}^{-1} \text{ cm}^{-1}$ ), compared to that of JH-1 organic sensitizer ( $50,000 \text{ M}^{-1} \text{ cm}^{-1}$ ) and N719 Ru-sensitizer ( $15,000 \text{ M}^{-1} \text{ cm}^{-1}$ ). This high molar absorption coefficient of dye enables using thin film of  $\text{TiO}_2$  for photoelectrode. In particular, this advantage is favorable for flexible DSSCs due to short diffusion length of low-temperature fabricated  $\text{TiO}_2$  photoelectrode.

Also, the absorption spectra of mixed dye solution at different molar ratio are investigated. Apparently, it can be seen that the mixed dye solution exhibited the same absorption characteristics as the individual JH-1 and SQ2 sensitizer. (Figure 4.1(c)) With increasing molar ratio of JH-1 dye, the light absorption from 400 nm to 550 nm increases and that from 550 nm to 700 nm decrease simultaneously. On the contrary, the light absorption from 550 nm to 700 nm increases with the increasing molar ratio of SQ2 in the solution, and decreased simultaneously in the light absorption from 400 nm to 550 nm. From this UV-absorption result, it is concluded that the light absorption of JH-1 and SQ2 sensitizers are independent and complementary.

### 4.3.2 Absorption spectra of co-sensitized TiO<sub>2</sub> films

The mixed dye solutions with different molar ratios of 10:0, 8:2, 6:4, 4:6, 2:8 and 0:10 were used for co-sensitized TiO<sub>2</sub> films. Figure 4.2 shows photograph image and absorption spectra of mixed dye-sensitized TiO<sub>2</sub> films. As we can see in Figure 4.2, the color of dye-sensitized TiO<sub>2</sub> film with different co-sensitizing condition changed gradually. However, the appearance of absorption spectra of dye-sensitized TiO<sub>2</sub> film is different from those of solution. The JH-1 sensitized TiO<sub>2</sub> film and SQ2 sensitized TiO<sub>2</sub> film showed absorption wavelength around 350 nm ~ 600 nm and 550 nm ~ 720 nm, respectively. This broadening phenomenon that is commonly observed in the spectral responses organic sensitizers with carboxylic acid groups adsorbed on TiO<sub>2</sub> surface. [37] The difference of absorbance between JH-1-sensitized TiO<sub>2</sub> film and SQ2-sensitized TiO<sub>2</sub> film is reduced after dye sensitization. This observation may result from different amount of adsorbed dye onto TiO<sub>2</sub> surface. Also, it is interesting that absorption intensity of JH-1-sensitized TiO<sub>2</sub> film is inconsistent with concentration of JH-1 dye solution. Therefore, we calculated amount of adsorbed dye on mixed dye-sensitized TiO<sub>2</sub> film in order to quantify analysis. Upon dipping the co-sensitized TiO<sub>2</sub> films for 10 min into a 0.02 M KOH ethanol solution,

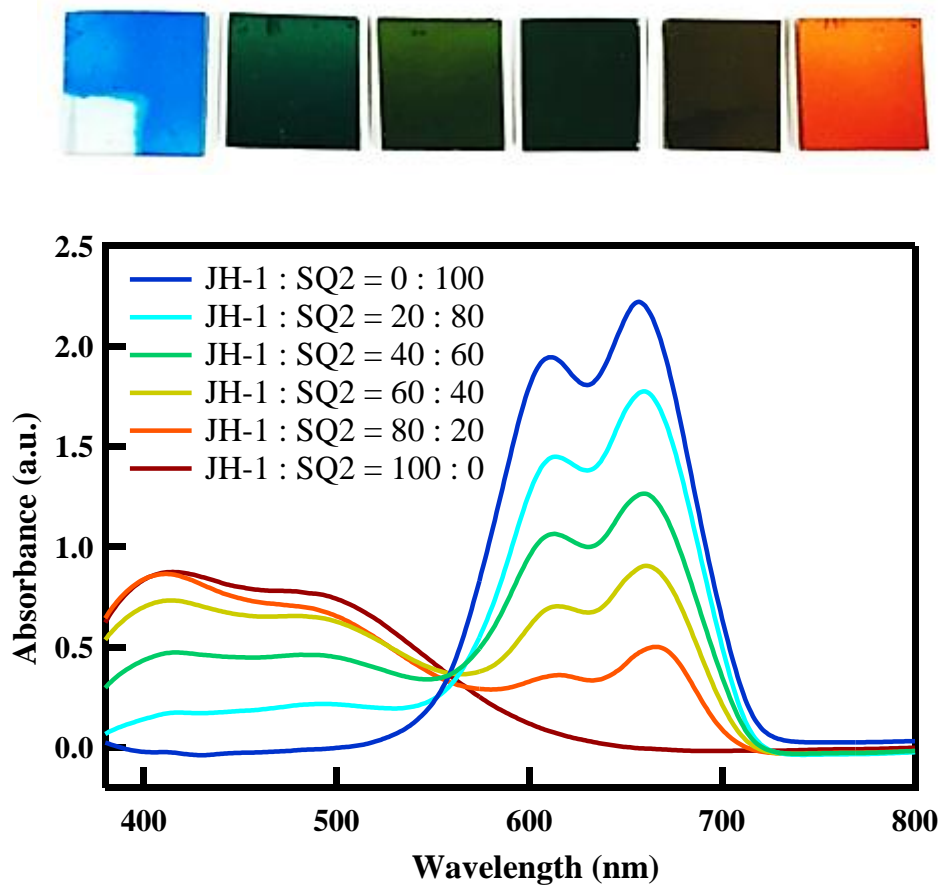


**Figure 4.2** (a) Photograph images and (b) absorption spectra of co-sensitized TiO<sub>2</sub> films with different cocktail dye solution.

only SQ2 dye dissolves from TiO<sub>2</sub> electrode. After washing the electrode, the residual JH-1 sensitizer on TiO<sub>2</sub> film was sequentially desorbed in 0.02 M KOH/2-Methoxyethanol solution. The amount of desorbed dye was calculated by measuring the UV absorption spectra of dissolved solution from co-sensitized TiO<sub>2</sub> film. The calculated individual dye concentration on co-sensitized TiO<sub>2</sub> films as a function of dipping time was introduced in Figure 4.3. As the Figure 4.3 indicates, the SQ2 sensitizer showed saturated dye loading after around 4 h, which is faster than that at around 8 h for JH-1 sensitizer. Although the SQ2 sensitizer showed faster adsorption kinetics than JH-1 sensitizer, the saturation concentration of SQ2 is lower than JH-1 dye. The saturation amount of adsorbed dye for JH-1 dye and SQ2 dye are  $\sim 12.92 \times 10^{-8} \text{ mol mg}^{-1}$  and  $\sim 6.27 \times 10^{-8} \text{ mol mg}^{-1}$ , respectively. This result indicates that the SQ2 sensitizers occupy larger anchoring space on the TiO<sub>2</sub> surface. Not only the individual sensitizer, the amount of adsorbed dye on co-sensitized TiO<sub>2</sub> film was plotted as a function of molar ratio in Figure 4.4 and Table 4.1. The dye concentration of SQ2 sensitizer on TiO<sub>2</sub> films decreases linearly as molar ratio of SQ2 decreases. However, the dye concentration of JH-1 sensitizer showed non-linear characteristic. At the lower concentration of JH-1 sensitizer, the dye concentration of JH-1 increases proportionally, whereas the dye concentration of JH-1

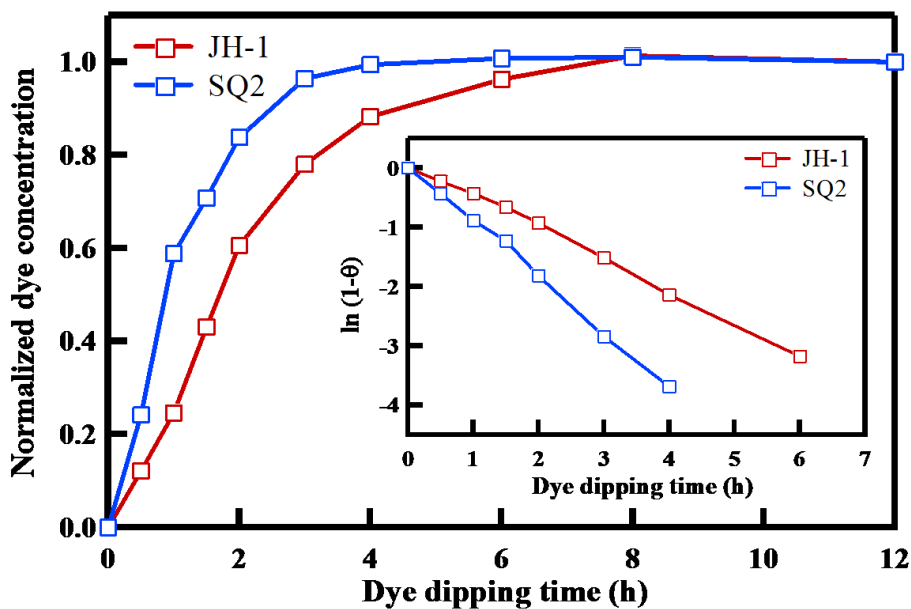


**Figure 4.3** Normalized dye concentrations onto the flexible  $\text{TiO}_2$  photoelectrode as a function of dipping times. The calculated values are the average of sample from three  $\text{TiO}_2$  electrodes. Inset plot is dye coverage ( $\theta$ ) versus adsorption time based on pseudo-first-reaction of each dye onto the flexible  $\text{TiO}_2$  photoelectrode.

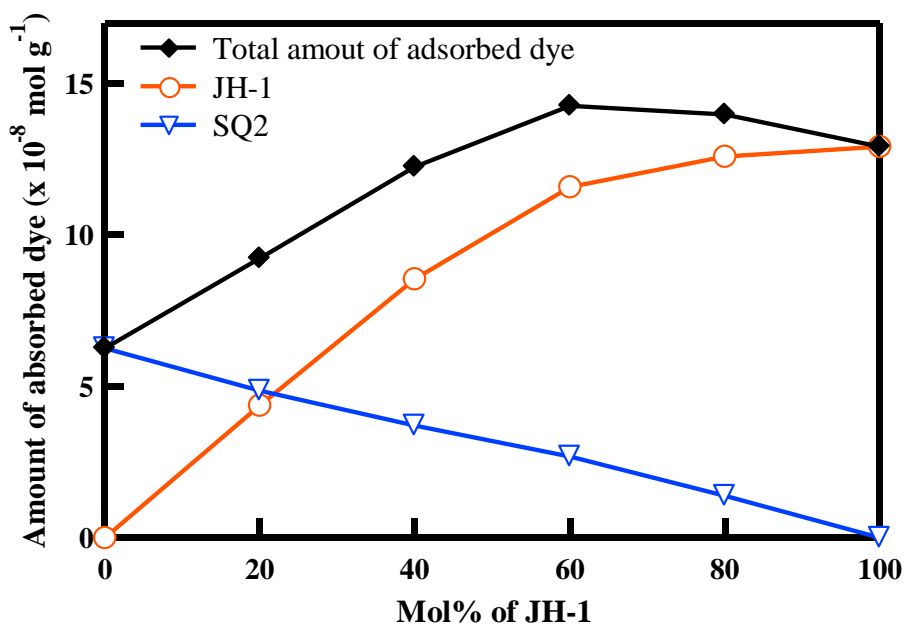


**Figure 4.4** Dye concentrations on flexible  $\text{TiO}_2$  film as a function of molar ratio in dye cocktail solution.

Dye	JH-1 : SQ2 0 : 100	JH-1 : SQ2 20 : 80	JH-1 : SQ2 40 : 60	JH-1 : SQ2 60 : 40	JH-1 : SQ2 80 : 20	JH-1 : SQ2 100 : 0
[C] <sub>JH-1</sub> (mol/mg)	0.00×10 <sup>-8</sup>	4.37×10 <sup>-8</sup>	8.55×10 <sup>-8</sup>	11.59×10 <sup>-8</sup>	12.60×10 <sup>-8</sup>	12.92×10 <sup>-8</sup>
[C] <sub>SQ2</sub> (mol/mg)	6.27×10 <sup>-8</sup>	4.86×10 <sup>-8</sup>	3.70×10 <sup>-8</sup>	2.68×10 <sup>-8</sup>	1.39×10 <sup>-8</sup>	0.00×10 <sup>-8</sup>
[C] <sub>TOTAL</sub> (mol/mg)	6.27×10 <sup>-8</sup>	9.23×10 <sup>-8</sup>	12.25×10 <sup>-8</sup>	14.27×10 <sup>-8</sup>	13.99×10 <sup>-8</sup>	12.92×10 <sup>-8</sup>

**Table 4.1** Concentration of individual dye loaded onto the flexible TiO<sub>2</sub> electrode for various molar ratio of dye cocktail solution.

increases slowly at the high molar ratio of JH-1 in mixed dye solution. For this trend of JH-1 sensitizer, the total amount of adsorbed dye on co-sensitized TiO<sub>2</sub> film at the molar ratio of 6/4 (JH-1/SQ2) showed increased to  $14.27 \times 10^{-8}$  mol mg<sup>-1</sup>, which is 110% of JH-1 only dye concentration. This improved total dye concentration on co-sensitized TiO<sub>2</sub> film come from insertion of small sized JH-1 into the space gap between SQ2 sensitizers. Consequently, we expected that the increased coverage of dye on TiO<sub>2</sub> surface facilitate enhanced photocurrent generation of co-sensitized TiO<sub>2</sub> electrode.

### 4.3.3 Photovoltaic characteristics of co-sensitized device

Figure 4.5 shows the photovoltaic performance of flexible DSSC sensitized with co-sensitizers and the photovoltaic parameters are listed in Table 4.2. The JH-1 sensitized device showed 5.1% of efficiency, whereas the SQ2 sensitized device showed 2.81% of efficiency. In spite of lower molar extinction coefficient of JH-1, the JH-1 sensitized device exhibited 70% higher  $J_{SC}$  (10.12 mA cm<sup>-2</sup>) than SQ2 sensitized device (5.92 mA cm<sup>-1</sup>) due

to broad light absorption and resonant multiple light scattering of JH-1 and hierarchically structured TiO<sub>2</sub> (HS-TiO<sub>2</sub>) aggregates. [37]

The co-sensitized DSSCs at the molar ratio of 8:2 and 6:4 (JH-1/SQ2) shows better performance compared to the JH-1 only sensitized DSSCs due to higher photocurrent density of these devices. According the Table 4.1 and Table 4.2, the total dye concentration these two devices is higher than that of JH-1 only device. Thus, we concluded that performance increase is mainly due to increased  $J_{SC}$ , which are highly related to the dye concentration and spectral response. We obtained the highest efficiency of 6.31%, where the molar ratio of 6:4 (JH-1/SQ2). The obtained  $V_{OC}$ ,  $J_{SC}$  and FF are 0.754 V, 12.32 mA cm<sup>-2</sup>, and 0.68, respectively. To investigate the spectral attribution of co-sensitized devices, incident photon to electron conversion efficiency (IPCE) spectra were measured. Figure 4.6 illustrated the IPCE spectra, which are sensitized by mixed dye solution. The maximum IPCE value of the individual JH-1 and SQ2 sensitized device reaches 58% at 460 nm and 40% at 670 nm, respectively. The value of IPCE spectra from JH-1 and SQ2 sensitized device are consistent with the  $J_{SC}$  value of these devices. In addition, the IPCE spectra range of device sensitized with JH-1 and SQ2 dye is in consistency with the range of light absorption of JH-1 and SQ dye-sensitized TiO<sub>2</sub> film.

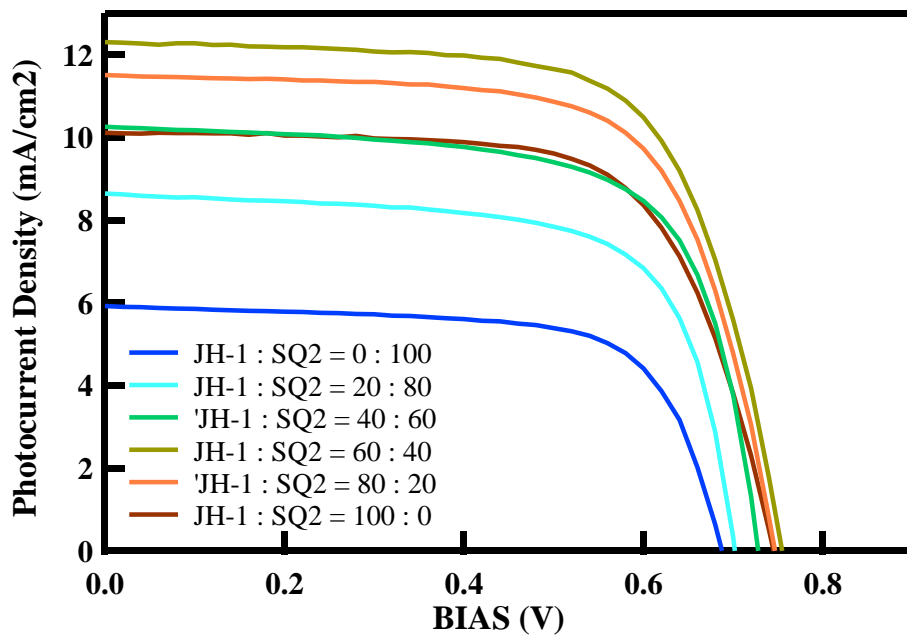


**Figure 4.5** J-V curves of the co-sensitized flexible DSSCs with different dye concentration.

Dye	V <sub>oc</sub> (V)	J <sub>sc</sub> (mA cm <sup>-2</sup> )	FF	EFF (%)
JH-1 : SQ2 = 0 : 100	0.688	5.92	0.69	2.81
JH-1 : SQ2 = 20 : 80	0.702	8.65	0.686	4.16
JH-1 : SQ2 = 40 : 60	0.728	10.27	0.68	5.08
JH-1 : SQ2 = 60 : 40	0.754	12.32	0.68	6.31
JH-1 : SQ2 = 80 : 20	0.748	11.52	0.682	5.87
JH-1 : SQ2 = 100 : 0	0.745	10.12	0.676	5.1
N719	0.837	8.85	0.691	5.26

**Table 4.2** Photovoltaic parameters of the flexible DSSCs with different dye concentration.

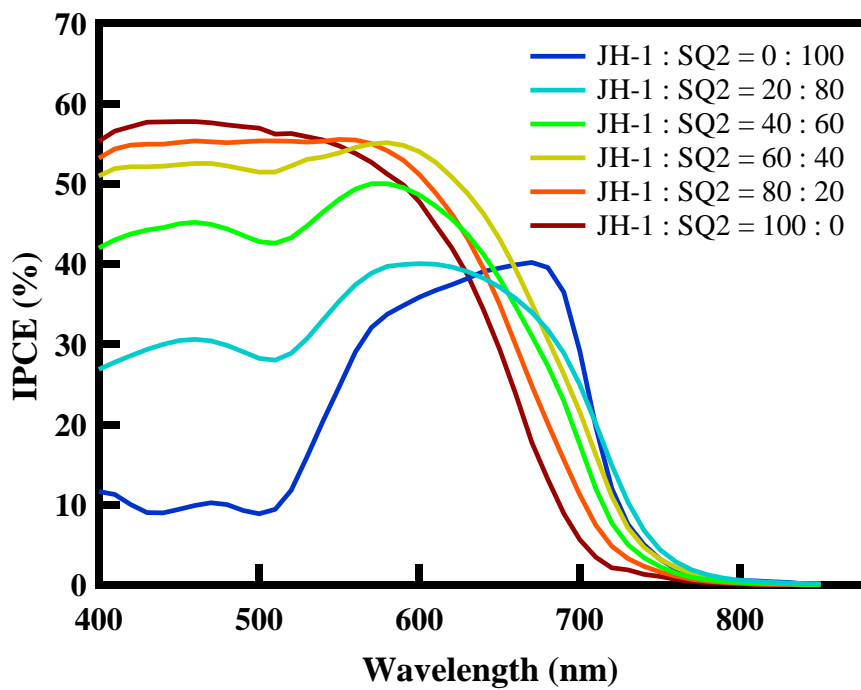
According to Figure 4.2, the spectrum response of JH-1 and SQ2 on TiO<sub>2</sub> surface is complementary to each other, so that the same phenomenon can be found for IPCE spectra. With increasing the molar ratio of SQ2 sensitizer in mixed dye solution, the IPCE spectrum shifts to the longer wavelength region and the IPCE value increases at the longer wavelength region. These spectral changes of co-sensitized device lead to higher photocurrent generation.

Figure 4.7 shows the calculated  $J_{SC}$  and measured  $J_{SC}$  with different dye concentration as a function of the dye molar ratio in the solution. The photocurrent density of DSSCs can be calculated using the IPCE spectrum (Equation 1)

$$J_{SC} = \int eIPCE(\lambda)I_S(\lambda)d\lambda \quad \text{Eq. 1}$$

Where  $e$ ,  $IPCE(\lambda)$ ,  $I_S(\lambda)$ , and  $\lambda$  are the electron charge, incident photon to current efficiency, incident photon flux density, and incident photon wavelength, respectively. The IPCE efficiency is the product of three quantum efficiencies, as expressed by Equation 2,

$$IPCE(\lambda) = \eta_{LHE} \times \eta_{INJ} \times \eta_{COL} \quad \text{Eq.2}$$



**Figure 4.6** The IPCE spectra of the co-sensitized flexible DSSCs with different dye concentration.

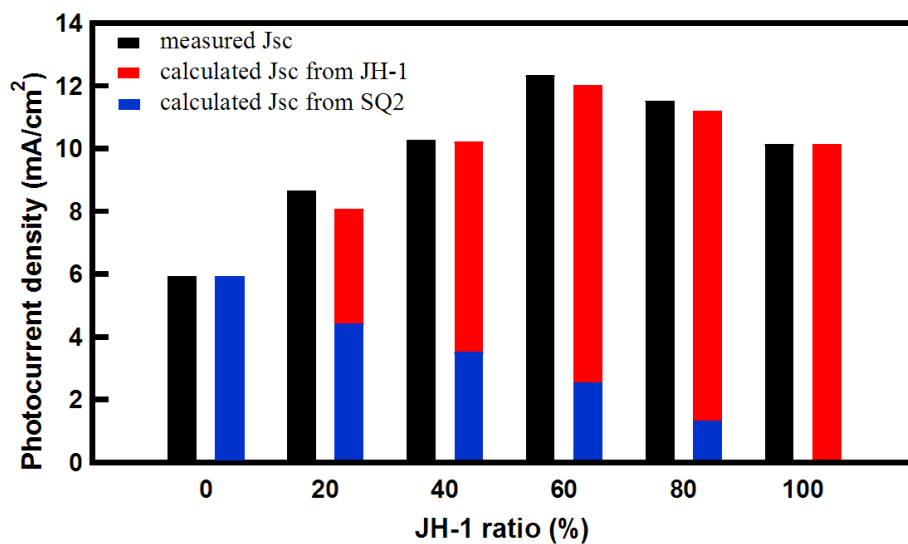


**Figure 4.7** Calculated photocurrent density with different dye concentration as a function of the dye molar ratio in the solution.

where  $\eta_{LHE}$ ,  $\eta_{INJ}$ , and  $\eta_{COL}$  are the light harvest efficiency, charge injection efficiency, and charge collection efficiency, respectively. The light harvesting, charge injection and charge collection efficiencies are related to the adsorbed dye concentration, the fraction of photons absorbed by the dye that are converted into conduction band electrons, and the degree of TiO<sub>2</sub> inter-particle connectivity. Therefore, the photocurrent density of device is directly proportional to the amount of adsorbed dye. Because we measured the amount of adsorbed dye on TiO<sub>2</sub> surface, the measured J<sub>SC</sub> could be expressed by sum of J<sub>SC</sub> from JH-1 and J<sub>SC</sub> from SQ2 dye. The measured J<sub>SC</sub> (left, black), calculated J<sub>SC</sub> from JH-1 (right, red) and SQ2 (right, blue) are shown in Figure 4.7. As shown in Figure 4.7, the difference between calculated J<sub>SC</sub> and measured J<sub>SC</sub> can be negligible and this result implies that the increased J<sub>SC</sub> by mixed dye solution results from not increased  $\eta_{INJ}$  and  $\eta_{COL}$ , but increased  $\eta_{LHE}$ . In other words, the increased J<sub>SC</sub> is mainly attributed to increased amount of adsorbed dye on TiO<sub>2</sub> surface.

Because of higher molar extinction coefficient of JH-1 and SQ2 sensitizer, optimal co-sensitized TiO<sub>2</sub> film thickness is expected to be shorter than Ru-sensitized TiO<sub>2</sub> film. In addition, the charge transport properties of low-temperature fabricated flexible TiO<sub>2</sub> film is much differ from high temperature fabricated rigid TiO<sub>2</sub> films. Therefore, it is worthy to

investigate the optimal thickness of co-sensitization on flexible TiO<sub>2</sub> electrode. Figure 4.8(a) and 4.8(b) shows the dependence of J<sub>SC</sub> and conversion efficiency on flexible TiO<sub>2</sub> film thickness and J-V characteristics of mixed dye-sensitized and N719 sensitized devices. All TiO<sub>2</sub> electrodes in Figure 4.8(a) were co-sensitized by the mixed dye solution of 6:4 (JH-1/SQ2) for 24 h. The J<sub>SC</sub> and conversion efficiency of flexible TiO<sub>2</sub> film initially increased with the TiO<sub>2</sub> film thickness from 3 μm to 6 μm, but slightly decrease with a further increase in film thickness. In general, total amount of adsorbed dye on TiO<sub>2</sub> surface is proportional to the thickness of the TiO<sub>2</sub> layer. Therefore, the photocurrent density and conversion efficiency increase as thickness of the TiO<sub>2</sub> layer increases. This decline of efficiency and J<sub>SC</sub> was observed because the electron pathway from the top of the photoelectrode to the conducting substrate was too long to permit transport without recombination. Thin optimal thickness of flexible TiO<sub>2</sub> electrode is rationalized by the different diffusion length of each device. In general, low-temperature fabricated TiO<sub>2</sub> electrode shows poor electron diffusion coefficient due to lack of particle connectivity, and also reported by our previous result.[28] This poor electron diffusion property of flexible fabricated TiO<sub>2</sub> electrode implies the short electron diffusion length of TiO<sub>2</sub> film. The optimized conversion efficiencies of DSSCs based on individual

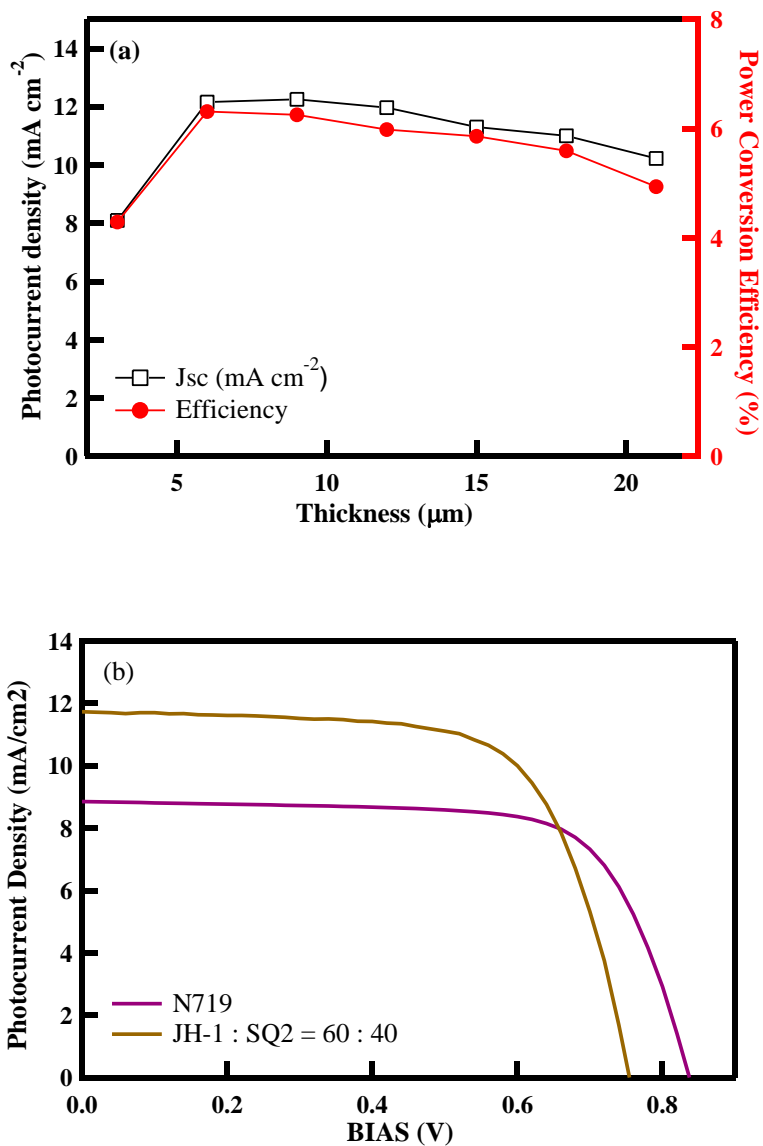


**Figure 4.8** Photovoltaic properties of (a) flexible DSSCs co-sensitized with molar ratio of 6:4 (JH1/SQ2) as a function of  $\text{TiO}_2$  thicknesses and (b) J-V characteristics of JH-1/SQ2 and N719-sensitized device.

JH-1, SQ2 and mixed (6:4, JH-1/SQ2) dye were 5.1%, 2.81%, and 6.31%, respectively. The co-sensitized flexible TiO<sub>2</sub> electrode showed greater J<sub>SC</sub> (12.32 mA cm<sup>-2</sup>) than those of DSSCs with the corresponding individual dyes (9.72 mA cm<sup>-2</sup> for JH-1 and 5.92 mA cm<sup>-2</sup> for SQ2). This large improvement of J<sub>SC</sub> of flexible TiO<sub>2</sub> photoelectrode by co-sensitization supports that co-sensitization is an effective approach to improve the J<sub>SC</sub> of thin film TiO<sub>2</sub> photoelectrode.

## 4.4 Conclusion

In this work, we demonstrated a highly efficient approach for flexible DSSCs by co-sensitization of JH-1 and SQ2 sensitizers. The complementary spectral response of JH-1 and SQ2 dyes was obtained because of different absorption properties (400 nm ~ 550 nm for JH-1 and 550 nm ~ 700 nm for SQ2) of the individual sensitizers. The absorption spectra of TiO<sub>2</sub> sensitized films exhibited extended absorption range and changed by the molar ratio of dye in mixed solution. The absorption kinetics of co-sensitizer was investigated using UV-visible absorption spectra. We found that the dye concentration of co-sensitized TiO<sub>2</sub> film is higher than that of individual dye-sensitized TiO<sub>2</sub> film. This increased dye loading of co-sensitized TiO<sub>2</sub>

photoelectrode lead to enhanced photovoltaic performance. It was also found that a co-sensitization of TiO<sub>2</sub> with high molar extinction sensitizers is more effective for flexible TiO<sub>2</sub> electrode because of short diffusion length of low-temperature fabricated TiO<sub>2</sub> layer. After optimizing the molar ratio of individual sensitizer and thickness of TiO<sub>2</sub> layer, the highest conversion efficiency of 6.31% was achieved for the flexible DSSCs with the molar ratio of 6 to 4 for JH-1 to SQ2 sensitizer.

## 4.5 References

- [1] O'regan, B.; Gratzel, M. *Nature* **1991**, 353, 737
- [2] Chiba, Y.; Islam, A.; Watanabe, Y.; Komiya, R.; Koide, N.; Han, L. *Jpn. J. Appl. Phys* **2006**, 45, 638
- [3] Gratzel, M. *Inorg. Chem.* **2005**, 44, 6841
- [4] Nazeeruddin, M. K.; De Angelis, F.; Fantacci, S.; Selloni, A.; Viscardi, G.; Liska, P.; Ito, S.; Takeru, B.; Gratzel, M. *J. Am. Chem. Soc.* **2005**, **127**, 16835
- [5] K. Fan, T. Peng, J. Chen, X. Zhang, R. Li, *J Power Sources*, **2013**, 222, 38
- [6] W. Guo, C. Xu, X. Wang, S. Wang, C. Pan, C. Lin, Z.L. Wang, *J Am*

*Chem Soc*, **2012**, 134, 4437

[7] J.-Y. Liao, B.-X. Lei, H.-Y. Chen, D.-B. Kuang, C.-Y. Su, *Energy & Environmental Science*, **2012**, 5 5750

[8] S. Senthilarasu, T.A.N. Peiris, J. García-Cañadas, K.G.U. Wijayantha, *J Phys Chem C*, **2012**, 116, 19053

[9] W. Wang, Q. Zhao, H. Li, H. Wu, D. Zou, D. Yu, *Adv Funct Mater*, **2012**, 22, 2775

[10] H.C. Weerasinghe, F. Huang, Y.-B. Cheng, *Nano Energy*, **2013**, 2, 174

[11] Durr, M.; Schmid, A.; Obermaier, M.; Rosselli, S.; Yasuda, A.; Nelles, G. *Nat. Mater.* **2005**, 4, 607

[12] Yamaguchi, T.; Tobe, N.; Matsumoto, D.; Nagai, T.; Arakawa, H. *Sol. Energy Mater. Sol. Cells* **2010**, 94, 812

[13] Boschloo, G.; Lindstrom, H.; Magnusson, E.; Holmberg, A.; Hagfeldt, A. *J. Photochem. Photobiol., A* **2002**, 148, 11

[14] Zhang, D.; Yoshida, T.; Furuta, K.; Minoura, H. *J. Photochem. Photobiol., A* **2004**, 164, 159

[15] Miyasaka, T.; Ikegami, M.; Kijitori, Y. *J. Electrochem. Soc.* **2007**, 154,

[16] Li, X.; Lin, H.; Li, J.; Wang, N.; Lin, C.; Zhang, L. *J. Photochem. Photobiol., A* **2008**, 195, 247

[17] Kim, K.; Lee, G. W.; Yoo, K.; Kim, D. Y.; Kim, J. K.; Park, N. G. *J.*

*Photochem. Photobiol., A* **2009**, 204, 144

[18] Zhang, D.; Yoshida, T.; Oekermann, T.; Furuta, K.; Minoura, H. *Adv. Funct. Mater.* **2006**, 16, 1228

[19] Yum, J. H.; Kim, S. S.; Kim, D. Y.; Sung, Y. E. *J. Photochem. Photobiol., A*. **2005**, 173, 1

[20] Grinis, L.; Kotlyar, S.; Ruhle, S.; Grinblat, J.; Zaban, A. *Adv. Funct. Mater.* **2010**, 20, 282

[21] Chen, H. W.; Liang, C. P.; Huang, H. S.; Chen, J. G.; Vittal, R.; Lin, C. Y.; Kevin, C. W. W.; Ho, K. C. *Chem. Commun.* **2011**, 47, 8346

[22] Fujimoto, M.; Kado, T.; Takashima, W.; Kaneto, K.; Hayase, S. J. *Electrochem. Soc.* **2006**, 153, A826

[23] Cha, S. I.; Koo, B. K.; Hwang, K. H.; Seo, S. H.; Lee, D. Y. *J. Mater. Chem.* **2011**, 21, 6300

[24] Li, X.; Zhang, Y.; Zhang, Z.; Zhou, J.; Song, J.; Lu, B.; Xie, E.; Lan, W. *J. Power Sources* **2010**, 196, 1639

[25] Park, N. G.; Kim, K. M.; Kang, M. G.; Ryu, K. S.; Chang, S. H.; Shin, Y. J. *Adv. Mater.* **2005**, 17, 2349

[26] Uchida, S.; Tomiha, M.; Takizawa, H.; Kawaraya, M. *J. Photochem. Photobiol., A* **2004**, 164, 93

[27] D. Hwang, H. Lee, S.-Y. Jang, S.M. Jo, D. Kim, Y. Seo, D.Y. Kim, *ACS*

*Applied Materials & Interfaces*, **2011**, 3, 2719

[28] H. Lee, D. Hwang, S.M. Jo, D. Kim, Y. Seo, D.Y. Kim, *ACS Applied Materials & Interfaces*, **2012**, 4, 3308

[29] F. Gao, Y. Wang, D. Shi, J. Zhang, M. Wang, X. Jing, R. Humphry-Baker, P. Wang, S.M. Zakeeruddin, M. Grätzel, *J Am Chem Soc*, **2008**, 130, 10720

[30] P. Wang, C. Klein, R. Humphry-Baker, S.M. Zakeeruddin, M. Grätzel, *J Am Chem Soc*, **2005**, 127, 808

[31] W.H. Howie, F. Claeysens, H. Miura, L.M. Peter, *J Am Chem Soc*, **2008**, 130, 1367

[32] H. Choi, I. Raabe, D. Kim, F. Teocoli, C. Kim, K. Song, J.-H. Yum, J. Ko, M.K. Nazeeruddin, M. Grätzel, *Chemistry – A European Journal*, **2010**, 16, 1193

[33] H. Chen, H. Huang, X. Huang, J.N. Clifford, A. Forneli, E. Palomares, X. Zheng, L. Zheng, X. Wang, P. Shen, B. Zhao, S. Tan, *J Phys Chem C*, **2010**, 114, 3280

[34] D. Kuang, P. Walter, F. Nüesch, S. Kim, J. Ko, P. Comte, S.M. Zakeeruddin, M.K. Nazeeruddin, M. Grätzel, *Langmuir*, **2007**, 23, 10906

[35] A. Yella, H.-W. Lee, H.N. Tsao, C. Yi, A.K. Chandiran, M.K. Nazeeruddin, E.W.-G. Diau, C.-Y. Yeh, S.M. Zakeeruddin, M. Grätzel,

*Science*, **2011**, 334, 629

[36] F. Huang, D. Chen, L. Cao, R.A. Caruso, Y.-B. Cheng, *Energy & Environmental Science*, **2011**, 4, 2803

[37] J. Kim, H. Lee, D.Y. Kim, Y. Seo, *Adv Mater*, **2014**, 26, 5192

[38] T. Geiger, S. Kuster, J.-H. Yum, S.-J. Moon, M.K. Nazeeruddin, M. Grätzel, F. Nüesch, *Adv Funct Mater*, **2009**, 19, 2720

# Chapter 5

## **Anisotropic piezoelectric generation of highly oriented PZT nanofibers for a flexible nanogenerator.**

### **5.1 Introduction**

Energy harvesting technologies have encountered several challenges over the past decade due to the exhaustion of certain fossil fuel sources and an increasing awareness of the environmental effects of current fuel consumption strategies. Devices that harvest energy from ambient sources, such as solar, [1-6] wind, [7, 8] mechanical vibrations, [9-15] or thermal energy, [16-19] have been developed recently as alternatives to fossil fuels. Among these, ‘nanogenerators’ show promise as renewable energy sources that directly convert vibrational or mechanical energy into electrical power. Piezoelectric nanogenerators are potentially useful in portable devices because they are flexible, light-weight, and their energy sources are readily accessible.

High-performance piezoelectric nanogenerators may be fabricated using a variety of piezoelectric materials, including ZnO, [20-26]  $\text{PbZr}_{0.52}\text{Ti}_{0.48}$  (PZT), [27-31]  $\text{BaTiO}_3$ , [32-35]  $\text{KNbO}_3$ , [36]  $\text{NaNbO}_3$ , [37] GaN, [38]

CdSe, [39] ZnSnO<sub>3</sub>, [40-42] and PVDF. [43-46] These inorganic materials alone are not readily compatible with flexible devices due to their brittleness; therefore, flexible piezoelectric nanogenerators have been fabricated by dispersing piezoelectric nanoparticles in a polydimethylsiloxane (PDMS) matrix. The morphology and geometry of these dispersions are important for device performance. A variety of nanoparticle-based piezoelectric materials, such as NaNbO<sub>3</sub> nanocubes and nanowires, [37] KNLN (0.942(K<sub>0.48</sub>Na<sub>0.535</sub>)NbO<sub>3</sub>-0.058LiNbO<sub>3</sub>), [36, 47] or PZT nanoparticles [31] have been tested in flexible nanogenerators. Although nanoparticle piezoelectric materials are more flexible than the bulk or thin film-based piezoelectric materials, the nanoparticles tend to be poorly dispersed throughout the matrix and do not readily form percolating networks within the PDMS matrix. Power generation measurements collected from nanoparticle-based nanogenerators have revealed that these devices are strain-mode dependent. Electricity tends to be generated only under large compressive forces. [26, 40] The compressive forces can induce unavoidable electrostatic noise associated with the triboelectric effect due to the interfacial contact between the nanogenerator and the measurement equipment. Moreover, the PDMS matrix and the polymeric substrate, typically polyethylene terephthalate (PET) or polyethylene naphthalate

(PEN), are easily charged and induce electrostatic noises (triboelectric effects) that obscure a quantitative analysis of the piezoelectric output. [48, 49]

Composite nanofibers comprising PDMS may potentially be useful as flexible piezoelectric nanogenerator materials. Chen et al. fabricated laterally aligned PZT nanofibers on interdigitated electrodes of a Pt wire array using the electrospinning method, and the nanogenerator generated a voltage of 1.6 V under an applied pressure.[29] Wu et al. fabricated a wearable nanogenerator using an electrospun PZT textile in which the nanofibers were oriented parallel to one another.[28] Following this report, Gu et al. obtained a 209 V output voltage from the vertically aligned PZT nanofiber array.[50] Previous studies have reported that nanofibers may be used as highly efficient flexible nanogenerators.

Here, we fabricated flexible nanogenerators based on electrospun PZT nanofibers in a PDMS matrix. The flexible devices were loaded onto a measurement unit and were deformed by bending to minimize the triboelectric effects resulting from mechanical friction. We characterized the effects of the device thickness, PZT textile stacking arrangement, device area, and fiber orientations on the piezoelectric output generation. The relationship between the piezoelectric output and the applied strain was

measured using PZT textiles having different orientations. Finally, we measured the piezoelectric outputs generated under different strain rates.

## **5.2 Experimental**

### **5.2.1 Preparation of the PZT nanofiber textiles**

PZT nanofiber textiles were prepared using the electrospinning method.[28] A solution containing 4.8 g anhydrous ethanol, 2.0 g acetylacetone, and 7.0 g acetic acid was mixed and stirred for 5 min using a magnetic stirrer. Acetic acid was added to the solution as a chelating agent. Next, 1.25 g tetrabutyltitanate, 1.862 g zirconium acetylacetonato, and 2.06 g lead subacetate were dissolved sequentially in the solution. Complete dissolution was achieved by stirring the resultant solution for 24 h at room temperature. Finally, 0.3 g polyvinylpyrrolidone (PVP,  $M_w = 1,300,000$ , Aldrich) was added to the precursor solution to obtain a viscosity appropriate for the spinning process.

The final PVP-containing PZT precursor solution was electrospun under a 10 kV electric field at a feed rate of  $15 \mu\text{L min}^{-1}$ . The relative humidity and

temperature were 40% and 25°C, respectively. The distance between the needle tip and the collector was 10 cm. The electrospun PZT nanofibers were collected onto a multi-pair parallel stainless steel wire to obtain the aligned PZT textile, as shown in Fig. 5.1(a). The radius of the stainless steel wires was 0.1 mm, and the gap between wires was 4 mm. The as-spun PZT textile was carefully peeled from the wire collector, and the as-spun PZT textile was annealed in two steps. The as-spun textile was first annealed at 150°C for 30 min to remove residual stress from the textile. The temperature was then increased to 650°C at a rate of 3°C min<sup>-1</sup>. The PZT textiles were further calcined over 3 h in air to remove residual PVP polymer. During the calcination and cooling procedures, PZT formed a polycrystalline phase. The composition ratio after calcination was PbZr<sub>0.52</sub>Ti<sub>0.48</sub>.

### **5.2.2 Device Fabrication**

A piece of the calcined PZT textile was placed on a cleaned ITO-PEN (Peccell Technology Inc., Japan) substrate. Poly(dimethylsiloxane) (PDMS, Sylgard 184, Dow Corning Corp.) was then spread onto the PZT textile, and the assembly was placed in a vacuum desiccator for 30 min to allow the PDMS to infiltrate the fibers and remove air bubbles from micropores in the

PDMS/PZT composite matrix. A second ITO-PEN substrate was placed on top of the PDMS/PZT composite layer, and the assembly was cured in an oven at 80°C for 2 h in air. During the curing process, the assembled devices were pressed slightly to squeeze out excess PDMS and reduce the thickness of the PZT/PDMS composite to the thickness of the PZT. Finally, a Cu wire was connected using a Ag epoxy paste at each end of the ITO-PEN electrodes and poled under an electric field of 7.5 kV/mm at 100°C for 12 h in an oil bath.

### **5.2.3 Characterization**

The morphologies and microstructures of the PZT nanofibers were analyzed by field-emission scanning electron microscopy (FE-SEM, Hitachi S-4100) and high-resolution transmission electron microscopy (HR-TEM, TECNAI F20 G<sup>2</sup>). The crystal structures of the PZT nanofibers were investigated using an X-ray diffractometer (XRD, D8 Advance). The output voltage and current were recorded using an analog signal recorder (e-Corder 401) and a current amplifier (Stanford Research SR-570). A constant strain was applied to the flexible PZT nanogenerator using a motorized bending machine.

## 5.3 Results and discussion

### 5.3.1 Morphologies of electrospun PZT nanofibers

Figure 5.1(a) shows a schematic diagram of the process used to fabricate the well-aligned PZT textiles. The well-aligned electrospun PZT textiles were prepared on multi-pair parallel electrodes. The PZT nanowires aligned as a result of the repulsive forces among the negatively charged fibers on parallel wire collectors. The average diameter of a PZT fiber was ca. 270 nm for the as-spun fibers and 220 nm after calcination. The small fiber diameter resulted from the degradation of the PVP polymer during the high-temperature calcination process. SEM images of the well-aligned PZT textiles after the calcination process are shown in Figure 5.1(b). The individual PZT nanofibers collected were uniformly orientated and formed highly porous structures. The porous structures of the PZT textiles facilitated the infiltration of the viscous PDMS elastomer to form the flexible matrix of the piezoelectric nanogenerator device. The degree of orientation alignment was determined by calculating the fiber orientation factor  $S$ ,

$$S = \langle (3\cos^2\theta - 1)/2 \rangle, \quad \text{Eq. (1)}$$

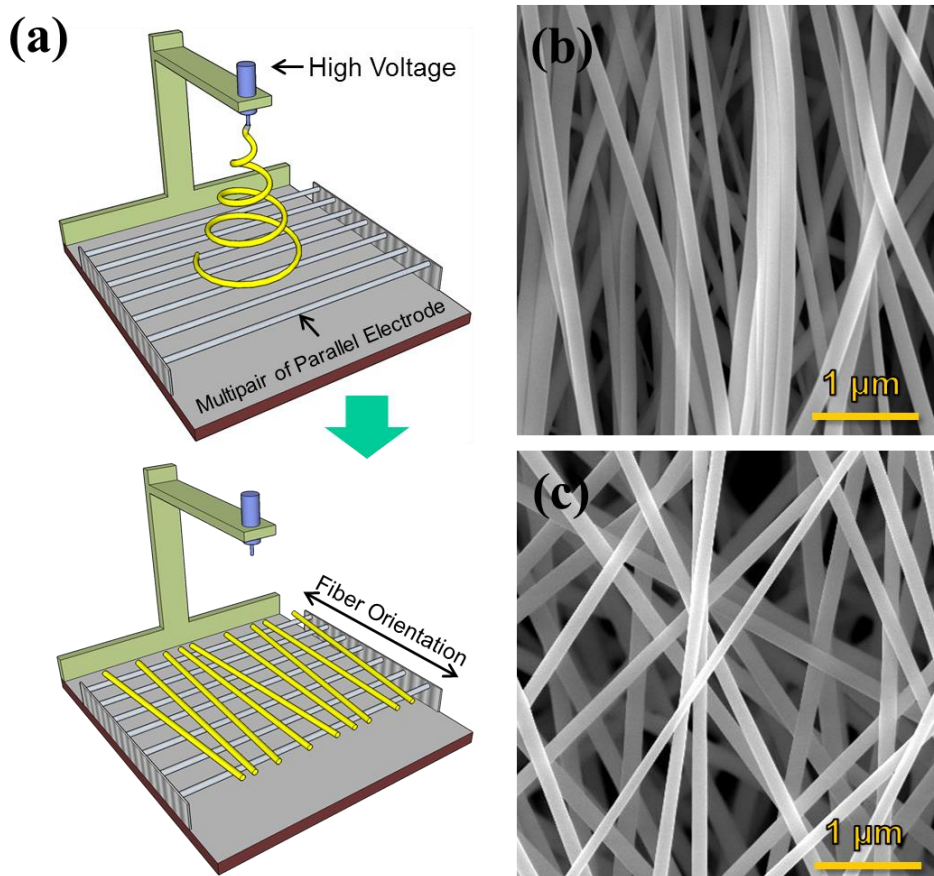


**Figure 5.1** (a) Schematic diagram showing the process of fabricating the aligned PZT textiles by electrospinning onto multi-pair metal wire collectors. (b and c) SEM images of the PZT textile prepared with a parallel orientation and the randomly oriented PZT textile, respectively.

where  $\theta$  is the angle formed between the individual electrospun fibers and the multi-pair metal wires.[51] The S value of the electrospun PZT textile, which could range from 0 for anisotropic orientation to 1 for perfect alignment, was 0.896. We fabricated a randomly oriented PZT textile using a metal mesh collector to characterize the effects of the fiber orientation on piezoelectricity generation, as shown in Figure 1(c). The S value of the randomly oriented PZT textile was 0.219. The large difference between the orientations in the two textiles could affect the piezoelectric properties of the assembled devices. The effects of the orientation on piezoelectricity generation will be discussed below.

The X-ray diffraction (XRD) profiles collected from the calcined PZT nanofibers are provided in Figure 5.2(a). All peaks in Figure 5.2(a) corresponded to a fully crystallized pure perovskite PZT phase, and no impurity components were observed in the samples after calcination at 650°C for 3 h. Figures 5.2(b) and 5.2(c) show high-resolution transmission electron microscopy (HR-TEM) images collected from a single electrospun PZT nanofibers. The corresponding selective area electron diffraction (SAED) pattern is also provided. The HR-TEM images indicated that the calcined PZT nanofibers were highly polycrystalline, with a lattice separation of 2.9 Å in the (101) lattice plane.

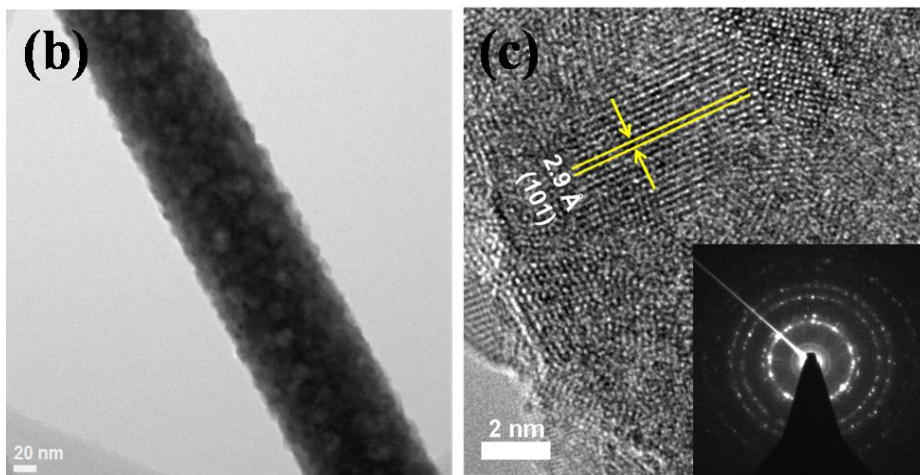
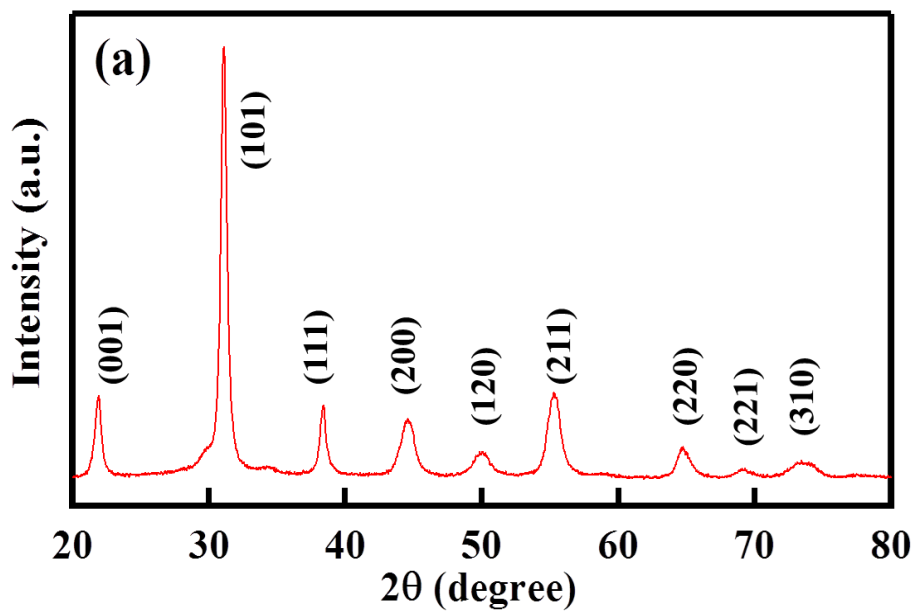


**Figure 5.2** (a) XRD pattern of a calcined PZT textile. (b) TEM image of a single PZT nanofiber. (c) High-resolution TEM image of a PZT nanofiber. The inset image shows a SAED pattern of a PZT nanofiber.

### 5.3.2 Structure of assembled flexible nanogenerator

A schematic diagram of an assembled flexible nanogenerator based on the well-aligned PZT textile embedded in a PDMS composite structure is shown in Figure 5.3(a). The PZT/PDMS composite layer was sandwiched between two flexible ITO-PEN films and featured a strain-neutral line along the middle of the PZT/PDMS composite layer. Thus, the upper and lower parts of the PZT/PDMS layer were subject to tensile and compressive strains and strain in the PZT/PDMS depended on the distance from the strain-neutral line. The performances of the two devices were characterized quantitatively, assuming that the strain applied to the top layer of the PZT/PDMS layer was equally distributed throughout the composite layer. The applied strain was calculated according to equation (2),

$$\varepsilon = r / R = t/2R = t \times h / (a^2 + h^2), \quad \text{Eq.(2)}$$

where  $r$  is the distance from the strain-neutral line to the top of the composite layer,  $R$  is the radius of the strain-neutral arc,  $t$  is the thickness of the PZT/PDMS composite layer,  $h$  is the height of the arc, and  $a$  is the

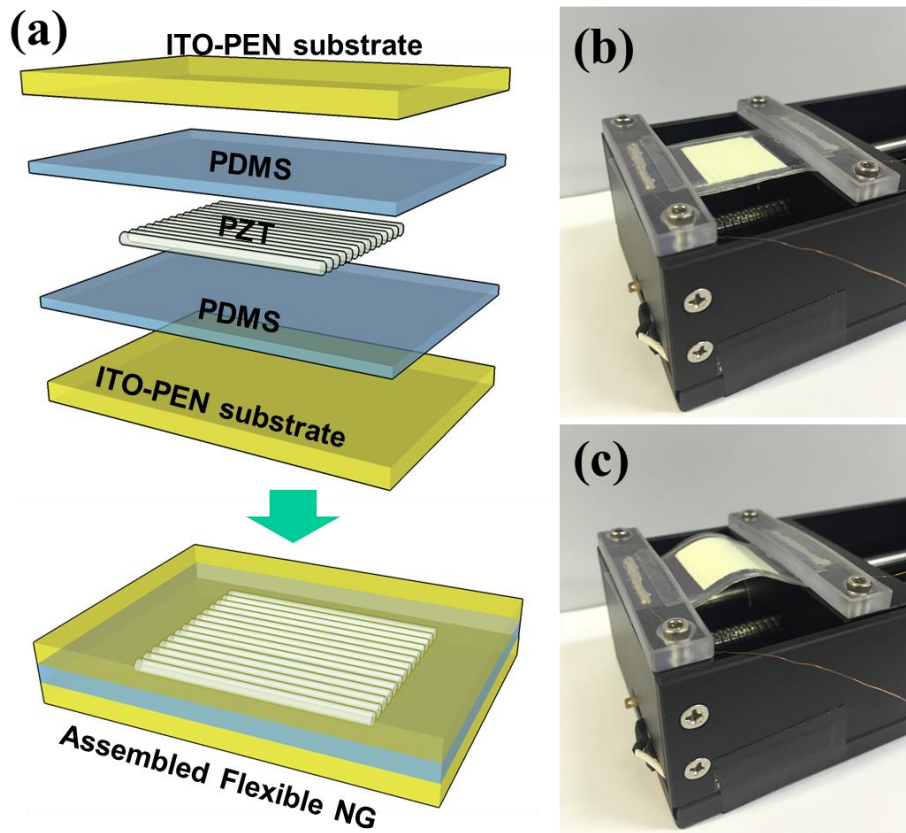


**Figure 5.3** (a) Structural illustration of the flexible piezoelectric nanogenerator. (b and c) Photographic images of the devices assembled on a measurement station without deformations or with deformations, respectively.

half-width of the arc. The elastic modulus of the PDMS was much smaller than that of the PZT material so that the real applied strain on the PZT nanofiber was smaller than the actual applied strain on the PZT/PDMS composite layer.

Figures 5.3(b) and 5.3(c) show photographic images of the assembled flexible nanogenerator in the initial and bending states, respectively. The linear motor moved back and forth to periodically apply bending and unbending motions, respectively. During the bending motion, the applied strain on the flexible nanogenerator was transferred to the PZT nanofibers in the textile through the flexible PDMS matrix. This strain produced a piezoelectric potential, and the generated charges accumulated at the two electrodes. As the applied strain was released, the accumulated electrons moved back in the opposite direction, and the built-up piezoelectric potential disappeared. Under periodic strain induced by the bending and releasing motions, the flexible PZT nanogenerator generated an alternating piezoelectric voltage and current.

It is important to distinguish the real piezoelectric voltage from the triboelectric voltage (electrostatic voltage). Before characterizing the nanogenerator, we fabricated a PDMS-only sample without the PZT textile and measured the electric signal induced by the bending motions. As

shown in Figures 5.4(a) and 5.4(b), the electric signals were insignificant. This observation suggested that the output power generated by the PDMS/PZT composite generator arose from electrons induced by the piezoelectricity under mechanical strain. We examined the poling effects of the PZT on the piezoelectric output (see Figure 5.5(a) and 5.5(b)). The electric poling process improves the alignment of electric dipoles along an applied electric field direction, thereby increasing the piezoelectric output. The measured output voltage and current increased as the poling field increased and reached saturation at an electric field strength of  $7.5 \text{ kV mm}^{-1}$ . A polarity switching test was conducted to verify that the electric signal originated from piezoelectric effects (see Figures 5.6(a) and 5.6(b)). Inverted polarities were measured in a device prepared with reverse connections, revealing that the electric signals of the nanogenerator measured during the bending motion arose only from the piezoelectric effects of the PZT textile in the PZT/PDMS composite layer.

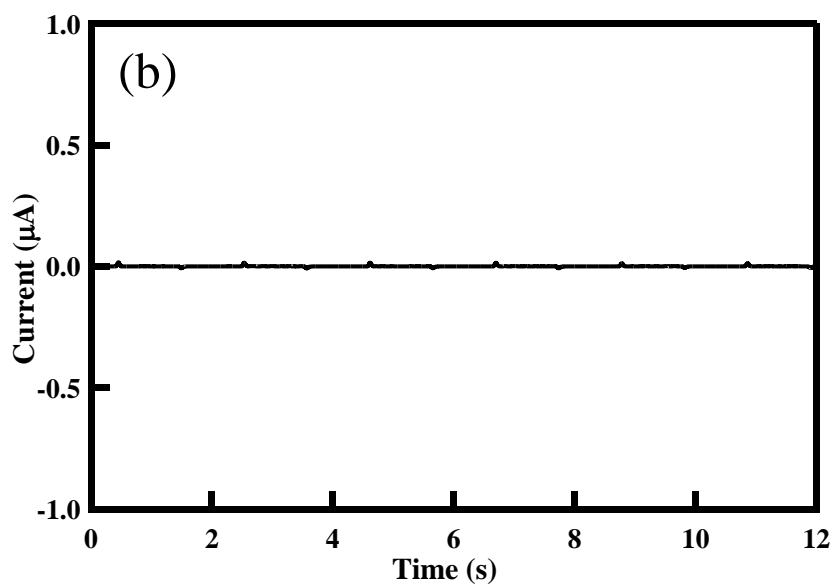
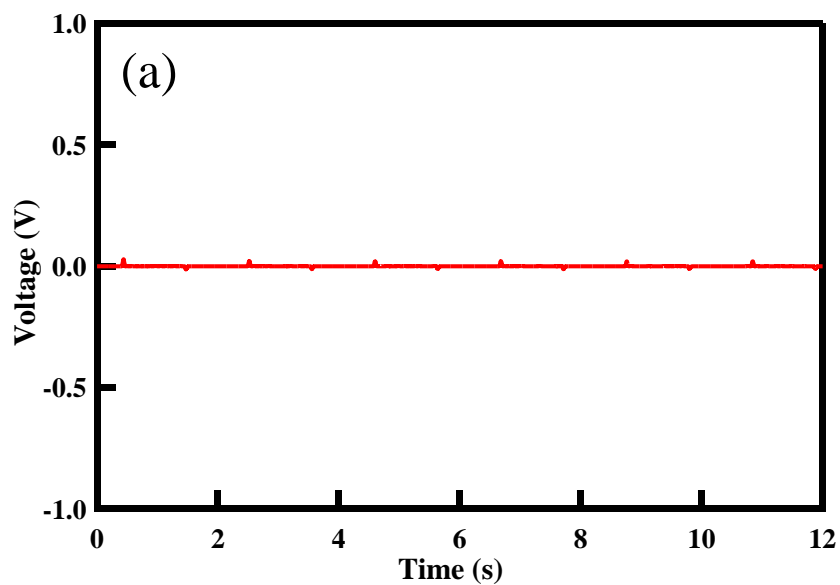


**Figure 5.4** Piezoelectric voltage (a) and current (b) of PDMS-only nanogenerator.

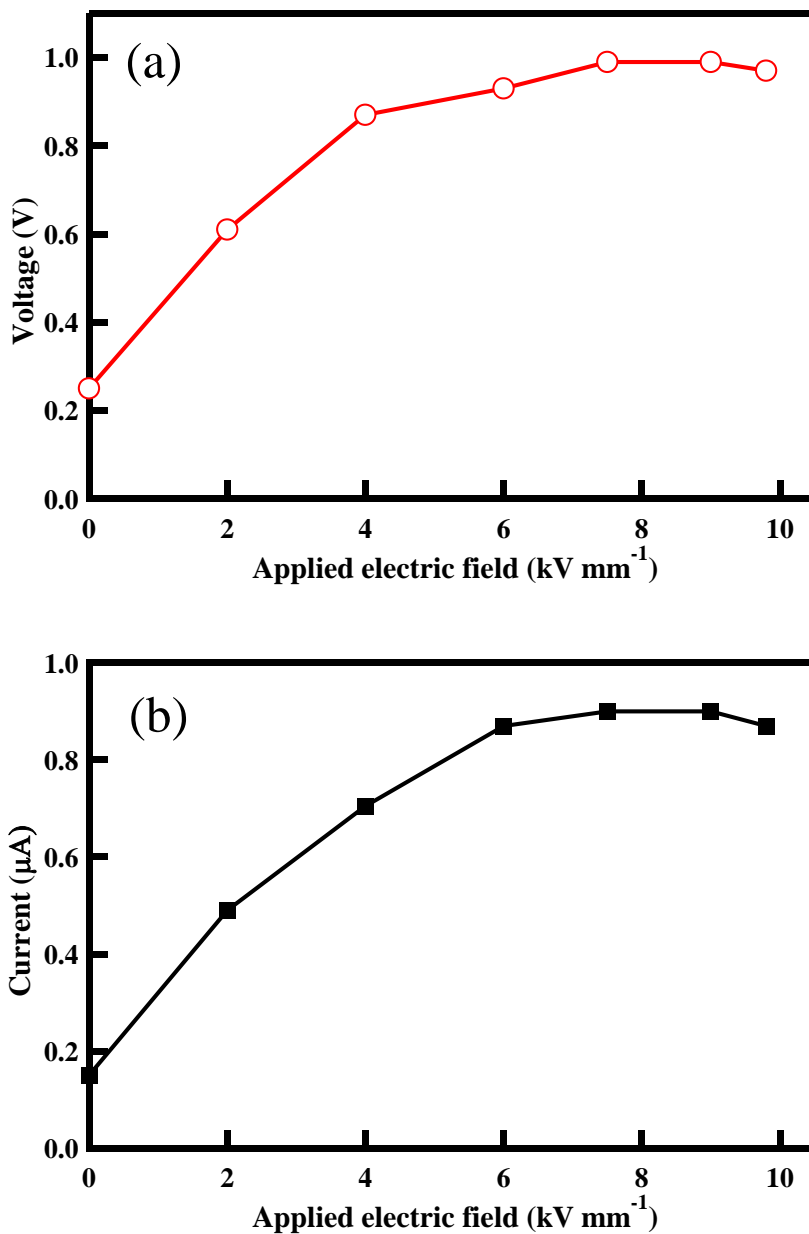


**Figure 5.5** Piezoelectric voltage (a) and current (b) as a function of applied electric field

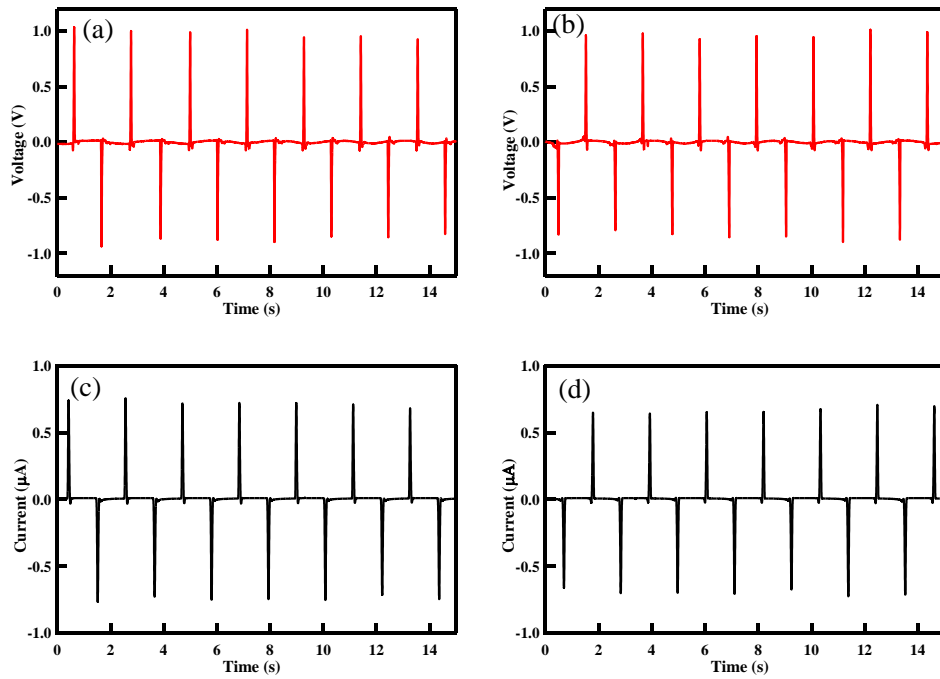


**Figure 5.6** (a and c) Output voltage and current under the forward connection. (b and d) Output voltage and current under the reverse connection.

### **5.3.3 Piezoelectric Generation – Thickness and area dependence**

The piezoelectric power generation and related parameters were investigated by measuring the output voltage and current in the assembled PZT flexible nanogenerator as a function of the PZT thickness, which was varied from 20 nm to 40 nm. Figures 5.7 (a) and 7(b) show the measured output voltage and current, respectively. The strain induced by the bending motion was 0.18%, and the area of the PZT was 4 cm<sup>2</sup> (2 cm×2 cm). The measured values are listed in Table 1. As shown in Figures 5.7(a) and 7(b), the piezoelectric voltage and current increased as the PZT thickness increased. Because the individual PZT fibers in the PDMS/PZT matrix acted as a piezoelectric source, both the piezoelectric voltage and the current increased linearly as a function of the amount of PZT present, indicated by the thickness. The output voltage and current of the device were enhanced in flexible nanogenerators assembled by stacking two identical layers. The resulting device performances are plotted in Figures 5.7(c) and 5.7(d). The measured values are listed in Table 5.1. The output voltage and current obtained from a two-layer stacked device was twice the value obtained from a one-layer stack, as shown in Figures 5.7(c) and 5.7(d). These results

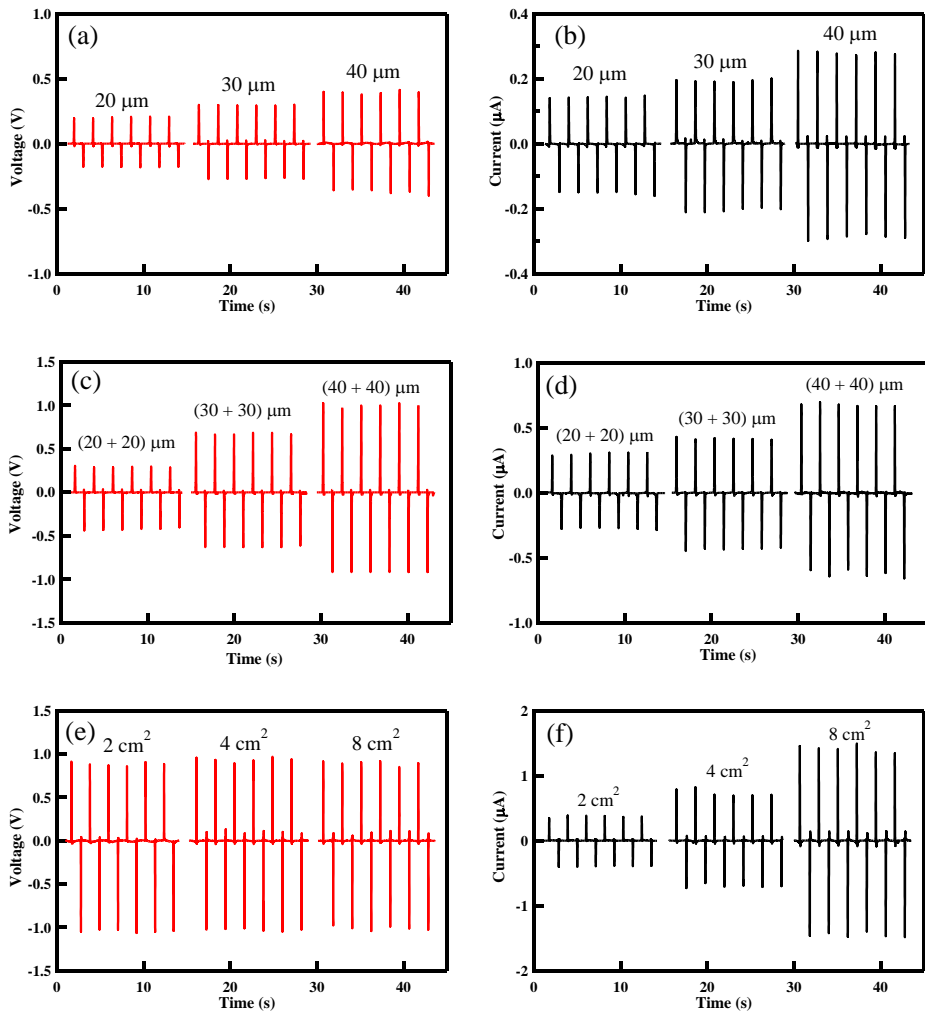


**Figure 5.7** (a) Output voltage, and (b) current measured in a single layer PZT nanogenerator, as a function of the PZT layer thickness. The area of the PZT was 4 cm<sup>2</sup>. (c) The output voltage and (d) current measured in the two-layer PZT nanogenerator as a function of the thickness. The area of the PZT was 4 cm<sup>2</sup>. (e) The output voltage and (f) current of a two-layer PZT nanogenerator prepared with different areas. The thickness of each PZT was 40 μm (total 80 μm).

PZT thickness ( $\mu\text{m}$ )	PZT area ( $\text{cm}^2$ )	$V_{\text{MAX}}$ (V)	$I_{\text{MAX}}$ ( $\mu\text{A}$ )	$J_{\text{MAX}}$ ( $\mu\text{A cm}^{-2}$ )
20	4	0.22	0.15	0.0375
30	4	0.31	0.19	0.0475
40	4	0.43	0.28	0.07
20 + 20	4	0.45	0.30	0.075
30 + 30	4	0.72	0.45	0.1125
40 + 40	4	1.03	0.72	0.18
40 + 40	2	0.94	0.39	0.195
40 + 40	4	0.99	0.82	0.205
40 + 40	8	0.93	1.58	0.1975

**Table 5.1** Output signals obtained from the flexible piezoelectric nanogenerators prepared with different thicknesses and areas

indicated that both the piezoelectric voltage and current depended on the PZT thickness. The stacking of PZT layers provides an effective approach to obtaining high-performance piezoelectric nanogenerators.

We investigated the effects of the PZT area on the performances of the assembled devices. The device thickness was fixed during these measurements, and only the areas of the two-layered PZTs (each layer was 40  $\mu\text{m}$  thick) were varied. The effects of geometry were minimized by fixing the sample length at 2 cm while varying the PZT width. The output voltage and current are shown in Figures 5.7(e) and 5.7(f), respectively. It should be noted that the output voltages of the three devices were independent of the PZT thickness, although the output current increased linearly with the thickness. The output current densities of all devices were 0.2  $\mu\text{A cm}^{-2}$ . Therefore, we concluded that the piezoelectric voltage depended on the PZT thickness, whereas the piezoelectric current was affected by both the thickness and area of the PZT layer.

### **5.3.4 Piezoelectric Generation – Bending orientation dependence**

The effects of the fiber orientations in the PZT/PDMS composite layer and the bending direction on the piezoelectric performance were next tested. Figure 5.8(a) shows a schematic diagram of the different devices assembled using the oriented PZT textiles. The device nomenclature indicates the fiber orientation and bending motion. The randomly oriented PZT textile was collected by electrospinning onto a mesh-type collector. SEM images of the randomly oriented PZT nanofibers are shown in Figure 5.1(c). The PZT fiber orientation on the mesh-type collector was not perfectly isotropic because the grids in the mesh-type collector were aligned in a parallel fashion. The S value of the nanofibers was 0.219. The physical properties, such as the average fiber diameter, length, and density remained constant, and only the orientations of the PZT fibers were varied in this set of studies.

Although the strain applied to the flexible nanogenerators was fixed (0.18%), significant differences in the piezoelectric voltages and current signals were obtained, as shown in Figures 5.8(b) and 5.8(c). The piezoelectric voltage and current of the perpendicular device were 0.22 V and 0.16  $\mu\text{A}$ , respectively. These values were 24% and 23.5% of the voltage

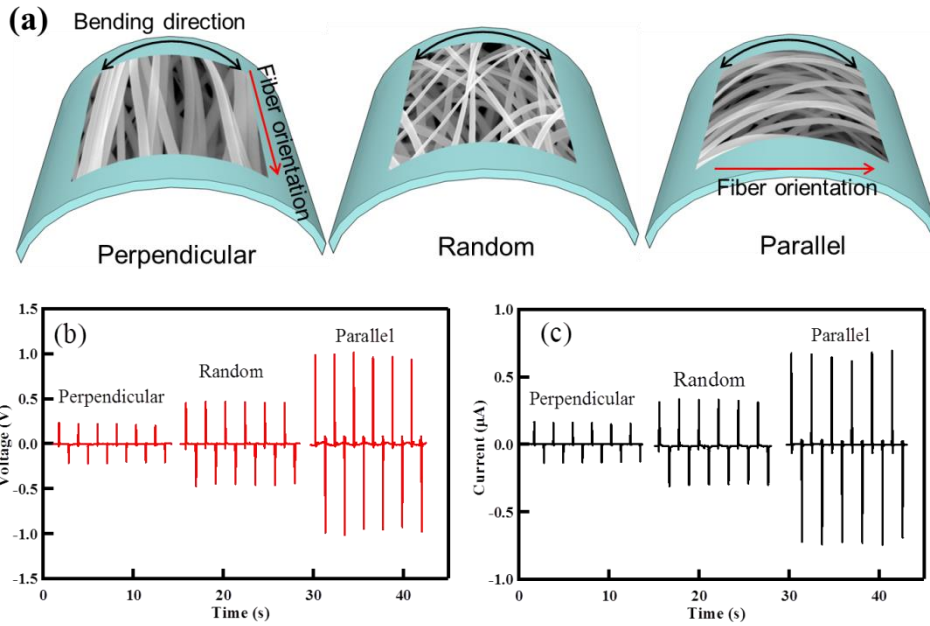


**Figure 5.8** (a) Schematic diagram showing a flexible PZT nanogenerator embedded in different PZT textiles. (b) Output voltage and (c) current measured from three different nanogenerators under identical measurement conditions.

and current values measured in the parallel devices, respectively. The large difference between the piezoelectric signals suggested that the real strains on the PZT nanofibers in the composite layers differed and depended on the fiber orientation. The bending direction and fiber orientation were parallel in the parallel devices. A large fraction of the PZT nanofibers became deformed along the longitudinal direction as the device was bent. On the other hand, the bending direction and fiber orientation in the perpendicular devices were orthogonal. Therefore, few PZT nanofibers were stretched along the longitudinal direction. For this reason, the perpendicular device showed a much lower degree of piezoelectricity generation than the parallel device. The voltage and current generated in the random device were, respectively, 49% and 48% of the values measured in the parallel device. Although the fiber orientation factor ( $S$ ) in the random device was much lower than the value measured in the perpendicular device, the electric output of the random device exceeded that obtained from the perpendicular device. The fiber orientations in the random device were isotropic; therefore, the number of deformed PZT fibers in the random device that were oriented along the bending direction exceeded the value present in the perpendicular device. The random device, therefore, provided a higher piezoelectric output than the perpendicular device.

### **5.3.5 Piezoelectric Generation – Strain and Strain rate dependence**

The voltage and current generated from the nanogenerator were investigated as a function of the applied strain for different bending directions. The area of the PZT was 2 cm×2 cm and the thickness of the PZT/PDMS composite layer was fixed to 80 μm (40 + 40 μm). The strain range was limited to 0.2% to prevent buckling in the flexible device. As shown in Figures 5.9 (a) and 5.9 (b), the voltage and current in the devices were proportional to the applied strain. The output voltage and current followed the trends plotted in Figures 5.8(b) and 5.8(c) across the measured strain range, but the slope of the output voltage and the current differed. Interestingly, the output voltage and current in the parallel device increased slowly as the strain increased from 0.02% to 0.13%, whereas the output voltage and current increased rapidly as the strain increased from 0.13% to 0.18%. The different slope of the output voltage and current measured from the parallel device could be divided into two strain regions. At strains below 0.13%, the strain was not sufficient to generate a significant piezoelectric signal, and only small lattice distortions were obtained among the PZT nanofibers. The PDMS in the composite layer endured the majority of the

applied strain due to its flexibility at lower strains. Thus, the orientations among the PZT nanofibers were not critical to the piezoelectric output. The three different devices showed similar piezoelectric performances, as shown in Figures 5.8(a) and 5.8(b). Strains beyond 0.13% yielded rapid increase of output voltages and currents in the parallel device that exceeded the values measured in the other devices. A maximum voltage of 1.1 V and a current of 0.85  $\mu\text{A}$  were obtained. The high output voltage and current indicated that an applied strain exceeding 0.14% produced a large actual deformation in the PZT nanofibers in PDMS/PZT composite layer. The strong increase of piezoelectric signal was attributed to heterogeneous polarization at the interface between the PZT nanofibers and the PDMS matrix. As the composite layer bent under the applied strain, crystallized PZT grains in the composite layer narrowed under the compressive strain to create large Maxwell–Wagner–Sillars polarization effects at the interface between the PZT nanofibers and the PDMS matrix.[40, 47, 52] The piezoelectric output voltage and current trends by applied strain agreed well with the trends reported previously.[26, 40] Although the trends of piezoelectric signals measured from the random device were similar with those measured in the parallel device, the slope of the piezoelectric signal was lower than that of the corresponding signal measured in the parallel devices due to poor PZT

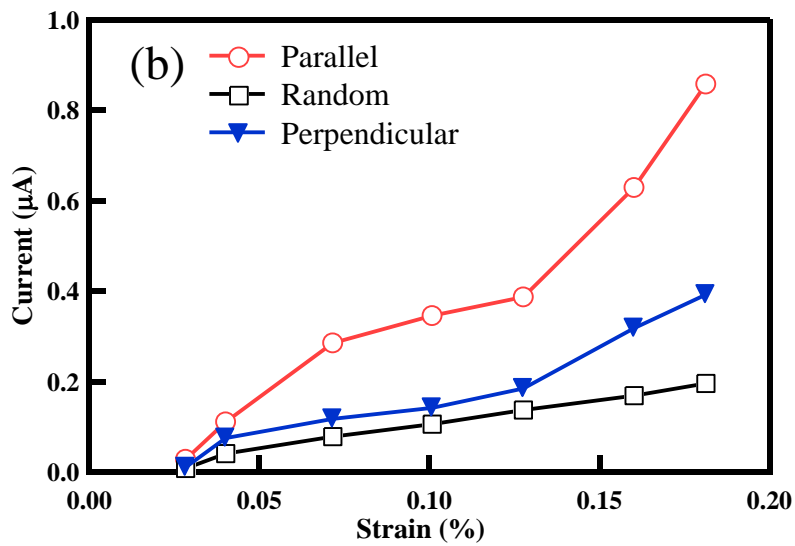
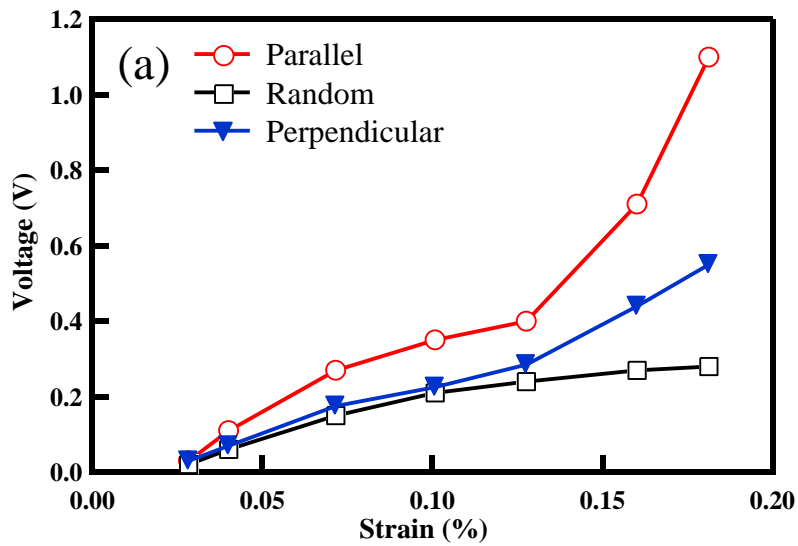


**Figure 5.9** Strain dependence of (a) the output voltage and (b) the output current as a function of the strain for three different nanogenerators.

fiber orientations, as discussed above. In the perpendicular devices, the piezoelectric output signal was small and increased linearly within the measured strain range. The PZT nanofibers were oriented orthogonal to the bending axis such that bending motions did not induce much strain on the PZT nanofibers. These small deformations were not sufficient to create stress-induced poling effects. The perpendicular devices, therefore, did not show abrupt increases in the output signal at strains beyond 0.18%.

We next investigated the piezoelectric performance as a function of the strain rate. Strain rates ranging from 0.04 to 1.36 s<sup>-1</sup> were applied by modifying the speed of the bending machine. The total applied strain was fixed to 0.18%. The piezoelectric voltage and current were proportional to the applied strain rate, as shown in Figures 5.10 (a) and 5.10 (b). As the applied strain rate increased, the charges in the external circuit were transported more rapidly to neutralize the piezoelectric voltage. This rapid transport of charge resulted in a large piezoelectric current. Because the output voltage is the product of the output current and the external resistance, the voltage is proportional to the applied strain rate. These results were consistent with the fundamental equation describing piezoelectricity, as expressed by Eq. (3),

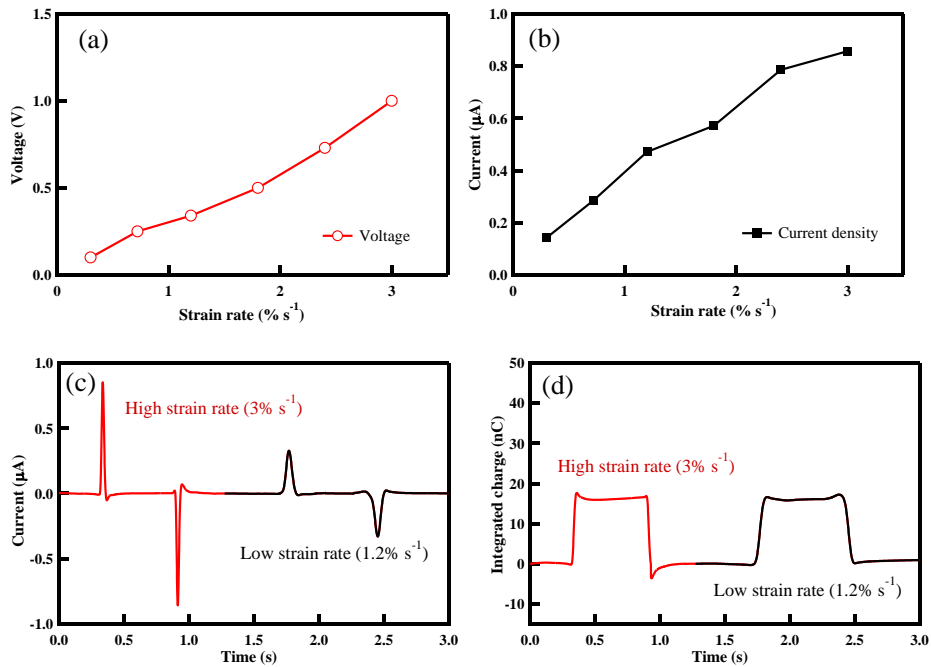


**Figure 5.10** Strain rate dependence of (a) the output voltage and (b) the current of a flexible PZT nanogenerator. (c) Output current and (d) integrated charge of a flexible nanogenerator subject to two different strain rates under the same applied strain. Here, the device was assembled using a two-layer PZT nanogenerator (80 μm and 4 cm<sup>2</sup>), and measurements were collected under an applied strain of 0.18%.

$$i = dq/dt = d_{33}EA(d\varepsilon/dt), \quad \text{Eq. (3)}$$

where  $i$  is the output current,  $q$  is the generated charge,  $d_{33}$  is the piezoelectric charge constant,  $E$  is the Young's modulus,  $A$  is the cross-sectional area,  $\varepsilon$  is the applied strain, and  $t$  is time. Figures 5.10(c) and 5.10(d) plot the output current and integrated charge of the nanogenerator as a function of the strain rate under a given applied strain. As mentioned above, the current signal at a high strain rate displayed sharper and narrower peaks compared to the current signal at a low strain rate. Maximum output currents of 0.86 and 0.29  $\mu\text{A}$  were measured under strain rates of 1.36 and 0.11  $\text{s}^{-1}$ , respectively. Equation (3) indicated that the integral of the measured output current represented the external free charges transported from the external circuit to the nanogenerator (Figure 5.10 (d)). It should be noted that the total charges generated under different strain rates remained constant. The negligible discrepancies between the total charges measured under a given applied strain indicated the absence of piezoelectric charge leakage through the nanogenerator during the bending process.

## 5.4 Conclusion

We fabricated a flexible piezoelectric nanogenerator using highly oriented PZT nanofibers in a PDMS matrix. The oriented PZT nanofibers were electrospun onto multi-pair parallel metal wires. The performance parameters of the nanogenerator were investigated under bending motions. The output voltage increased with the PZT thickness, whereas the output current increased as the PZT thickness and area increased. We obtained a 1.1 V output voltage and a 1.4  $\mu\text{A}$  output current at a PZT thickness of 80  $\mu\text{m}$  and an area of 8  $\text{cm}^2$ . The piezoelectric output performance was found to depend on the degree to which the fibers were uniformly oriented as well as the bending direction. The piezoelectric output of a device in which the bending direction and fiber orientations were parallel increased rapidly at large strains, and a mechanism was proposed to describe this behavior. We demonstrated that the output voltage and current depended on the strain rate, but the total amount of generated charge was independent of the strain rate.

## 5.5 References

- [1] W. U. Huynh, J. J. Dittmer, A. P. Alivisatos, *Science* **2002**, *295*, 2425.
- [2] S. Jeong, E. C. Garnett, S. Wang, Z. Yu, S. Fan, M. L. Brongersma, M. D. McGehee, Y. Cui, *Nano Lett.* **2012**, *12*, 2971.
- [3] B. O'Regan, M. Gratzel, *Nature* **1991**, *353*, 737.
- [4] J. C. Shin, P. K. Mohseni, K. J. Yu, S. Tomasulo, K. H. Montgomery, M. L. Lee, J. A. Rogers, X. Li, *ACS Nano* **2012**, *6*, 11074.
- [5] J. Yang, J. You, C.-C. Chen, W.-C. Hsu, H.-r. Tan, X. W. Zhang, Z. Hong, Y. Yang, *ACS Nano* **2011**, *5*, 6210.
- [6] Y. Yang, H. Zhang, Y. Liu, Z.-H. Lin, S. Lee, Z. Lin, C. P. Wong, Z. L. Wang, *ACS Nano* **2013**, *7*, 2808.
- [7] Y. Xie, S. Wang, L. Lin, Q. Jing, Z.-H. Lin, S. Niu, Z. Wu, Z. L. Wang, *ACS Nano* **2013**, *7*, 7119.
- [8] S. Lee, S.-H. Bae, L. Lin, Y. Yang, C. Park, S.-W. Kim, S. N. Cha, H. Kim, Y. J. Park, Z. L. Wang, *Adv. Funct. Mater.* **2013**, *23*, 2445.
- [9] X. Wang, J. Song, J. Liu, Z. L. Wang, *Science* **2007**, *316*, 102.
- [10] J. Chen, G. Zhu, W. Yang, Q. Jing, P. Bai, Y. Yang, T.-C. Hou, Z. L. Wang, *Adv. Mater.* **2013**, *25*, 6094.

- [11] S. N. Cha, J.-S. Seo, S. M. Kim, H. J. Kim, Y. J. Park, S.-W. Kim, J. M. Kim, *Adv. Mater.* **2010**, *22*, 4726.
- [12] N. Cui, L. Gu, J. Liu, S. Bai, J. Qiu, J. Fu, X. Kou, H. Liu, Y. Qin, Z. L. Wang, *Nano Energy* **2015**, *15*, 321.
- [13] K. N. Kim, J. Chun, J. W. Kim, K. Y. Lee, J.-U. Park, S.-W. Kim, Z. L. Wang, J. M. Baik, *ACS Nano* **2015**, *9*, 6394.
- [14] W. Seung, M. K. Gupta, K. Y. Lee, K.-S. Shin, J.-H. Lee, T. Y. Kim, S. Kim, J. Lin, J. H. Kim, S.-W. Kim, *ACS Nano* **2015**, *9*, 3501.
- [15] W. Tang, T. Jiang, F. R. Fan, A. F. Yu, C. Zhang, X. Cao, Z. L. Wang, *Adv. Funct. Mater.* **2015**, *25*, 3718.
- [16] Y. Yang, W. Guo, K. C. Pradel, G. Zhu, Y. Zhou, Y. Zhang, Y. Hu, L. Lin, Z. L. Wang, *Nano Lett.* **2012**, *12*, 2833.
- [17] Y. Yang, J. H. Jung, B. K. Yun, F. Zhang, K. C. Pradel, W. Guo, Z. L. Wang, *Adv. Mater.* **2012**, *24*, 5357.
- [18] J.-H. Lee, K. Y. Lee, M. K. Gupta, T. Y. Kim, D.-Y. Lee, J. Oh, C. Ryu, W. J. Yoo, C.-Y. Kang, S.-J. Yoon, J.-B. Yoo, S.-W. Kim, *Adv. Mater.* **2014**, *26*, 765.
- [19] Y. Yang, S. Wang, Y. Zhang, Z. L. Wang, *Nano Lett.* **2012**, *12*, 6408.

- [20] S. Y. Chung, S. Kim, J.-H. Lee, K. Kim, S.-W. Kim, C.-Y. Kang, S.-J. Yoon, Y. S. Kim, *Adv. Mater.* **2012**, *24*, 6022.
- [21] A. Khan, M. Ali Abbasi, M. Hussain, Z. Hussain Ibupoto, J. Wissting, O. Nur, M. Willander, *Appl. Phys. Lett.* **2012**, *101*, 193506.
- [22] S.-H. Shin, Y.-H. Kim, M. H. Lee, J.-Y. Jung, J. H. Seol, J. Nah, *ACS Nano* **2014**, *8*, 10844.
- [23] Z. L. Wang, J. Song, *Science* **2006**, *312*, 242.
- [24] M.-P. Lu, J. Song, M.-Y. Lu, M.-T. Chen, Y. Gao, L.-J. Chen, Z. L. Wang, *Nano Lett.* **2009**, *9*, 1223.
- [25] J. Chun, K. Y. Lee, C.-Y. Kang, M. W. Kim, S.-W. Kim, J. M. Baik, *Adv. Funct. Mater.* **2014**, *24*, 2038.
- [26] J. Chun, N.-R. Kang, J.-Y. Kim, M.-S. Noh, C.-Y. Kang, D. Choi, S.-W. Kim, Z. Lin Wang, J. Min Baik, *Nano Energy* **2015**, *11*, 1.
- [27] Y. Qi, N. T. Jafferis, K. Lyons, C. M. Lee, H. Ahmad, M. C. McAlpine, *Nano Lett.* **2010**, *10*, 524.
- [28] W. Wu, S. Bai, M. Yuan, Y. Qin, Z. L. Wang, T. Jing, *ACS Nano* **2012**, *6*, 6231.
- [29] X. Chen, S. Xu, N. Yao, Y. Shi, *Nano Lett.* **2010**, *10*, 2133.
- [30] S. Xu, B. J. Hansen, Z. L. Wang, *Nat Commun* **2010**, *1*, 93.

- [31] K.-I. Park, C. K. Jeong, J. Ryu, G.-T. Hwang, K. J. Lee, *Advanced Energy Materials* **2013**, *3*, 1539.
- [32] K.-I. Park, S. Xu, Y. Liu, G.-T. Hwang, S.-J. L. Kang, Z. L. Wang, K. J. Lee, *Nano Lett.* **2010**, *10*, 4939.
- [33] S.-H. Shin, Y.-H. Kim, M. H. Lee, J.-Y. Jung, J. Nah, *ACS Nano* **2014**, *8*, 2766.
- [34] Z.-H. Lin, Y. Yang, J. M. Wu, Y. Liu, F. Zhang, Z. L. Wang, *The Journal of Physical Chemistry Letters* **2012**, *3*, 3599.
- [35] K.-I. Park, M. Lee, Y. Liu, S. Moon, G.-T. Hwang, G. Zhu, J. E. Kim, S. O. Kim, D. K. Kim, Z. L. Wang, K. J. Lee, *Adv. Mater.* **2012**, *24*, 2999.
- [36] J. Jong Hoon, C. Chih-Yen, Y. Byung Kil, L. Nuri, Z. Yusheng, J. William, C. Li-Jen, W. Zhong Lin, *Nanotechnology* **2012**, *23*, 375401.
- [37] J. H. Jung, M. Lee, J.-I. Hong, Y. Ding, C.-Y. Chen, L.-J. Chou, Z. L. Wang, *ACS Nano* **2011**, *5*, 10041.
- [38] C.-T. Huang, J. Song, W.-F. Lee, Y. Ding, Z. Gao, Y. Hao, L.-J. Chen, Z. L. Wang, *J. Am. Chem. Soc.* **2010**, *132*, 4766.
- [39] Y. S. Zhou, K. Wang, W. Han, S. C. Rai, Y. Zhang, Y. Ding, C. Pan, F. Zhang, W. Zhou, Z. L. Wang, *ACS Nano* **2012**, *6*, 6478.

- [40] K. Y. Lee, D. Kim, J.-H. Lee, T. Y. Kim, M. K. Gupta, S.-W. Kim, *Adv. Funct. Mater.* **2014**, *24*, 37.
- [41] J. M. Wu, C. Xu, Y. Zhang, Y. Yang, Y. Zhou, Z. L. Wang, *Adv. Mater.* **2012**, *24*, 6094.
- [42] J. M. Wu, C. Xu, Y. Zhang, Z. L. Wang, *ACS Nano* **2012**, *6*, 4335.
- [43] C. Chang, V. H. Tran, J. Wang, Y.-K. Fuh, L. Lin, *Nano Lett.* **2010**, *10*, 726.
- [44] D. Mandal, S. Yoon, K. J. Kim, *Macromol. Rapid Commun.* **2011**, *32*, 831.
- [45] C. Sun, J. Shi, D. J. Bayerl, X. Wang, *Energy & Environmental Science* **2011**, *4*, 4508.
- [46] J. Fang, X. Wang, T. Lin, *J. Mater. Chem.* **2011**, *21*, 11088.
- [47] C. K. Jeong, K.-I. Park, J. Ryu, G.-T. Hwang, K. J. Lee, *Adv. Funct. Mater.* **2014**, *24*, 2620.
- [48] F.-R. Fan, L. Lin, G. Zhu, W. Wu, R. Zhang, Z. L. Wang, *Nano Lett.* **2012**, *12*, 3109.
- [49] F.-R. Fan, Z.-Q. Tian, Z. Lin Wang, *Nano Energy* **2012**, *1*, 328.
- [50] L. Gu, N. Cui, L. Cheng, Q. Xu, S. Bai, M. Yuan, W. Wu, J. Liu, Y. Zhao, F. Ma, Y. Qin, Z. L. Wang, *Nano Lett.* **2013**, *13*, 91.

[51] R. Dersch, T. Liu, A. K. Schaper, A. Greiner, J. H. Wendorff, *J. Polym. Sci., Part A: Polym. Chem.* **2003**, *41*, 545.

[52] D. Yang, L. Zhang, H. Liu, Y. Dong, Y. Yu, M. Tian, *J. Appl. Polym. Sci.* **2012**, *125*, 2196.

# Chapter 6

## Conclusion

### 6.1 Overall conclusion

Flexible energy harvester has been regarded as a promising alternative energy generator for mobile application. In this study, we focused on light and mechanical energy for source of energy harvesting because light energy and mechanical energy, such as solar and human motion, were easy to extract from environment condition. Thus, we prepared the highly efficient flexible dye-sensitized solar cells and piezoelectroc nanogenerator, as a light energy and mechanical energy harvester, respectively. In addition, we demonstrated electrospray and electrospinning process to make 0-D and 1-D nanostructured materials and fabricated energy harvester using these processes.

First, we fabricated flexible dye sensitized solar cells using 0-D hierarchically structured  $\text{TiO}_2$  (HS- $\text{TiO}_2$ ) aggregates via electrospray process. (chapter 2) The HS- $\text{TiO}_2$  film formed by this method yielded a large surface area and a highly porous structure. The conversion efficiency of the as-sprayed HS- $\text{TiO}_2$  particles on the plastic ITO-PEN substrate was

poor due to poor interparticle connectivity among the as-sprayed HS-TiO<sub>2</sub> spheres. Two post-treatments were tested in an effort to enhance the interparticle connectivity. First, we mechanically compressed the films to form physically well-connected HS-TiO<sub>2</sub> structures. The conversion efficiency improved by a factor of 2 using this method. By optimizing the thickness of the photoelectrode and the compression conditions, the conversion efficiency of the flexible DSSCs reached a value of 5% for the as-pressed HS-TiO<sub>2</sub> photoelectrodes. An additional TTB low-temperature chemical treatment was applied, yielding highly efficient flexible DSSCs. The resulting TTB-treated HS-TiO<sub>2</sub> photoelectrode displayed rapid electron transport, resulting in a maximum conversion efficiency of 5.57% under 1 sun illumination (100 mW cm<sup>-2</sup>). Long-term stability of device is also important issue for real application. Thus, we compared the long-term stability of high-temperature sintered TiO<sub>2</sub> and low-temperature fabricated TiO<sub>2</sub> electrode. (chapter 3) The high-temperature sintered TiO<sub>2</sub> (H-TiO<sub>2</sub>) devices exhibited good stability after 1000 h (75.7% of its initial efficiency); however, the TiO<sub>2</sub> device fabricated at room temperatures (R-TiO<sub>2</sub>) exhibited poor long-term stability after 1000 h (34.8% of its initial efficiency) due to the desorption of adsorbed N719 dye molecules from the R-TiO<sub>2</sub> surface. The binding modes of N719 molecules on the H-TiO<sub>2</sub> and

R-TiO<sub>2</sub> photoelectrodes were analyzed by ATR-FTIR. The presence of excess surface OH groups on R-TiO<sub>2</sub> surface led to a large amount of weakly adsorbed N719 molecules on the TiO<sub>2</sub> surfaces. Dye desorption from the R-TiO<sub>2</sub> surfaces was prevented by modifying the N719 anchoring process through the addition of SA co-adsorbents to the dye solution (RS-TiO<sub>2</sub>). Although the total amounts of N719 molecules adsorbed onto the RS-TiO<sub>2</sub> surface were slightly reduced due to the competitive anchoring process between the SA and N719 dye molecules, the slow adsorption of N719 molecules increased the amounts of strongly anchored N719 on the RS-TiO<sub>2</sub> surface. The RS-TiO<sub>2</sub> device yielded a stable performance after 1000 h (70.1% of its initial efficiency). This result provides a new approach to developing long-term stable DSSCs fabricated under low-temperature/ambient conditions. In addition, we proposed co-sensitization approach for highly efficient flexible TiO<sub>2</sub> electrodes. The complementary spectral response of JH-1 and SQ2 dyes was obtained because of different absorption properties (400 nm ~ 550 nm for JH-1 and 550 nm ~ 700 nm for SQ2) of the individual sensitizers. The absorption spectra of TiO<sub>2</sub> sensitized films exhibited extended absorption range and changed by the molar ratio of dye in mixed solution. The absorption kinetics of co-sensitizer was investigated using UV-visible absorption spectra. We found that the dye

concentration of co-sensitized TiO<sub>2</sub> film is higher than that of individual dye-sensitized TiO<sub>2</sub> film. This increased dye loading of co-sensitized TiO<sub>2</sub> photoelectrode lead to enhanced photovoltaic performance. It was also found that a co-sensitization of TiO<sub>2</sub> with high molar extinction sensitizers is more effective for flexible TiO<sub>2</sub> electrode because of short diffusion length of low-temperature fabricated TiO<sub>2</sub> layer. After optimizing the molar ratio of individual sensitizer and thickness of TiO<sub>2</sub> layer, the highest conversion efficiency of 6.31% was achieved for the flexible DSSCs with the molar ratio of 6 to 4 for JH-1 to SQ2 sensitizer.

Second, we fabricated a flexible piezoelectric nanogenerator for mechanical energy harvester. The flexible nanogenerator was sandwiched using highly oriented PZT nanofibers in a PDMS matrix. The oriented PZT nanofibers were electrospun onto multi-pair parallel metal wires. The performance parameters of the nanogenerator were investigated under bending motions. The output voltage increased with the PZT thickness, whereas the output current increased as the PZT thickness and area increased. We obtained a 1.1 V output voltage and a 1.4  $\mu$ A output current at a PZT thickness of 80  $\mu$ m and an area of 8 cm<sup>2</sup>. The piezoelectric output performance was found to depend on the degree to which the fibers were uniformly oriented as well as the bending direction. The piezoelectric output

of a device in which the bending direction and fiber orientations were parallel increased rapidly at large strains, and a mechanism was proposed to describe this behavior. We demonstrated that the output voltage and current depended on the strain rate, but the total amount of generated charge was independent of the strain rate.

## **6.2 Further works**

We believe that the electrospray and electrospinning may be readily applicable for other flexible energy harvester or fabrication process for nanostructured materials. Also, the performance analysis in this study will provide a fertile base for highly efficient flexible energy harvester. However, further challenges still remained and summarize as follows.

1. The long-term stability of JH-1 sensitizer was reported, but that of SQ2 sensitizer is questionable. Additional passivation treatment for improving chemical bonding will be needed.
2. In spite of additional treatment, including mechanical compression and TTB chemical sintering treatment, the diffusion coefficient of HS-TiO<sub>2</sub> for flexible DSSCs was not sufficient for high efficiency.

3. We found that the binding mode of N719 sensitizer affect the bond strength and chemical stability. Likewise, the electron injection from dye to  $\text{TiO}_2$  may be influenced by N719 binding mode. We are currently systematically analyzing the effects of the binding mode on the electron injection properties using transient absorption measurement.
4. We prepared PZT textile comprising highly oriented PZT nanofiber. Because of environmental problem of lead in PZT, PZT is not suitable materials for wearble nanogenerator. Pb-free piezoelectric materials should be developed.

# 초 록

지난 몇 년 동안 화석연료로 촉발된 에너지 위기와 환경문제로 인해, 신재생 에너지의 개발은 상당한 주목을 받아왔다. 그 중 대부분의 연구는 수력, 풍력, 원자력과 같은 대규모 발전을 위한 연구에만 집중되었다. 최근 전자제품의 소비전력이 낮아짐이 따라, 대규모 발전을 위한 대체 에너지 자원 외에 태양광, 열 또는 기계적 에너지와 같이 우리 주변의 환경에서 쉽게 수확할 수 있는 에너지원으로부터 에너지를 수확하여 작은 규모의 모바일 전원으로 이용하려는 연구가 활발하게 연구되고 있다.

본 연구에서는 나노구조재료를 이용한 고효율 에너지 하베스터를 제작하였다. 많은 에너지원들 가운데, 빛과 기계적 에너지원에 집중하여 태양전지와 압전소자를 제작하였다. 이런 에너지원은 우리 주변에서 항상 존재하고 있고 쉽게 활용할 수 있다. 또한 이렇게 제작한 소자의 특성을 분석하였다.

첫째로, 0-D의 2차구조형 이산화티탄 응집체를 (HS-TiO<sub>2</sub>) 이용하여 유연성 염료감응형 태양전지를 제작하였다. 상온(섭씨 150도 이하)에서 유연성 염료감응형 태양전지 전극을 만들기 위해 상용 TiO<sub>2</sub> 입자가 분산된 용액을 유연성 ITO-PEN 기관 위에 전기분사하였다. 기계적 압착 또

는 TTB (Titanium n-tetrabutoxide)를 이용한 화학적 후처리 방법을 통해 유연성 ITO-PEN 기판을 이용한 소자의 효율을 향상시켰다. 기계적 압착은 HS-TiO<sub>2</sub> 전극의 표면적과 공극률을 낮추지만 입자간의 연결도와 HS-TiO<sub>2</sub> 입자와 ITO-PEN 기판의 접합력을 향상시켜 전류밀도를 향상시킨다는 것을 확인하였다. 기계적 압착 후 전극의 전자확산계수는 증가하였으나 재결합시간은 변하지 않았다. 추가적으로 효율을 향상시키기 위해 TTB를 이용한 후처리 방법에 대해 실험하였다. TTB로 코팅된 막은 섭씨 100도의 물에서 hydrolysis되어 anatase 결정상을 보여주었다. 압착 후 TTB 후처리를 통해 더 빠른 전자의 확산을 유도하여 AM 1.5G, 100 mW cm<sup>-2</sup>의 광량 하에서 광전변환효율 5.57%을 얻을 수 있었다.

유연성 염료감응 태양전지의 장기 안정성 또한 실제 응용을 위해 매우 중요하다. 본 연구에서는 상온에서 제작된 TiO<sub>2</sub> 광전극(R-TiO<sub>2</sub>)을 이용해 염료의 흡착 모드와 효율의 상관관계에 대해 연구하였다. 상온에서 전기분사법으로 만든 R-TiO<sub>2</sub> 전극은 표면에 많은 수산기(OH)가 존재하며 R-TiO<sub>2</sub> 표면에 흡착된 염료의 탈착으로 인해 매우 낮은 장기 안정성(100 mW cm<sup>-2</sup>의 광량 및 섭씨 60도의 조건에서 초기 효율 대비 34.8% 효율)을 보여주었다. R-TiO<sub>2</sub> 표면의 많은 수산기가 염료의 빠른 흡착을 유도하여 많은 양의 N719 염료가 R-TiO<sub>2</sub> 표면에 하나의 카복

시산을 통해 약하게 결합되어있음을 확인하였다. 염료 흡착 과정에서 스테아르산(SA)을 공흡착제로 이용한 경우 (RS-TiO<sub>2</sub>) TiO<sub>2</sub> 표면으로부터의 염료의 탈착을 억제할 수 있었다. N719와 SA가 TiO<sub>2</sub> 표면의 수산기를 두고 경쟁반응을 하여 염료의 흡착 속도를 늦췄고, 최종적으로 TiO<sub>2</sub> 표면에 약한 결합력으로 흡착되는 N719 염료의 양을 줄였다. RS-TiO<sub>2</sub> 전극은 염료의 탈착에 높은 저항성을 보여 향상된 장기 안정성(100 mW cm<sup>-2</sup>의 광량 및 섭씨 60도의 조건에서 초기 효율 대비 70.1% 효율)을 보여주었다.

또한 본 연구에서는 JH-1와 SQ2라는 유기염료를 혼합하여 전극에 흡착시키는 방법을 통해 넓은 영역대의 빛을 흡수할 수 있는 광전극을 제조하였다. 두 염료의 공흡착법을 이용해 6.31%의 효율을 보이는 유연성 염료감응형 태양전지를 제작하였다. 이는 JH-1을 단독으로 이용한 경우보다 높은 변환효율이다. 이런 효율의 향상은 공흡착으로 인해 많아진 염료의 흡착양에 기인한다는 것을 확인했다. 이는 N719 염료를 이용한 소자의 광전변환효율보다 우수한 값이다.

마지막으로, 1차원의 전기방사된 PZT 압전 나노섬유를 이용하여 유연성 압전 나노제너레이터를 제작하고 특성을 분석하였다. 전도성 기관 또는 평행한 금속 와이어를 이용해 전기방사된 PZT 텍스타일의 배향성을 조절하였다. 유연성 압전 나노제너레이터는 전기방사된 PZT 텍스타일을

PDMS에 함침시키고 두 장의 ITO-PEN 기판 사이에 삽입하여 제작하였다. 벤딩 응력 하에서  $8\text{cm}^2$ ,  $80\ \mu\text{m}$  두께의 PZT를 이용한 소자의 경우  $1.1\ \text{V}$ ,  $1.4\ \mu\text{A}$ 의 전기를 발생시켰다. 압전 전압은 PZT의 두께, 압전 전류는 PZT의 두께와 면적에 비례함을 실험적으로 확인하였다. 또한 PZT의 배향성과 굽힘의 방향이 소자의 성능에 중요한 인자임을 확인하였다. 마지막으로 압전 전압 및 압전 전류는 응력에 비례하지만 생성된 총 전하량은 응력 변화율에 무관하다는 사실을 알아내었다.

**주요어:** 유연성 에너지 하베스터, 나노구조재료, 태양전지, 압전 제너레이터, 전기분사, 전기방사, PZT,  $\text{TiO}_2$ , 유기염료, 장기안정성, 염료흡착, 복합재료, 전하 수송, 저온공정, 섬유배향, PDMS

**학번:** 2009-20634

# List of Publications

## Original Papers

- (1) Daesub Hwang, Horim Lee, Sung-Yeon Jang, Seong Mu Jo, Dongho Kim, Yongsok Seo, and Dong Young Kim\*, Electropray Preparation of Hierarchically-structured Mesoporous TiO<sub>2</sub> Spheres for Use in Highly Efficient Dye-Sensitized Solar Cells, *ACS Appl. Mater. Interfaces*, **2011**, 3 (7), 2719–2725
- (2) Horim Lee, Daesub Hwang, Seong Mu Jo, Dongho Kim, Yongsok Seo, and Dong Young Kim\*, Low-temperature fabrication of TiO<sub>2</sub> electrodes for flexible dye-sensitized solar cells using an electropray process, *ACS Appl. Mater. Interfaces*, **2012**, 4 (6), 3308–3315
- (3) Daesub Hwang, Horim Lee, Yongsok Seo, Dongho Kim, Seong Mu Jo and Dong Young Kim\*, Enhanced charge collection efficiency of dye-sensitized solar cells based on size-tunable hierarchically structured TiO<sub>2</sub> beads, *J. Mater. Chem. A*, **2013**, 1, 1359-1367
- (4) Daesub Hwang, Jun-Su Jin, Horim Lee, Hae-Jin Kim, Heejae Chung, Dong Young Kim, Sung-Yeon Jang & Dongho Kim, Hierarchically Structured Zn<sub>2</sub>SnO<sub>4</sub>Nanobeads for High-Efficiency Dye-Sensitized Solar

Cells, *Scientific Reports*, **2014**, 4, 7353

(5) Jihun Kim, Hyun-Sub Shim, Horim Lee, Min-Soo Choi, Jang-Joo Kim\*, and Yongsok Seo\*, Highly Efficient Vacuum-Processed Organic Solar Cells Containing Thieno [3,2-b] thiophene-thiazole, *J. Phys. Chem. C*, **2014**, 118 (22), 11559–11565

(6) Jihun Kim, Horim Lee, Dong Young Kim, and Yongsok Seo, Resonant Multiple Light Scattering for Enhanced Photon Harvesting in Dye-Sensitized Solar Cells, *Adv. Mater.*, **2014**, 26, 5192–5197

(7) Horim Lee, Daesub Hwang, Seong Mu Jo, Yongsok Seo, Dong Young Kim\*, Enhanced long-term stability of room-temperature fabricated DSSCs by stabilized binding of N719 dye, *Submitted*

(8) Horim Lee, Daesub Hwang, Seong Mu Jo, Yongsok Seo, Dong Young Kim\*, Anisotropic Piezoelectric Generation of Highly Oriented PZT Nanofibers for a Flexible Nanogenerator, *In preparation*

(9) Horim Lee, Jihun Kim, Dong Young Kim, Yongsok Seo\*, Tuning up Organic Dyes for Efficient Photo-current Generation in Dye-Sensitized Solar Cells, *Submitted*

(10) Horim Lee, Jihun Kim, Dong Young Kim, Yongsok Seo\*, Highly efficient photon harvesting by co-sensitization for flexible dye sensitized solar cells, *in preparation*